FRUSTRATED MAGNETISM STUDIES IN $NACANI_2F_7$, $ER_3GA_5O_{12}$ AND $ERMGGAO_4$

FRUSTRATED MAGNETISM STUDIES IN $NACANI_2F_7$, $ER_3GA_5O_{12}$ AND $ERMGGAO_4$

YIPENG CAI, B.Sc., M.Sc.

A Thesis Submitted to the School of Graduate Studies
in Partial Fulfillment of the Requirements
for the Degree Doctor of Philosophy

McMaster University

DOCTOR OF PHILOSOPHY (2019) McMaster University
(Physics) Hamilton, Ontario

TITLE: Frustrated magnetism studies in $NaCaNi_2F_7$, $Er_3Ga_5O_{12}$ and $ErMgGaO_4$

AUTHOR: Yipeng Cai, B.Sc., M.Sc.

SUPERVISORS: Professor Graeme Luke

NUMBER OF PAGES: viii, 72

Abstract

This dissertation details studies of three different frustrated magnet families: $NaCaNi_2F_7$, $Er_3Ga_5O_{12}$, and $ErMgGaO_4$, using a variety of techniques, including magnetization, specific heat, neutron scattering and muon spin rotation/relaxation (μSR).

$NaCaNi_2F_7$ belongs to the fluoride pyrochlores family. In this thesis, we study the effect of the randomness on the A site on the magnetic property of B site. This chemical disorder randomness was caused by the mixture of two different elements from Group 1 and 2 (Na and Ca). DFT calculation and computation simulations indicates a possible non-centred $F - \mu - F$ muon stopping site. Zero field (ZF) and longitudinal field (LF) μSR shows that the Ni^{2+} spins undergo spin freezing into a disordered ground state below 4K, with persistent spin dynamics to our lowest temperature 75 mK.

We obtained high quality single crystal of $Er_3Ga_5O_{12}$ by utilizing the optical floating-zone (OFZ) technique. We performed inelastic neutron scattering measurements to determine the crystalline electric field (CEF) Hamiltonian, eigenvalues and eigenvectors, indicating an Ising-like anisotropy ground state which is also consistent with our specific heat experiment with entropy approaching $Rln(2)$. All seven crystalline electric field excitations from the ground state Kramers doublet were identified. In addition, Rietveld refinement of neutron powder diffraction data reveal that $Er_3Ga_5O_{12}$ orders into the Γ_3 magnetic structure, with ordered magnetic moment $\mu_{ord} = 5.24(4)\ \mu_B$, in agreement with $\mu_{Ising} = 5.61\ \mu_B$ from our deduced CEF Hamiltonian. Our μSR measurements also reveals the presence of fluctuating local fields on the muon timescale, indicating exotic slow spin dynamics in the ground state.

The objective of the work on $ErMgGaO_4$ was to identify a new quantum spin liquid candidate. Single crystals of $ErMgGaO_4$ were obtained through (OFZ) technique as well, and the structure was refined and confirmed by powder X-ray diffraction and Laue diffraction after a repeated refinement of our synthesis process. Susceptibility measurements reveal no evidence of a magnetic transition down to 0.5 K, in agreement with specific heat measurement which exhibit no anomalies which would have been evidence of an ordering transition. ZF-μSR measurements reveal no sign of coherent long range order or spin freezing down to 25 mK, while LF-μSR measurements shows persistent spin dynamics at 25 mK. Our observations provides evidence for a quantum spin liquid ground state in this compound.

Acknowledgements

During my research there are numerous people who have provided invaluable assistance, without whom much of the work would not have been completed. First, I would like to thank my supervisor, Graeme Luke, for providing the wonderful research environment at McMaster. From the first day when I came across to Canada, his willingness in allowing me to explore scientific researches, teaching me effective scientific studies and writing and providing quick feedback on ideas helped me enjoying my PhD time.

I also want to thank my PhD colleagues from McMaster University: Alannah Hallas, James Beare, Murray Wilson, Tim Munsie, Connor Buhariwalla, Jonathan Gaudet, Dalini Maharaj, Casey Marjerrison and Darryl MacBeath. Thank you for the friendships through all these years in making my daily life colourful, especially for Murray and Connor. Thank you also to our frequent μSR collaborators from Columbia: Yasutomo Uemura, Benjamin Frandsen, Lian Liu, Sky Cheung, Zizhou Gong, and Qi Sheng. I am also very grateful for the support I received from Cheryl Johnston, Rosemary McNeice, Tina Stewart and Mara Esposto.

My research would have been much more difficult without the assistance of numerous technicians and beam-line scientists. I would first like to thank all of the staff at TRIUMF, particularly Bassam Hitti, Deepak Vyas, Gerald Morris, and Donald Arsenault. I admire your dedication to helping any users of the μSR facilities at TRIUMF. Having such knowledgeable people available to ask for help, even at midnight later hours on the weekend, is a wonderful resource, not to mention all of the work that goes on behind the scenes keeping all of the instruments running in tip-top shape. I would also like to thank to staffs at Oak Ridge National Lab, especially Adam Aczel at HB2A beam-line, thank you for giving such great help to perform successful neutron scattering experiments. I would also like to thank Paul Dube and Jim Garret at McMaster for their invaluable assistance in many aspects of my research.

I would like to thank my family. Thank you to my Mom, Dad, Sister and Rita Wang for always encouraging me to pursuing my dreams and believing in me. Especially for Rita, I am always looking forward to walk through the remaining lifetime.

Finally, after having spent so much time out of my country, I am beyond grateful to all the people I met in Canada. Thank you all.

Contents

1 Introduction **1**

1.1 Frustrated magnetism . . . 1

1.2 Crystal electric field . . . 3

1.3 Spin glass state in the Pyrochlore lattice . . . 7

1.4 Magnetic ordered state in garnet lattice . . . 8

1.5 Quantum Spin liquid state in triangular lattice . . . 8

2 Experimental Methods **10**

2.1 Floating Zone Optical Image Furnaces . . . 10

2.2 SQUID Magnetometry . . . 15

2.3 Muon Spin Rotation and Relaxation . . . 17

2.3.1 Muon basics . . . 17

2.3.2 μSR models in frustrated magnetic materials . . . 19

2.3.3 $F\mu F$ bond . . . 25

2.4 Neutron Scattering . . . 28

3 $NaCaNi_2F_7$ **31**

3.1 Summary of $NaCaNi_2F_7$ . . . 31

4 $Er_3Ga_5O_{12}$ **41**

4.1 Summary of $Er_3Ga_5O_{12}$ . . . 41

5 $ErMgGaO_4$ **53**

5.1 Summary of $ErMgGaO_4$ . . . 53

6 Conclusions and Future Directions **61**

7 Appendix **63**

List of Figures

1.1 Ising spins with Antiferromagnetic nearest neighbour interactions on the a) triangular lattice and b) square lattice. The triangular lattice shows frustration, as the spin denoted with ? cannot satisfy the requirement of the antiferromagnetic interactions simultaneously with its neighbours. 2

1.2 Typical frustrated magnetic lattices with 2D and 3D triangular motifs. In 2D, a) triangular lattice, b) and kagomé lattice. In 3D, c) pyrochlore lattice, and d) garnet lattice 2

1.3 Detailed local D_2 symmetry of the Er^{3+} (green) ions surrounded by eight closest O^{2-} ions (red). 6

2.1 a) Picture of NEC furnace in McMaster University with loaded feed and seed rods of $ErMgGaO_4$. Quartz tube is not installed for clarity of the view, b) schematic diagram of optical floating zone apparatus (fig.b from Ref. [23]) 11

2.2 Crystal of $Er_3Ga_5O_{12}$ grown in the NEC optical floating zone furnace with about 2 cm single crystal. Bottom shows the pictures of the reflection light (left) and transmission light (right) 13

2.3 Laue pattern of $Er_3Ga_5O_{12}$ grown in the NEC optical floating zone furnace. Alignment was identified in the [001], [110] and [111] orientations. 14

2.4 Schematic of a typical setup of SQUID. The black dot shows the sample moving through the orange loops. The orange loops present the pick-up loop and generates a typical current signal as shown on the right. The current signal later was capture by the SQUID loop and output a voltage signal in a similar shape of signal. Typical movement of the sample is vertically through the pick-up coil around 6 cm 16

2.5 Diagram of the muon spin precessing in the presence of a field $\mathbf{B}$ 19

2.6 The effect of increasing longitudinal fields on the Gaussian Kubo-Toyabe function. Dashed line shows the 1/3 position 22

2.7 Muon spin polarization functions for a Gaussian distribution of static local fields ($\nu = 0$) for various fluctuation rates from static to the fast fluctuation regime ($\nu/\Delta = 40$). Dashed line shows the 1/3 position. 24

2.8 LF dependency of Gaussian Kubo-Toyabe polarization at selected fluctuation rate ($\nu/\Delta = 1, 10$). 25

2.9 Muon polarization function of $G_{F\mu F}$ signal at selected bond distances $2r = 2.205\ \mathring{A} + \Delta r$. 27

Preface

This is a sandwich thesis containing published article and preprint work in sections. A summary to the subject area is provided at each section.

Publication I: "*μSR study of spin freezing and persistent spin dynamics in $NaCaNi_2F_7$*", Y. Cai, M.N. Wilson, A.M. Hallas, L. Liu, B. A. Frandsen, S. R. Dunsiger, J. W. Krizan, R. J. Cava, Y. J. Uemura, O. Rubel, and G. M. Luke. J. Phys.: Condens. Matter **30** 385802.
Reproduced from Ref. [1] with permission, copyrighted by the American Physical Society.

Preprint I: "*Crystal fields and magnetic structure of the Ising antiferromagnet $Er_3Ga_5O_{12}$*", Y. Cai, M.N. Wilson, J. Beare, C. Lygouras, G. Thomas, D.R. Yahne, K. Ross, K.M. Taddei, G. Sala, H.A. Dabkowska, A. A. Aczel, and G. M. Luke. *arXiv*:1905.03687 (2019).

Preprint II: "*μSR study of triangular Ising antiferromagnet $ErMgGaO_4$*", Y. Cai, C. Lygouras, G. Thomas, M. N. Wilson, J. Beare, D.R. Yahne, K. Ross, Z. Gong, Y. J. Uemura, H.A. Dabkowska, and G.M. Luke. *arXiv*:1905.12798 (2019).

1

Introduction

1.1 Frustrated magnetism

Since ancient times, researchers have discovered various types of magnetism in materials and have studied the theory of magnetism as well as searching for new magnetic materials for applications [2]. One important current area of magnetism research is the study of frustrated magnets. The concept of general magnetic frustration was first introduced by Toulouse [3] and Anderson [4]. Frustrated magnets are materials in which pairwise magnetic interactions cannot be simultaneously satisfied due to their geometrical arrangement. An example of such a situation is that of antiferromagnetic interactions between spins on a triangular lattice. The Heisenberg Hamiltonian for an antiferromagnetic interaction between any two spins can be written as a scalar product of two spin operators, $\hat{H}_{ex} = -2J\hat{S}_i \cdot \hat{S}_j$ $(J < 0)$, where $J < 0$ represents the case of antiparallel (antiferromagnetic) correlation. Fig 1.1a depicts the situation for three nearest neighbour spins, in the case where two spins are antiparallel with up and down alignments, while the third spin cannot align antiparallel with both its neighbours simultaneously. This system therefore cannot achieve a state that entirely satisfies the microscopic constraints, giving rise to a macroscopic degeneracy of the system ground state. This can be very different for the square lattices, Fig 1.1b, which is clearly not frustrated under the same condition.

Antiferromagnetically coupled spins on lattices with triangular motifs provide one of the common basis components for frustration. Conditions for magnetic frustration are satisfied in many real materials and the effect of the frustrations is usually seen in their magnetic properties. As shown in Fig 1.2, either corner or edge-sharing triangles are key motifs present in two dimension(2D), including stacked triangular lattice and kagomé lattice, as well as in three

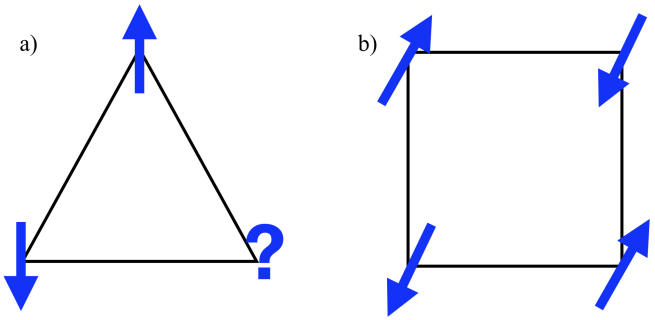

Figure 1.1: Ising spins with Antiferromagnetic nearest neighbour interactions on the a) triangular lattice and b) square lattice. The triangular lattice shows frustration, as the spin denoted with ? cannot satisfy the requirement of the antiferromagnetic interactions simultaneously with its neighbours.

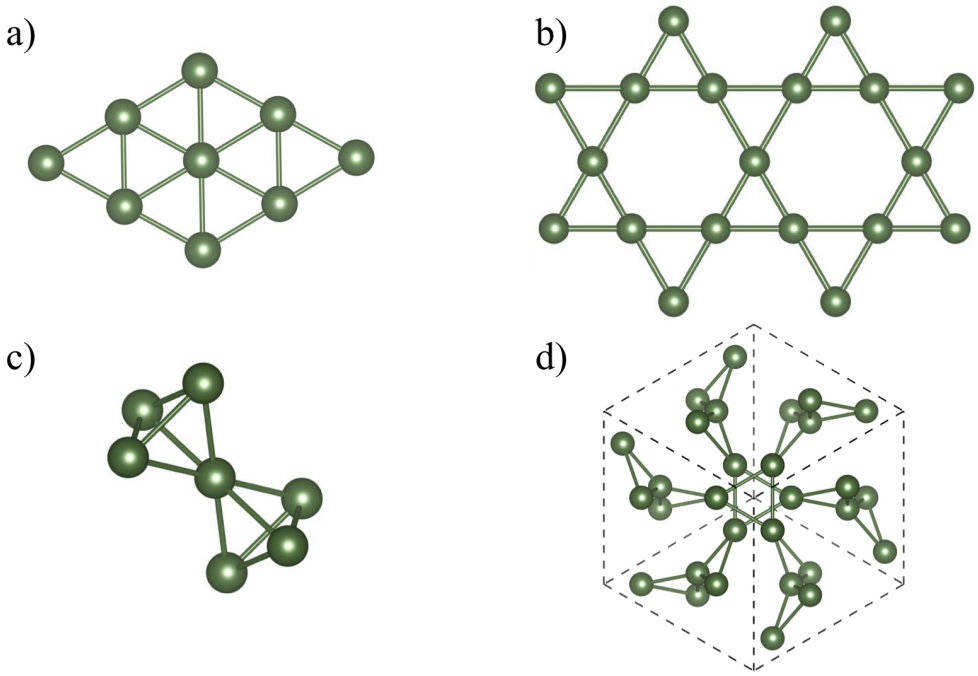

Figure 1.2: Typical frustrated magnetic lattices with 2D and 3D triangular motifs. In 2D, a) triangular lattice, b) and kagomé lattice. In 3D, c) pyrochlore lattice, and d) garnet lattice

dimensional cases such as the pyrochlore and garnet lattices which may also incorporate corner or edge-sharing tetrahedra. Depending on the circumstance, the spins could be correlated but fluctuating, or order into a magnetically ordered state, resulting in potential exotic magnetic ground states including spin glasses, spin ices and spin liquids [5]. There have been numerous studies on the effect of frustration on magnetic properties and ground state selection. In order to further understand how frustration can promote the existence of new magnetic ground states, it is useful to synthesize and characterize new geometrically frustrated materials.

This thesis is composed of three studies each has focused on one of above mentioned frustrated magnetic materials systems:1) $NaCaNi_2F_7$ as the pyrochlore lattice, 2) $ErMgGaO_4$ as the stacked triangular lattice and 3) $Er_3Ga_5O_{12}$ as the garnet lattice. Each of these chapters is in the form of a paper which has either been published or submitted for publication.

1.2 Crystal electric field

The magnetism of both the rare earth garnets and pyrochlores originates from the unpaired $4f$ electrons localized on the rare earth ions. Therefore, the single ion properties of the rare earth ions are essential for understanding the resulting magnetic properties.

Following Hund's rules, the single ion properties are dominated by the Coulomb interactions between their $4f$ electrons, which could be first minimized by two steps in order of importance: 1) maximizing the total spin angular momentum S to reduce the overlap of the spatial wavefunctions in order to minimize the strongest spin-spin coupling and 2) maximizing the total orbital angular momentum L, which further reduces the overlap of wavefunctions.

The next most important is the spin-orbit coupling which is more pronounced in higher-Z elements. In light atoms, the interactions between the orbital angular momenta is much stronger than the spin-orbit coupling where this kind of coupling is called $L-S$ coupling. However, for some very heavy elements, spin orbit coupling can become comparable or even more important than the above spin-spin and orbit-orbit couplings. In these cases, a $J-J$ coupling scheme provides better agreement with experiment.

In rare earths ions, which we are dealing with in this work, the way that takes the spin-orbit coupling as the lower level interactions provides better agreement with experiment here; which obeys Hund's third rule: if under half filled, J should be minimized $J = |L-S|$, if over half filled, J should be maximized $J = |L+S|$. In such a manner, for the example of the Er^{3+} ion, this leads to a state with $L = 6, S = 3/2, J = 15/2$. Finally, this $(2J+1) = 16$ fold degeneracy is lifted by the electric field of the nearby ions. CEF on the rare earth ions are due to the Coulomb potential

from the neighbouring oxygen ions in the crystalline environment. The order of magnitude of spin-orbit coupling (∼1 eV) is usually much bigger than that of CEF (∼100 meV): together they lift the ground state degeneracy and controls the magnetism of the rare earth ions. After all these lifting effects, one can calculate the magnetic moment for each of these cations as

$$\mu = g_J \sqrt{J(J+1)} \mu_B, \tag{1.1}$$

where g_J is the Landé factor given by

$$g_J = \frac{3}{2} + \frac{S(S+1) - L(L+1)}{2J(J+1)}, \tag{1.2}$$

These predictions of magnetic moments are usually in good agreement with experimentally determined values for $4f$ ions. The models we have considered has assumed that spin-orbit coupling is weak enough and viewed as a perturbation to the electrostatic interactions, namely the $L-S$ coupling. For atoms with high atomic number (Z), this will not work since the spin orbit interaction energy is proportional to Z^4. Therefore, such strong effects should not be considered as a perturbation, where a $J-J$ coupling shall be introduced to describe such scenario.

Kramers theorem states that for any system with half integer spin, every energy level must be at least doubly degenerate to preserve time reversal symmetry [6]. With Er^{3+} as our example, the $(2J+1) = 16$ fold degeneracy can be split at most into eight doublets under the effect of CEF, which is the case in both the local environment in titanate pyrochlore and gallium garnet. For ions with integer spin, this theorem does not apply.

The crystalline electric field effects are typically small such that one can treat CEF splitting as a perturbation on an appropriate free ion wave function and energy levels. In this way, the energy levels and wave functions in the crystal field can then be found from a standard perturbation theory. It is useful to theoretically calculate the CEF and the crystalline potential energy on the basis of a simple point charge ionic model given by

$$\hat{H}_{CEF} = \sum_{ij} q_i V(r_j, \theta_j, \phi_j) = \sum_{ij} \frac{q_i q_j}{|(\mathbf{R}_j - \mathbf{r}_i)|}, \tag{1.3}$$

where q_j is the effective point charge at the jth neighboring ion with the j neighbors typically taken to be the closest ions to the magnetic site, at a distance R_j from the origin with the magnetic ion has charge q_i at position of (r_i, θ_i, ϕ_i). The energy contribution can be evaluated in cartesian coordinates, but it's far more convenient to express the crystalline electric potential

in tesseral harmonics which could be easily transform to matrix elements through spherical harmonics that capture the local symmetry.

$$V(r,\theta,\phi) = \sum_{n=0}^{\infty}\sum_{\alpha} r^n \gamma_{n\alpha} Z_{n\alpha}(\theta,\phi) \tag{1.4}$$

where

$$\gamma_{n\alpha} = \sum_{j} \frac{4\pi q}{2n+1} \frac{Z_{n\alpha}(\theta_j,\phi_j)}{R_j^{(n+1)}} \tag{1.5}$$

and the $Z_{n\alpha}(\theta_j,\phi_j)$ are the tesseral harmonics. A detailed summary of the transform process are described in Ref. [7]. The CEF Hamiltonian act on ith ion turns to be

$$\hat{H}_{CEF} = q_i \sum_j q_j \sum_n \frac{r^n}{R_j^{(n+1)}} \frac{4\pi}{(2n+1)} \sum_{m=-n}^{n} (-1)^m Y_n^{-m}(\theta_j,\phi_j) Y_n^m(\theta,\phi), \tag{1.6}$$

where Y_n^m are spherical harmonics. By using the Stevens operator equivalents method [7], these spherical harmonics could be transformed to Stevens operators, in a final form of summation of combination of Stevens operators, $\hat{O}_n^i$, and CEF coefficients, B_n^i as follows:

$$H_{CEF} = \sum_{n=2,4,6} \sum_{m=-n}^{n} B_n^m \hat{O}_n^m, \tag{1.7}$$

where

$$B_n^m = A_n^m \langle r^n \rangle \theta_n \tag{1.8}$$

with

$$A_n^m = q_j \sum_j \frac{4\pi}{(2n+1)} (-1)^m \frac{Y_n^m(\theta_j,\phi_j)}{R_j^{(n+1)}} \tag{1.9}$$

and $\langle r^n \rangle$ is the expectation values of the electron radial coordinate for the $4f$ wave function, and θ_n is the multiplicative factor ($\theta_{2,4,6} = \alpha, \beta, \gamma$)

Taking the $Er_3Ga_5O_{12}$ as an example with its local environment as shown in Fig. 1.3, the Er^{3+} site has a D_2 point group symmetry, containing four symmetry elements $\{E, C_2(x), C_2(y), C_2(z)\}$ which are identity operation E and three two fold rotation operation along x, y, z. Its corresponding crystal electric field Hamiltonian is given by

$$\hat{\mathcal{H}}_{D_2}^{CEF} = \sum_{i=0,2} B_2^i \hat{O}_2^i + \sum_{i=0,2,4} B_4^i \hat{O}_4^i + \sum_{i=0,2,4,6} B_6^i \hat{O}_6^i, \tag{1.10}$$

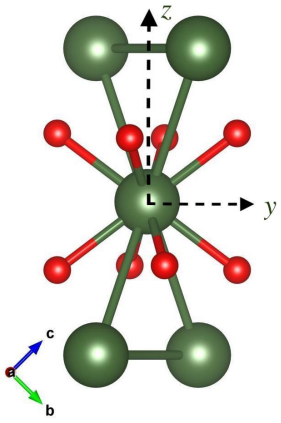

Figure 1.3: Detailed local D_2 symmetry of the Er^{3+} (green) ions surrounded by eight closest O^{2-} ions (red).

where the Stevens operators, $\hat{O}_n^i$, are combinations of total angular momentum operators and the coefficients B_n^i could be experimentally determined through spectroscopic measurement or can be theoretically calculated using point charge calculations from Eq. 1.8.

Once those CEF parameters are determined, the ground state wave function, $\phi_0^{\pm}$, can also be calculated along with the corresponding CEF levels. The anisotropic g-tensor for the doublet ground state can also be computed as

$$g_{\parallel} = 2g_J|\langle\phi_0^{\pm}|J_z|\phi_0^{\pm}\rangle|; \;\; g_{\perp} = g_J|\langle\phi_0^{\pm}|J_{\pm}|\phi_0^{\mp}\rangle| \tag{1.11}$$

where $g_{\parallel}$ is the g-tensor component along the defined z (Ising) direction and $g_{\perp}$ is the component perpendicular to the z direction. An Ising-like spin anisotropy is obtained in cases where $g_{\parallel}$ is much greater than $g_{\perp}$. Conversely, an XY-like spin anisotropy is obtained when $g_{\perp}$ is much greater than $g_{\parallel}$. If $g_{\parallel}$ is as comparable to $g_{\perp}$, a Heisenberg-like anisotropy is obtained. The effective magnetic moment can also be obtained by

$$\mu_{eff} = \frac{1}{2}\sqrt{g_x^2 + g_y^2 + g_z^2} \tag{1.12}$$

The point charge calculation on CEF coefficients and CEF analysis were coded in Matlab software based on the theorem discussed above. Those Matlab codes are provided in Appendix A.

1.3 Spin glass state in the Pyrochlore lattice

Many materials with frustrated interactions do not exhibit a phase transition to a long range ordered state. This is well-illustrated in pyrochlore lattice compounds with six nearest coordinated spins. Pyrochlores have the chemical formula $A_2B_2X_7$, and these belong to the cubic space group $Fd3m$, where both A and B metal sublattices form an interpenetrating three dimensional tetrahedral networks. The magnetic lattice of pyrochlores can be pictured as a network of corner-sharing tetrahedra. These different ions on both A and B sites allow broad tuning of the physical interactions. For example, in titanium B-site pyrochlores, placing dysprosium on the A-site gives a classical spin ice state, whereas gadolinium gives a unique partially ordered state [8–10]. From a microscopic point of view in a spin ice pyrochlore structure with a ferromagnetic interaction, a minimum energy state for each tetrahedron can be obtained as to be close to parallel as possible, also called two-in two-out state which arises from the effect of the CEF. Similarly, as to an antiferromagnetic interactions, an all-in all-out structure is obtained. There are six two-in two-out states for one tetrahedron and any configuration in which all tetrahedra are in such a state is a ground state. Such ground state can be macroscopically spread that no long range ordered state can emerge, resulting in a state with an enormous degeneracy and residual entropy [11].

The competing energy scales in these systems (such as spin exchange, and dipolar interactions), spin anisotropy as well as sensitivity to dilute disorder have emerged as extremely important in selecting the ground states of these materials. These effects can work to select a ground state or set of states which will may or may nor be long-range ordered states. The most commonly observed non-ordered state is the spin glass state where the moments are frozen, but in random configurations. This is the subject of the first chapter of the thesis work on $NaCaNi_2F_7$, in which local (A-site)disorder selects a spin glass ground state. The spin glass state is a configuration of spins frozen into a certain pattern from a fluctuating state at a freezing or glass temperature, T_f. Since the frozen state is selected spontaneously, the exact ground state is determined by the experimental conditions, which naturally leads to hysteresis in magnetic properties. There are many signatures of the spin glass state, where most commonly used is the magnetic susceptibility: a divergence below T_f in the DC magnetic susceptibility in field cooled and zero field cooled susceptibility, and a frequency dependence of T_f as well in the AC susceptibility. Other important features are a sharp decrease in spin fluctuation rate or increase in the spin relaxation time below the freezing temperature T_f. Such decrease of spin relaxation time and its spin dynamics properties are well-suited for and measured by μSR in our study of $NaCaNi_2F_7$.

1.4 Magnetic ordered state in garnet lattice

Despite these exotic ground states without long range order, it was frequently seen that a actual phase transition occurs in some frustrated magnets. One example is the rare earth gallium garnet, which are three dimensional lattices with triangular motifs as shown in Fig. 1.2, consisting of 3D array of corner sharing triangles. In the rare earth gallium garnet, the Gd does not order while other REs ions, Nd, Sm, Dy, Ho and Er, do order. It is also interesting to compare the garnets with the well studied titanate pyrochlores, where both are thought to be three dimensional frustrated magnets. In contrast to that of garnets, the Gd titanate pyrochlore orders while other REs, Tb, Dy and Ho, do not. Such difference could be due to the different local environment and the different J values of the magnetic ions, which resulting in a different single ion properties in these two structures. Therefore, the study of the crystal electric field properties and magnetic properties is also essential in understanding this three dimensional frustrated magnet family, which is another focus of this thesis.

1.5 Quantum Spin liquid state in triangular lattice

A ground state frequently studied in geometrically frustrated magnets is the spin liquid in which an interacting system remains dynamic and disordered down to temperature well below the Curie-Weiss temperature. It differs from spin glasses in that there is no spin freezing and no well-defined distinct T_f for such materials. In quantum spin liquids (QSLs), the spins can remain truly dynamic down to the lowest temperature as the liquid state is driven by quantum spin fluctuations. There have been many studies and some progresses on QSLs [12–14] and it has been found that geometric frustration and low dimensionality are expected to be supportive in forming such a quantum spin liquid state. The QSL was originally proposed in 1973 by Anderson with an idea of spin paired singlets (namely resonating valence bond state RVB) superposed on a 2D triangular lattices with antiferromagnetic exchange interactions, in which the spins simultaneously point in different directions and are highly long-range entangled [15]. There is no exact solution for QSL state defined by the RVB model and the theoretical possibility of such a non-magnetic ground state from well defined local moments has been debated. The experimental search for QSLs has been challenging because of the lack of unique positive signatures, however it is well-motivated as they are holding promising application potentials such as quantum computation [16] besides its rich and exotic physics. In such a background, searching for new QSLs is the motivation for the work on $ErMgGaO_4$ described in this thesis.

When searching for QSL candidates, it is difficult to definitively prove the existence of a QSL since there is no easily accessible experimental feature that can serve to identify a QSL, though the existence of a QSL state can be disproven through the observation of magnetic order or spin freezing. But there are several positive indications for QSL candidates such as: a large frustration parameter, persistent spin dynamics at low temperatures, dynamic correlations and excitations, as well as the existence of fractionalized excitations. $ErMgGaO_4$, one focus in this thesis, is an iso-structural material to $YbMgGaO_4$ which is a quasi-two dimensional triangular-lattice structure recently shown to be a promising QSL candidate [17–20]. $YbMgGaO_4$ has a Curie-Weiss temperature of $\sim$ -4K and shows no sign of long-range order or spin freezing down to 30 mK [17–19, 21]. The magnetic specific heat in zero magnetic field shows a broad hump at 2.4 K instead of a sharp λ-type peak which would have been expected for a well-defined second order phase transition. The magnetic excitation spectra appears as a broad continuum in inelastic neutron scattering measurements, which has been taken as an evidence for a QSL state [19, 21]. In $YbMgGaO_4$, anisotropic exchange interactions between rare earth ions are thought to play a crucial role in stabilizing a spin liquid ground state [17–22]. Such exchange interactions as well as anisotropy property arises from crystal electric field strongly depends on rare earth ions. Work on $ErMgGaO_4$ could help understanding the these materials and expanding the family of QSL candidates, where we would expect a different anisotropic exchange interactions in Er compared to Yb.

2

Experimental Methods

In modern materials science, it is normally the case that a variety of techniques are required to understand any particular problem. This chapter introduces the main experimental methods which were used within this thesis, including the Floating Zone Optical Image Furnace, Laue diffraction, powder X-ray diffraction, SQUID magnetometry, muon spin rotation, and neutron scattering. All of these experimental techniques are well established such that this section will mainly focus on the most relevant aspects for this thesis.

2.1 Floating Zone Optical Image Furnaces

The crystals of $Er_3Ga_5O_{12}$ and $ErMgGaO_4$ discussed in this thesis were grown using the Floating Zone Optical Image Furnaces at McMaster University. The optical floating zone crystal growth method has been extensive developed since nearly half a century ago. Commercially available image furnaces from Nippon Electric Co. (NEC) and Crystal systems from Japan have been utilized extensively world-wide in institutes and universities for growing large high quality single crystals (particularly for transition metal oxides). At McMaster University, we employe two two-mirror NEC furnaces and one four-mirror Crystal Systems furnace.

In an optical image furnace, ellipsoidal mirrors are used to focus the light from halogen or xenon lamps onto a vertically held rod to produce a molten zone which is held in place by surface tension. Mention that the benefit of this method is that the liquid only touches material of the same composition, which can give very pure samples. Then the lamps are moved up, or the rods are moved down so that material is transferred through the molten zone from the feed rod (top) to the seed rod (bottom), hopefully in the form of a single crystal.

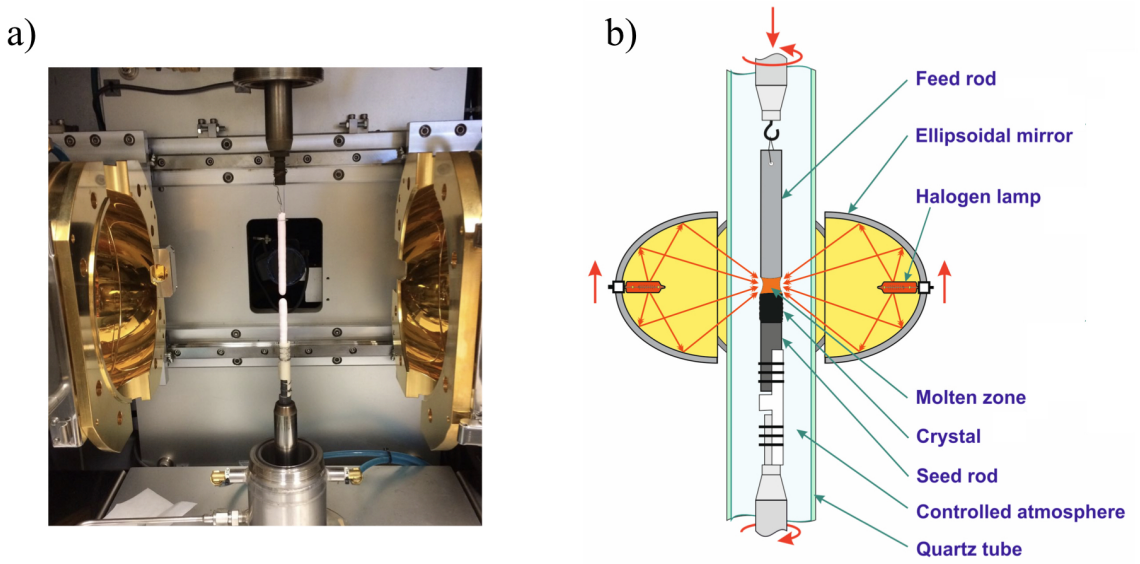

Figure 2.1: a) Picture of NEC furnace in McMaster University with loaded feed and seed rods of $ErMgGaO_4$. Quartz tube is not installed for clarity of the view, b) schematic diagram of optical floating zone apparatus (fig.b from Ref. [23])

Fig 2.1 shows a photograph of one of our two-lamp (NEC) furnaces at McMaster University as well as a schematic diagram of a two mirror optical floating zone system. The furnace consists of the rotating water cooled motor hooked with the feed rod on the very top and a counter-rotating motor mounted with seed rod at the bottom. These two motors control the feeding speed and the growing speed, two essential controlling parameters during the growth. Polycrystalline starting material of desired composition (the feed and seed rods), is placed close to the common foci in the elliptical mirror cavity, while halogen lamps were placed at the other foci, ensuring the focusing of the light and heating is as homogeneous as possible in the hot zone. The common foci is the hottest spot and could be heated up to as high as 2200 degrees, such that a melting zone is formed if the material's melting point is below that temperature. The rods are enclosed in a transparent quartz tube chamber, which could be filled with specialized atmospheres or vacuum, where argon and oxygen were mostly used during the growth as needed. The inner pressure can also be set up to 10 atmospheres pressure: high pressure is sometimes employed to discourage evaporation of material. Since the molten zone never contacts anything else other than gases and itself, there is no incorporation of impurities from a crucible (held in place by surface tension). It is important to maintain a stable molten zone in this type of crystal growth,

for this reason, materials with low surface tension (where the zone can easily spill) or a high vapour pressure (where constituents can evaporate during growth, possibly obscuring the quartz tube) are not generally suitable.

There are multiple advantages to utilizing an optical floating zone furnace: firstly, no crucible is used during the growth and that both congruently and incongruently (though a flux is often needed in this case) melting materials can be grown. This allows for the growth of large sized of crystals up to 9 cm long with diameter of about 5 mm, which are amenable for experiments like neutron scattering and μSR. The growth can also be conducted at over-pressure and in a controlled gas atmosphere. Another advantage is the small segregation coefficients of most impurities in the molten zone, in other words, the solubility of impurity atoms in the melt is often larger than that in the solid. Hence, the impurities contained in the feed rod would remain in the melt and carry to the end of the growth. If all the conditions are properly done, the newly crystallized material can be obtained as a single crystal.

A typical crystal growth process has two major steps as follows (given the example of $Er_3Ga_5O_{12}$ growth) :

Preliminary ceramics preparation: first, powder raw materials of Er_2O_3 and Ga_2O_3 are placed in a pre-set 80 degree dryer for at least 48 hrs, mainly in order to get rid of water. The typical batch of 25 grams of powders is then weighed according to the desired chemical reaction and is prepared by ball-mixing and later by manual grinding using a mortar. The mixed powders are then formed into a rod, typically 8 mm in diameter and 10 cm long, by a hydrostatic pressure of 60 MPa for 15 minutes, producing a dense rod. The pressed rods are later sintered at an optimized temperature (1100 degrees C) and appropriate atmosphere (in air) for 48 hrs for a complete reaction. The weight of the rods was recorded both before and after the sintering in order to check whether there was any weight loss. This is important to know whether or not evaporation is an issue for a floating zone growth. Small part of the rods were later ground up for powder X-ray as well, to check that the desired phase was formed. Uniformly dense ceramics are ideal in preparation as gas bubbles incorporated into the feed rod can seriously influence the zone and even destroy the growth process.

Optical floating zone growth: After hanging up a feed rod on the top and mounting the seed rod on the bottom as shown in Fig 2.1a, centering of both rods are important to obtain and maintain a stable molten zone. The quartz tube was later installed and filled with a continuous argon gas flow at a pressure of 2 atms and maintains the correct oxidation state of the constituents. This over-pressure also eliminates the risk of contamination due to any small leaks in the sealed

tube. After the installation and turning on of the cooling system, the power was gradually increased until the light focused on the sample just started to melt the seed rod. Before the initial melting starts, counter rotation of feed and seed was started to ensure uniform heating and efficient mixing in the molten zone. The feed rod was then lowered and touched to the seed rod, forming a well-defined melting zone. Stability of the growth process as well as the quality of the obtained crystal depend strongly on the stability of the melting zone. Once a molten zone was achieved, we increased the rotation rate of both rods, which enhances convection in the liquid, resulting in a more stable molten zone. The growth speed was usually set between $1 - 10$ mm/h, with 3 mm/h for the garnet growth. Once the feed rod is exhausted, or the crystal is sufficiently long, the growth was ended by slowly decreasing the temperature of the molten zone and the feeding speed. This will narrow the molten zone and the crystal, eventually, finished with the separation between the feed and seed rod. After the separation, the feed rod was pulled away and its rotation was stopped, while the seed rod growing speed was set to zero and its rotation speed reduced to a slow rate. Such a slow cooling procedure helps to reduce the risk of cracks or breaking of the crystal due to the quenching effect. The power was also set to zero at a slow rate.

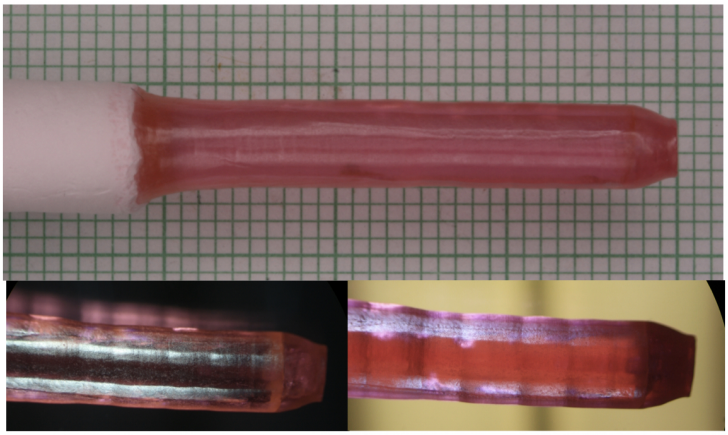

Figure 2.2: Crystal of $Er_3Ga_5O_{12}$ grown in the NEC optical floating zone furnace with about 2 cm single crystal. Bottom shows the pictures of the reflection light (left) and transmission light (right)

Depending on the material, a varying growing speed can affect the size, formation of secondary

phases, cracks, and the crystal grain orientation. Multiple attempts at growth for a new system are usually required to optimize the growing conditions. The goal is to grow a large single crystal, however that is usually not the case in the first 1-2 cm solidified crystals as it usually contains multiple grains. These grains typically grow preferentially as crystallization advances and are forced out by grains more commensurate with direction of growth. Eventually, by adjusting the growing conditions, one grain can dominate the crystal. Indications showing the material has become a single crystal include a change from a circle to an ellipse cross section and the formation of shiny facet on the material. However, one must simply wait until the end of the growth and later use other techniques to see whether they are single crystal [24].

An example of a crystal of $Er_3Ga_5O_{12}$ grown in the NEC optical floating zone furnace is shown in Fig 2.2. The transparent pink coloured crystal shows the correct oxidation state and is a supportive sign of a single crystal. The crystal was later aligned with the Laue X-ray diffraction showing the single crystal nature, as shown in Fig 2.3.

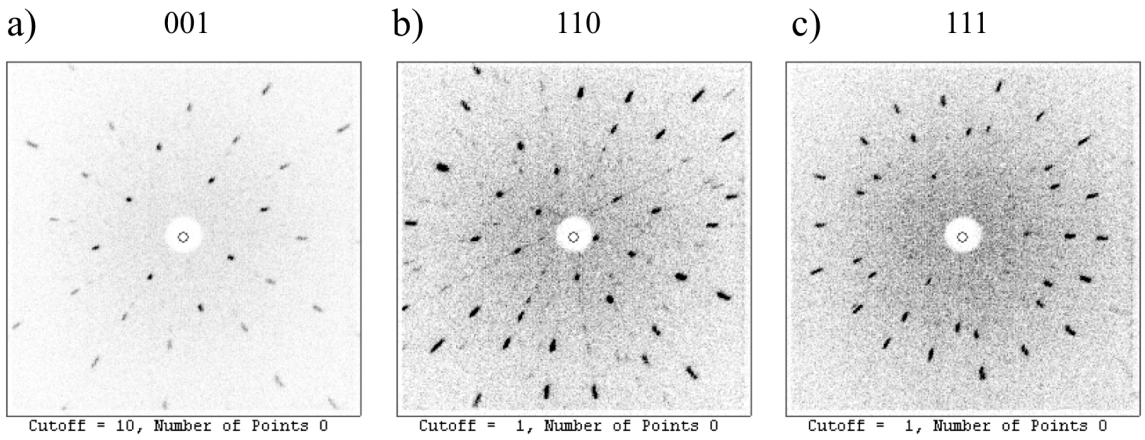

Figure 2.3: Laue pattern of $Er_3Ga_5O_{12}$ grown in the NEC optical floating zone furnace. Alignment was identified in the [001], [110] and [111] orientations.

2.2 SQUID Magnetometry

The Superconducting QUantum Interference Device (SQUID) magnetometer is the most sensitive commercially used method for bulk magnetization properties characterization. The basis of a SQUID is the Josephson junction, as first predicted by B. Josephson [25] and with a signal pick-up coil based on the induction law. When a magnetic sample moves through the loop, it changes the magnetic flux in the pick-up coil, and a corresponding current is generated in the loop due to the induction effect. This flux through the loop coupled with the current was later sensed by the SQUID and a voltage response is obtained by affecting the coupling with the junction loop driven with a bias circuit. This converted output voltage signal is directly proportional to the magnetic moment of the sample.

As shown in Fig 2.4, key component for a SQUID consists of a broken superconducting loop, i.e. Josephson junction, and the pick-up coil. The pick-up coil shown is a second order gradiometer, made by creating a single clockwise turn, followed with two counter-clockwise turns and another clock-wise turn. This second derivative coil design improves the noise and almost entirely eliminates any background field or gradient variations.

There are two types of SQUID devices: the DC-SQUID and the RF-SQUID. These devices vary in the number of Josephson junctions and the method operation. The underlying difference of DC and RF SQUID is its utilizing theory of DC and AC Josephson effect. Fig. 2.4 shows the DC-SQUID with two Josephson junctions in parallel in a superconducting loop. The SQUID loop captures the changing magnetic flux, Φ, due to this changing inductance current from the moving sample. This current around the SQUID superconducting loop will oscillate in the period of the flux quantum, Φ_0 due to the DC Josephson effect. In actual devices, there is always a bias current applied on the SQUID loop, the detected voltage across the device will be given by [26]

$$V = \frac{R}{2}\sqrt{I_b^2 - [2I_c\cos(\frac{\pi\Phi}{\Phi_0})]^2}, \tag{2.1}$$

where V is the voltage across the device, I_b is the applied bias current, R is the resistance of the junctions. Hence, this allows magnetic flux to be converted to the output voltage as measured.

For a RF-SQUID with only one Josephson junction, the superconducting loop is coupled to a circuit driven by a RF current source, experiencing the flux from the current Φ_{RF}. Again, when the loop captures the magnetic flux signal Φ_{sample} from the sample, the external flux in the loop becomes $\Phi_{ex} = \Phi_{sample} + \Phi_{RF}$. Since there is always a certain inductance L from the circuit that we must take into account in this case, the total flux in the loop is

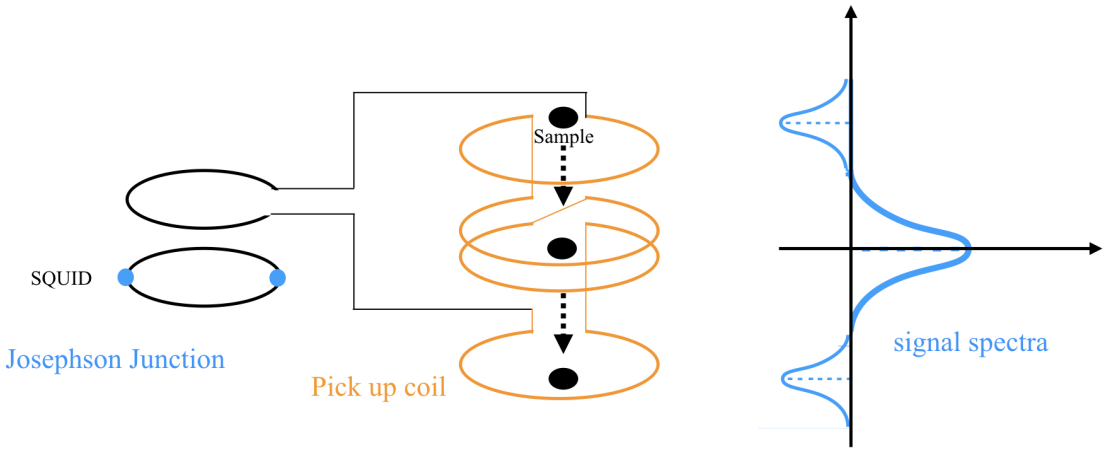

Figure 2.4: Schematic of a typical setup of SQUID. The black dot shows the sample moving through the orange loops. The orange loops present the pick-up loop and generates a typical current signal as shown on the right. The current signal later was capture by the SQUID loop and output a voltage signal in a similar shape of signal. Typical movement of the sample is vertically through the pick-up coil around 6 cm

$\Phi_{total} = \Phi_{ex} - LI$, where I is the current flowing in the loop. Considering the Josephson effect that the phase difference must be equal to 2πn, the current in the loop then becomes $I = I_0 sin(2\pi n - \frac{\phi}{\Phi_0})$. Hence, after rearrangement, a self-consistent relation for total flux through the loop is $\Phi_{total} = \Phi_{ex} - LI_0 sin(\frac{2\pi\Phi_{total}}{\Phi_0})$. As the AC current oscillates over time, the difference between the Φ_{total} and Φ_{RF} (known) could then be calculated, and again allowing magnetic flux to be converted to output voltage as measured.

All the magnetization measurements in this thesis were done utilizing the Quantum Design MPMS XL-3 magnetometer, a RF-SQUID on both Helium-4 and and Helium-3 inserts. The output of measurements is the magnetic moment, M, recorded in *emu*, and were later used for the analysis of susceptibilities.

2.3 Muon Spin Rotation and Relaxation

Muon Spin Rotation and Relaxation (μSR) is one of several modern techniques for microscopic magnetic measurements. It is the most powerful tool in detecting weak internal field in presence of an actual zero field. It is generally used to probe the magnitude of the internal field and its field distribution, dynamics properties and the volume fraction of different phases if present. Below I give a brief description of the technique. Further details can be found in Ref. [27–29].

2.3.1 Muon basics

Muons are unstable fundamental particles with a characteristic lifetime of $\tau_\mu = 2.197\ \mu s$. They behave like an electrons in many ways with spin $\frac{1}{2}$, and a mass approximately 207 times that of the electron. Once coupled with their local environment via their spin, muons experience Larmor precession at a frequency of $\nu = \gamma_\mu |\mathbf{B}_{loc}|$, where $\gamma_\mu = 135.54$ MHz / T is the muon gyromagnetic ratio and $|\mathbf{B}_{loc}|$ is the local field at the muon site. Muons can carry a positive or negative charge and spontaneously decay into an electron (for the μ^-) or position (for the μ^+) and a neutrino/anti-neutrino pair. Only positive muons were used in our μSR experiments. Once the muon decays it emits a decay position preferentially along the direction of its spin at the time of decay due to the parity violation of the weak interaction [28]. The angular distribution of the emitted positrons follows $W(\theta, a(E)) = 1 + a(E)\cos(\theta)$, where W is the probability of the positron emitted at an angle of θ which is the angle between the positron trajectory and the muon spin direction, and $a(E)$ is the energy dependent intrinsic asymmetry parameter. By measuring this anisotropic distribution of the decay positions from a statistical ensemble of implanted muons, one can measure the statistical average direction of the spin polarization with an expected average direction asymmetry of 1/3. The spatial distribution and dynamical fluctuations experienced by the muons can be seen in the time evolution of the muon spin polarization. That allows us to study the magnetism in the magnetic materials with μSR.

There are many ways to produce muons in high energy processes. One requirement for using those muons is a lower enough energy such that they can actually stop in the samples instead of going through them. The most used way to produce low energy muons is from pion decay. At the TRUIMF laboratory in Vancouver, where all the experiments discussed in this thesis were conducted, the pions (π) are produced by the collision of high energy protons with a light nuclei such as carbon or beryllium to maximize their production. These pions, at rest in the surface layer of the target, quickly decay, $\tau_\pi = 26\ ns$, into a muon and a muon neutrino. They are emitted during the decay in opposite directions because the pion was at rest. In order to

conserve momentum, they have equal and opposite momentum. Due to the parity violation of the pion decay, neutrinos are all left-handed, and so to conserve angular momentum, the muons are also created left-handed, giving essentially 100% spin polarization. Both π^- and π^+ were produced during the process, but π^- are always captured inside the target, therefore no μ^- are created, leaving only μ^+ beam with momentum of 29.8 MeV/c and corresponding kinetic energy 4.119 MeV. These surface muons have a mean stopping density of about 120 mg/cm^2, so they stop in the bulk of fairly thin samples ranges of 0.1 to 1 mm, depending on the density of the stopping material. After the production, the muon beam is first collected by a quadrupole doublet located very close to the target, following with slits as for selecting beam momentum acceptance. There are also dual separators/spin-rotators setup before the beam hit the sample. These rotators which consist of crossed electric and magnetic fields can be set to low values to separate positrons and to high values to also rotate the muon spin to be perpendicular to the beam direction. Hence, depends on the direction of the incident muon beam, they can classified as: Non Spin Rotated (NSR) mode where the muon spins are roughly antiparallel to the the incoming beam direction, and Spin Rotated (SR) mode, where the spins are perpendicular to the incoming beam direction. Once can switch between these mode to study properties both in and out of the plane in the three dimensional materials.

In μSR experiments, spin polarized muons are implanted into the sample one at a time, throwing away events that arise when two or more muons are simultaneously stopped in the sample. The muons thermalize rapidly in the material, coming to rest at a stopping site while maintaining their spin polarization. These thermalized muons find a minimum electrostatic potential site where they come to rest and then their spins precess in the local magnetic field until they decay. In materials containing fluorine or oxygen, muons generally thermalize close to these highly electronegative ions. To accurately determine these muons stopping sites, it is necessary to conduct a density functional theory calculations to determine the position with minimum electrostatic potential. Sometimes, there are multiple minimum energy (meta) stable sites in a crystal, this situation usually leads to multiple muon stopping site, such that multiple signals in the experiment data need to be accounted for.

Once the muon decays, the emitted positrons are observed by the detectors. There are usually two opposing pairs of detectors, one pair detectors on the front (F) and back (B) to the sample and the other pair is either up (U) and down (D) or left (L) and right (R) to the sample. By observing the sequential decay of millions of muons that stop and decay in the sample one after another, histograms of the number of counts as a function of time, for example along the beam

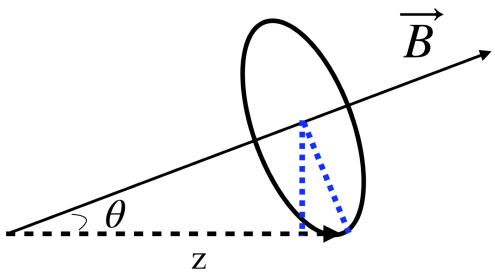

Figure 2.5: Diagram of the muon spin precessing in the presence of a field **B**

direction (B and F counters) can be constructed as

$$N_{B,F}(t) \propto e^{-t/\tau_\mu}(1 \pm A_{B,F}P_z(t)). \tag{2.2}$$

where A is the total muon asymmetry, P(t) is the time dependent muon polarization, and the e^{-t/τ_μ} presents the muons' lifetime, and the $\pm$ refers to the direction of the two counters relative to the initial muon spin polarization.

To avoid the muons' lifetime time dependency in the data analysis, we compute the asymmetry between the front and back counters as

$$A(t) = AP_z(t) \propto \frac{N_B(t) - \alpha N_F(t)}{N_B(t) + \alpha\beta N_F(t)}. \tag{2.3}$$

Where, A is the total asymmetry of the counters, and α, β are correction factors, where $\alpha = \frac{N_B^0}{N_F^0}$ accounts for the difference in solid angle of each detectors relative to the sample and the detection efficiency of these two counters, β is related to the construction and efficiency differences of the detectors, and is usually assumed to be 1.

2.3.2 μSR models in frustrated magnetic materials

Static probabilistic models

Suppose muons are probing a constant magnetic field with an angle θ relative to the initial muons spin directions as shown in Fig. 2.5. Then the z component of the muon polarization can be written by Eq. 2.4

$$P_z(t) = \cos^2(\theta) + \sin^2(\theta)\cos(\gamma_\mu|\overrightarrow{\mathbf{B}}|t). \tag{2.4}$$

In the case of $\theta = \pi/2$ where the local field is perpendicular to the muon spin, the polarization function becomes $P_z(t) = \cos(\gamma_\mu |\overrightarrow{\mathbf{B}}| t)$, giving a pure oscillation. In real materials with multiple muon stopping sites where muons could be experiencing different local fields, it could be easily constructed as sum of all these polarization functions together as $P_z(t)_{total} = \sum_i A_i \cos(\gamma_\mu |\overrightarrow{\mathbf{B}_i}| t)$, where A_i is the weight of different muon stopping sites.

This scenario has always been used in a weak transverse field (wTF-μSR) measurements, where instead of the local internal field, an external weak magnetic field is applied perpendicular to the muon spin, usually in magnitude around 30 G in the paramagnetic state. Two main reasons for a wTF measurements are 1) to perform calibration of the value of total asymmetry as well as α as mentioned in Eq. 2.3, and 2) to determine the magnetic volume fraction of the sample. For the second reason, a weak transverse field is applied in a magnetically ordered state. If the sample is partially magnetically ordered, then the muons are experiencing two different types of local field, an applied weak transverse field, and fields from magnetic moments of the sample. Assuming that the field strength from the magnetic moments is much larger than the weak transverse field, which is usually the case, the polarization function will have two components which gives the asymmetry ratio that tells the magnetic volume fraction of the sample. High transverse fields are often used in measuring the magnetic field distribution of the vortex lattice in a type-II superconductor or for measuring the Knight shift (proportional to the spin susceptibility) in materials.

Following Eq. 2.4, a more general form in zero external field with a given distribution of local fields $P(\overrightarrow{B})$, the polarization function can be expressed as Eq. 2.5:

$$P_z(t) = \int \{(\frac{B_{loc}^z}{B_{loc}})^2 + \frac{B_{loc}^{x^2} + B_{loc}^{y^2}}{B_{loc}^2} \cos(2\pi\nu_\mu t)\} P(\overrightarrow{B}) d^3\mathbf{B}_{loc}. \tag{2.5}$$

where different muons will feel different fields and therefore precess at different rates. This will produce a dephasing of the spins and a decrease in the overall polarization. In the case of a randomly ordered magnetic sample following spherically symmetric Gaussian distribution where Δ is the field distribution standard deviation, as expected for a dense array of randomly oriented static moments:

$$P(\overrightarrow{B}) = (\frac{1}{\sqrt{2\pi}\Delta})^3 e^{(B_x^2 + B_y^2 + B_z^2)/(2\Delta^2)} \tag{2.6}$$

the polarization function $P_z(t)$ can be analytically calculated as

$$P_z(t) = \frac{1}{3} + \frac{2}{3}(1 - \Delta^2 t^2) e^{-\Delta^2 t^2/2} \tag{2.7}$$

The polarization function is known as the Gaussian Kubo-Toyabe function. Similarly, if the internal magnetic fields follow a Lorentzian probability distribution, which is actually good approximation of field distribution in real magnetically diluted materials with frozen magnetic moments. Then Eq. 2.7 turns to the following relaxation function known as the Lorentzian Kubo-Toyabe function in ZF:

$$P_z(t) = \frac{1}{3} + \frac{2}{3}(1 - at)e^{-at/2} \tag{2.8}$$

where a reflects the width of the exponential field distribution.

In both cases, the constant 1/3 in the polarization functions means that on average there always 1/3 of the spins do not depolarize and seen as persisting polarization. One could either think it is due to the symmetry that the measurements lose its degree of freedom in the z direction, or just simply from the mathematically derivation of the integral of $\cos^2(\theta)$. This is important as it tells that the polarization function obtained from a powder sample shall be that 1/3 of the polarization will be parallel to the local field in a powder sample.

A LF$-\mu$SR experiment involves the application of an external magnetic field parallel to the initial direction of the muon spin in the ZF set-up. In the ZF$-\mu$SR, the muon spin polarization is completely out of thermal equilibrium so that a dynamical relaxation towards the equilibrium unpolarized state typically shows up as an additional decay in the spectra. A LF$-\mu$SR set-up can probe this dynamical relaxation rate as a function of applied LF, which adds an additional muon Zeeman energy term to the polarization. These dynamic properties will be addressed in the following part. Considering the same example of Gaussian distribution in ZF$-\mu$SR, the Gaussian distribution is then shifted from the origin in the direction of the muon spin since the muon are experiencing the combination of the Gaussian distribution local moments and the LF. The expression for the polarization function is found to be [30]:

$$P_z(t) = 1 - (\frac{2\Delta^2}{\omega^2})[1 - e^{-\frac{1}{2}\Delta^2 t^2}\cos(\omega t)] + (\frac{2\Delta^4}{\omega^3})\int_0^t e^{-\frac{1}{2}\Delta^2\tau^2}\sin(\omega\tau)d\tau, \tag{2.9}$$

where ω is the external LF expressed in frequency units. One can imagine that when the external LF is increased bigger enough such that the incoming muons are dominated by the LF instead of the local magnetic fields, the polarization will turn to a constant and almost equal to one. This process of muons becoming insensible to the local magnetic field due to the LF is called "decoupling". An example of the decoupling in the Gaussian distribution is illustrated in Fig. 2.6. It can be seen the Gaussian Kubo-Toyabe polarization is gradually decoupled as the

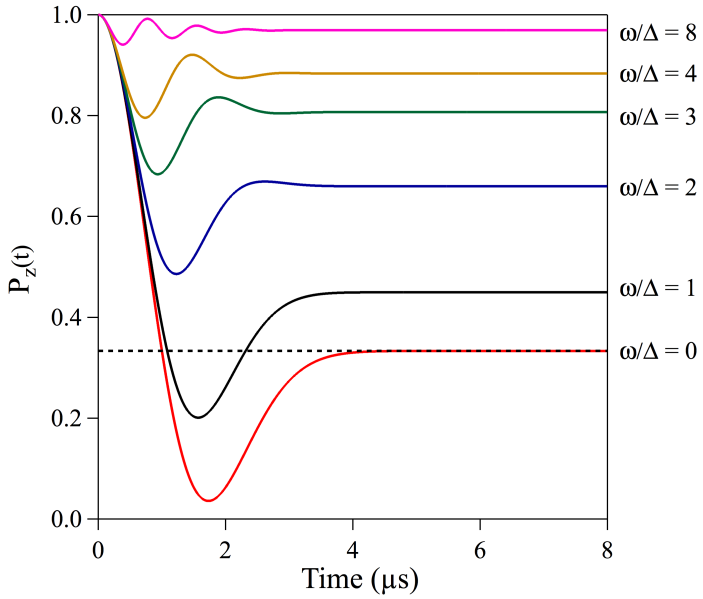

Figure 2.6: The effect of increasing longitudinal fields on the Gaussian Kubo-Toyabe function. Dashed line shows the 1/3 position

plateau tail increases with increasing LF. Similar results could be also obtained with a Lorentzian Kubo-Toyabe distribution.

This decoupling feature are always used to understand the dynamic or static nature of the local field. If the observed relaxation of the muon polarization comes from static magnetism, applying a LF will add this external field component to the internal field. Hence, muons are probing a net field that is closer to the direction of the muon spin, resulting in a reduced relaxing asymmetry. However, if the depolarization comes from dynamics, the signal will not be decoupled by such an applied field, as there is no well-defined weak internal field as discussed more in the next section.

Dynamic probabilistic models

In the previous Section.2.3.2, we supposed the muon to be at rest in the compound and the field distribution at the muon site to be static both in the Gaussian and Lorentzian Kubo-Toyabe relaxation functions. However, in practice, this condition does not hold in most real materials, especially in frustrated magnets as mentioned in Chapter.1.1. We also showed that the LF-μSR could help to detect such dynamic feature at the last of Section.2.3.2. One should always keep in mind that the actual field distribution is dynamic to some extent.

In characterizing the time-dependent disorder in ZF/LF-μSR, the most used model for understanding these dynamics is the strong collision model [30,31]. In this model, a Markovian process is introduced as, once the muon thermalized, it will see a given field for a period of time t, then this field will change abruptly to another value drawn from the same distribution for period of time t_1, and it keeps changing again and again according to a probability distribution given as follows:

$$\frac{\langle B(t)B(0)\rangle}{\langle B(0)^2\rangle} = e^{-\nu t} \tag{2.10}$$

In other words, muons are experiencing a sudden change in the local field rather than a gradual change, hence, the correlation between the local fields is completely ignored through the sudden change. Assuming dynamics arises from relatively slow magnetic fluctuations (relative to the muon precession in the static field), under the strong collision assumption, during each given time t', the muon's polarization follows the static Kubo-Toyabe function, and the relaxation function $P_z(t)$ at time t is a superposition of contribution from both muons that have and have not experienced such process during time t and could be given as [30]:

$$P_z^{(n)}(t) = \sum_{n=0}^{\infty} p_z^{(n)}(t) \tag{2.11}$$

where $p_z^{(0)}(t)$ means no such change happened during time t, with $p_z^{(0)}(t) = Eq.\ 2.7 \times e^{(-\nu t)}$, and

$$p_z^{(n)}(t) = \nu^n \int_{t^{(n)}}^{t} ... \int_0^{t''} dt(n)...dt^{'} p_z(t - t^{(n)})...p_z(t^{'})e^{-\nu t} \tag{2.12}$$

where n shows the number of changes, and t^i indicates the time of the i-th change during time t. This model does not have a general analytic solution, but it can be numerically obtained and simplified by Laplace transform as shown in Ref. [30] with

$$P_z(t) = \int_0^{\infty} \frac{f_z(s+\nu)}{1-\nu f_z(s+\nu)} e^{-st} ds, \tag{2.13}$$

where

$$f_z(s) = \int_0^{\infty} [\frac{1}{3} + \frac{2}{3}(1-\Delta^2 t^2)e^{-\frac{1}{2}\Delta^2 t^2}]e^{-st} dt \tag{2.14}$$

If the observed magnetic fluctuations are sufficiently fast enough ($\nu \gg \Delta$), the muons will average over the distribution of the fields from those changes time to time and experience a narrower field distribution, which is the motional narrowing limit. And the polarization rate will

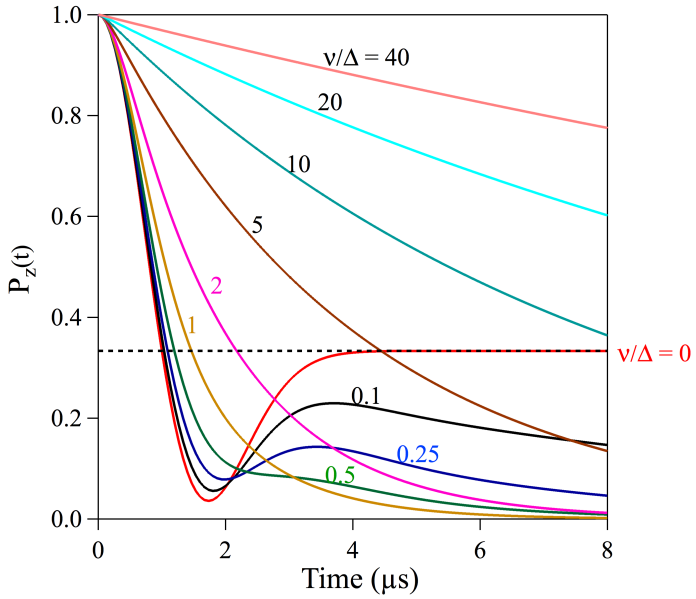

Figure 2.7: Muon spin polarization functions for a Gaussian distribution of static local fields ($\nu = 0$) for various fluctuation rates from static to the fast fluctuation regime ($\nu/\Delta = 40$). Dashed line shows the 1/3 position.

consequently decrease due to the dephasing and take the form of exponential as

$$P_z(t) = e^{-\lambda t} \tag{2.15}$$

where $\lambda = 2\Delta^2/\nu$ characterizes an effective muon spin lattice relaxation rate, known as $1/T_1$.

In Fig. 2.7, examples of polarization function ($P_z(t)$) are presented for several values of dynamic fluctuation rates ν, in the case of the Gaussian local field distribution. When the fluctuation rate ν is zero, it collapses to the static Kubo-Toyabe function shown previously in Eq. 2.7. For an increasing small fluctuation rate ($0 < \nu/\Delta < 1$), the polarization's 1/3 tail starts relaxing and becomes faster and faster while the early times 2/3 signal remains almost unchanged. If the fluctuation rate is faster ($\nu/\Delta > 1$), motional narrowing effect becomes significant, the static minimum gets inhibited and the 2/3 signal relaxation slows down, and starts the decoupling. In the case of faster fluctuations approaching the motional narrowing limit, the polarization function becomes the Eq. 2.15 as shown for $\nu/\Delta = 20, 40$.

In the presence of LF, for the motional narrowing limit, the relaxation rate from Eq. 2.15 becomes

$$\lambda = \frac{2\Delta^2\nu}{\omega^2 + \nu^2} \tag{2.16}$$

which is also known as the Redfield formula.

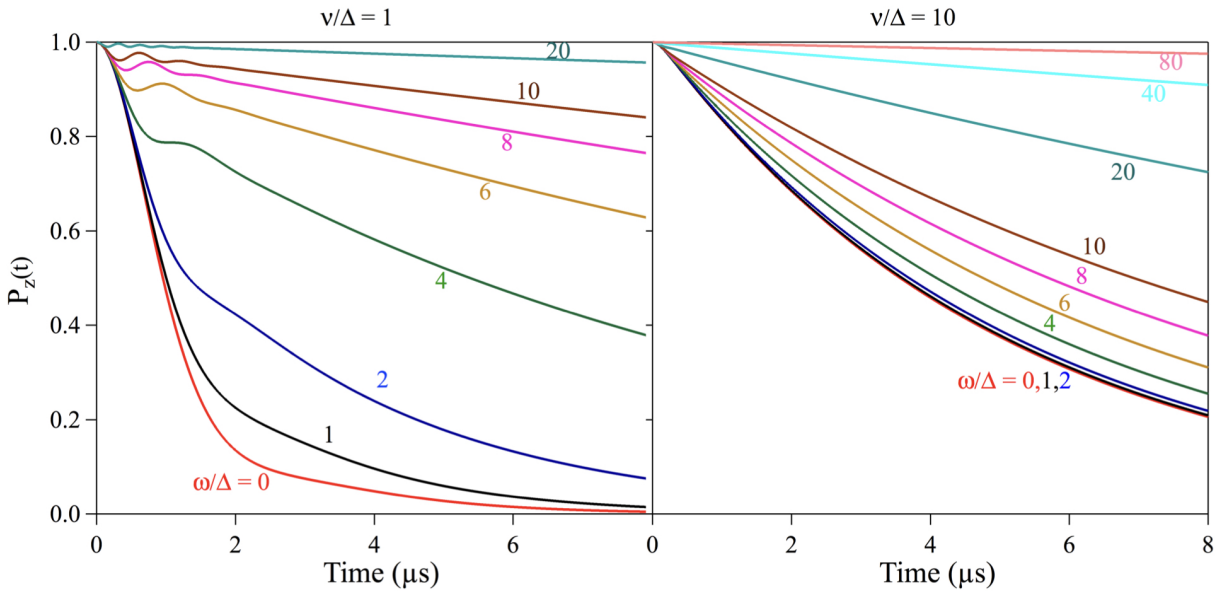

Figure 2.8: LF dependency of Gaussian Kubo-Toyabe polarization at selected fluctuation rate ($\nu/\Delta = 1, 10$).

Fig. 2.8 shows the *decoupling* effect on Gaussian Kubo-Toyabe polarization in presence of selected fluctuation rates and LFs. A nearly fully decoupled spectra requires at least a value of 20 ($\omega/\Delta = 20$) for the external LF even when the fluctuation is relatively slow ($\nu/\Delta = 1$). If the signal comes from purely static magnetic moments, as shown in Fig. 2.6, a value of 8 (field given in frequency units) already fully decoupled the spectra. If the fluctuations is bigger, let say $\nu/\Delta = 10$, it takes at least a field of 80 for a comparable decoupling. Hence, LF measurements are very useful to determine if a magnetic environment is static or dynamic.

2.3.3 $F\mu F$ bond

A special case need to be addressed is that when materials contain fluorine, an μSR signals obtained from such materials always shows a characteristic shape of the formation of an $F-\mu-F$ bond [32–36]. As the positive muons thermalized into such materials, they are attracted to the negatively charged F^- ions. Note the fluorine has a magnetic moment of 2.6 μ_n with angular momentum of $\frac{1}{2}$, at high temperature, well above any magnetic transition, where the electronic fluctuations are exchange narrowed and too rapid to contribute to the muon spin relaxation

signal, the signal in such compounds typically shows oscillations attributed to the $F-\mu-F$ magnetic dipole interaction. This is caused by the dipole-dipole interactions between the muon and the surrounding fluorine nuclei (usually two fluorines). It was first introduced by modelling the simplest configuration of muons lying at the mid-point between two fluorine ions in a cubic environment, and the ZF-μSR relaxation function $G_{F\mu F}(t)$ can be obtained by averaging over all different orientations

$$P(t) = A_{total}(fe^{-(\lambda_1 t)^{\beta}}G_{F\mu F}(t) + (1-f)e^{-\lambda_2 t}) \tag{2.17}$$

with

$$\begin{aligned} G_{F\mu F} = 1/6(3 + \cos(\sqrt{3}\omega_d t) + \\ (1 - 1/\sqrt{3})\cos[((3-\sqrt{3})/2)\omega_d t] + \\ (1 + 1/\sqrt{3})\cos[((3+\sqrt{3})/2)\omega_d t]). \end{aligned} \tag{2.18}$$

where ω_d is the muon-fluorine dipole frequency, β is a phenomenological stretching parameter, λ_1 is the relaxation rate of the F-μ-F signal and λ_2 represents the relaxation of the fraction of spins which do not participate in the $F\mu F$ formation (i.e background).

The parameter ω_d in Eq. 2.18 is the strength of the magnetic dipole-dipole interaction between the muon and the fluorine, and is given by

$$\omega_d = \frac{\mu_0 \hbar \gamma_\mu \gamma_F}{2\pi r^3}, \tag{2.19}$$

where r is the bond distance between the muon and fluorine, γ_μ and γ_F are the gyromagnetic ratios of muons and fluorine. The Coulomb interaction between muon and fluorine is usually strong enough that the bond distance r is always close to approximately 1.16 Å. Hence, there could be significant local distortion to the fluorine positions due to the presence of muons. This distortion effect is frequently seen, and is caused by the strength of the electrostatic attraction between the muons and fluorine ions, which is also seen in $NaCaNi_2F_7$.

Eq. 2.18 is commonly used for systems which present the $F\mu F$ formation. One should caution that a precise form of Eq. 2.18 only holds if the muon lies in the middle of two fluorines in the system with a cubic symmetry. In addition, the μSR signal of $F\mu F$ also depends on the initial muon spin direction and the formed $F\mu F$ bond direction. In practice, it is possible that the muon lands in off-centred sites with a random spin direction once they thermalize and form $F\mu F$

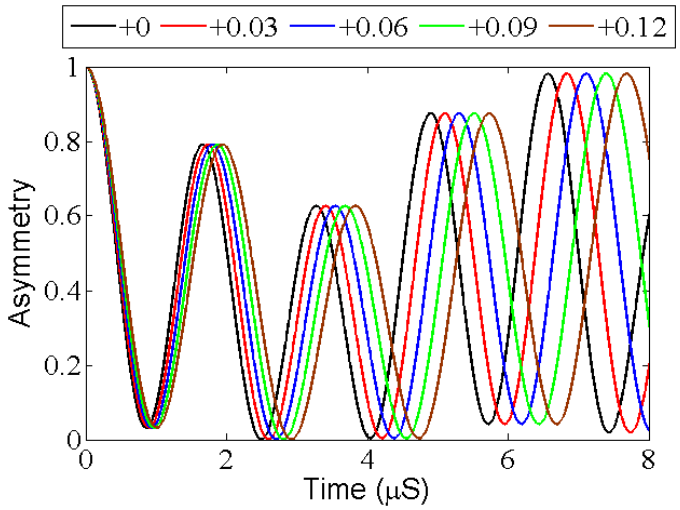

Figure 2.9: Muon polarization function of $G_{F\mu F}$ signal at selected bond distances $2r = 2.205\ \mathring{A} + \Delta r$.

bonds. To investigate details of such different configuration, a numerical simulation is needed, which was performed in the work of $NaCaNi_2F_7$.

Fig. 2.9, shows how $G_{F\mu F}$ behaves at selected $F\mu F$ bond distance, with $2r = 2.205\ \mathring{A} + \Delta r$.

2.4 Neutron Scattering

Neutron scattering is another well developed and powerful technique used in condensed matter physics. It is used to determine the crystal and magnetic structure of materials, as well as excitations on the scale of 0.1 meV to multiple eV, such as phonons, magnons and crystal field excitations. There are two neutron experiments in this thesis, the inelastic neutron scattering experiment performed utilizing SEQUOIA at the Spallation Neutron Source and the powder neutron diffraction experiment carried out on HB2A beamline at High Flux Isotope Reactor (HFIR). Both instruments are located at Oak Ridge National Laboratory (ORNL).

Neutron scattering makes use of neutrons beams and it has its own unique advantages. By contrast to other typical scattering probes like electrons, neutrons are uncharged particles and thus unaffected by Coulomb interactions. This gives neutrons comparatively high penetration (low absorption) for most elements. Neutrons do, however, possess a magnetic moment of spin 1/2. This results in interactions with nuclei of atoms and the unpaired electrons of the materials in interest for the study of magnetism. Neutron beams can be produced by spallation and fission, and can then be moderated to provide a wide range of wavelengths. The widely-used thermal neutrons have wavelengths on the order of 1 Å and an average kinetic energy on the order of 10 meV. This makes them appropriate for probing the static and dynamic properties of materials, as the atomic spacings and elementary excitations are typically of comparable length and energy scales respectively.

In a typical neutron scattering experiment, an incident neutron beam interacts with a sample of interest, resulting in a scattered beam. The energy and wavevector of the incident neutron beam are selected by choppers (at SEQUOIA) or a monochromator (at HB-2A). The scattering happens with a momentum and energy transfer which are both conserved during the event and follows as $\mathbf{k_f} = \mathbf{k_i} + \mathbf{Q}$ and $\hbar\omega = E_i - E_f = \frac{\hbar^2 \mathbf{k_i}^2}{2m_n} - \frac{\hbar^2 \mathbf{k_f}^2}{2m_n}$.

The partial differential scattering cross section is given as [37]:

$$\frac{d^2\sigma}{d\Omega dE} = (\frac{m_n}{2\pi\hbar^2})^2 \frac{k_f}{k_i} |\langle \mathbf{k_f}\sigma_f | \hat{V} | \mathbf{k_i}\sigma_i \rangle|^2 \delta(\hbar\omega + E_i - E_f) \tag{2.20}$$

where $\mathbf{V}$ is the potential that the neutron experiences, σ_i and σ_f represent the initial and final states of the sample, E_i and $\mathbf{k_i}$ are the incident energy and wavevector of the neutron, E_f and $\mathbf{k_f}$ are the final energy and wavevector of the neutron, m_n is the neutron mass, and the Dirac δ-function ensures conservation of the energy during the scattering events.

As the atoms in crystalline materials are periodically arranged in the real space with position

r, their corresponding reciprocal lattice vectors $\mathbf{Q}$ are defined in the reciprocal space. In the case of elastic neutron scattering, neutron powder diffraction measurements are performed to determine the crystal and magnetic structure, in which neutrons are diffracted by parallel planes of atoms in the crystal with interplanar spacing $d = 2\pi/\mathbf{Q}$. Bragg's law establishes the required conditions for constructive interference of the scattered beam (i.e. Bragg peaks) and is given by [38]: n $\lambda = 2\text{dsin}\,\theta$, where n is an integer representing the order of the reflection and 2θ is the scattering angle in the experiment. The structure factor determines the relative intensity of the Bragg peaks and is given by:

$$S(\mathbf{Q}) \propto \sum_{i}^{N} b_i e^{-i\mathbf{Q}\cdot\mathbf{r}_i} \tag{2.21}$$

where b_i is the scattering length (which accounts for the strength of the neutron-nuclear scattering for the atom at site r_i) and the sum is over the nuclei in the unit cell. If the sample of interest is in powder form, the structure factor must be averaged over all possible crystal orientations. Note that the powder-averaged structure factor is only non-zero for coherent nuclear scattering if Q is equal to a reciprocal lattice vector $\mathbf{G}_{hkl}$.

Apart from the interaction with nuclei, neutrons also interact with magnetic moments on atoms with unpaired electrons. Below the magnetic ordering temperature in a material, this scattering leads to additional intensity in a neutron diffraction pattern (i.e. magnetic Bragg peaks). The relative intensities of these peaks is determined by the magnetic structure factor:

$$M(\mathbf{Q}) \propto \sum_{i}^{N} \mathbf{M}_{\perp} e^{-i\mathbf{Q}\cdot\mathbf{r}_i} \tag{2.22}$$

where $\mathbf{M}_{\perp}$ represents the component of the magnetic moment that is perpendicular to the scattering vector $\mathbf{Q}$. Hence, neutron scattering is an excellent tool for determining magnetic structures.

Inelastic neutron scattering was utilized for the crystal field excitation study in this thesis and the neutron partial differential magnetic cross section can be written as follows [39]:

$$\frac{d^2\sigma}{d\Omega dE'} \propto \frac{k_f}{k_i} F^2(|Q|) S(|Q|, \hbar\omega), \tag{2.23}$$

where $F(|Q|)$ is the magnetic form factor, and $S(|Q|, \hbar\omega)$ is the scattering function. The scattering function gives the relative scattered transition intensities between different CEF levels and is

given by

$$S(|Q|,\hbar\omega)=\sum_{i,i'}\frac{\sum_{\alpha}|\langle i|J_{\alpha}|i'\rangle|^{2}e^{-\beta E_{i}}}{\sum_{j}e^{-\beta E_{j}}}L(E_{i}-E_{i}'+\hbar\omega), \tag{2.24}$$

where $\alpha=x,y,z$, and $L(E_i-E_{i'}+\hbar\omega)$ is a Lorentzian function ensuring energy conservation as the neutron induces transitions between CEF levels with energies E_i and $E_{i'}$. The width of the Lorenztian function arises from a finite instrumental energy resolution.

As discussed in Sec. 1.2, CEF excitations can also be calculated with Eq. 1.7. They provide a way to determine the CEF parameters: we began with an initial guess calculated using a point charge model and the known crystal structure. We then diagonalized the Hamiltonian with these parameters to find the corresponding CEF eigenfunctions and eigenvalues, which allowed us to calculate Eq. 2.24. Finally, we used a least-squares minimization routine to find a set of crystal field parameters that produced the best agreement between the calculated and experimental $S(|Q|,\hbar\omega)$.

3

$NaCaNi_2F_7$

3.1 Summary of $NaCaNi_2F_7$

As discussed in Section. 1.3, perturbations by the inclusion of complicating factors (such as disorder) could have significant impact on magnetic ground state in frustrated pyrochlore materials. New fully fluorine based pyrochlores have been synthesized [40], in which the A site is presumably randomly occupied by two different elements from Group 1 and 2 on the periodic table, and the B site is occupied by a magnetic metal. Such randomness on the A site give rise to a disorder and thus leads to bond disorder around the magnetic site. The study of such disorder effects on selecting its magnetic ground state is quite interesting. In this paper, we present μSR measurements on $NaCaNi_2F_7$ in study the ground state properties.

Our high temperature μSR spectra are dominated by $F\mu F$ oscillations. Density functional theory calculations show a most likely, off-centred, muon site in the $F\mu F$ bonds. Simulations on both centred and off centred muon stopping sites were also performed and found that either site would give essentially same relaxation behaviour compared to our experiment data. As a result, a off centred muon stopping site is preferred.

Our low temperature ZF-μSR spectra shows a partial spin freezing transition around 4 K to a spin glass like state. In the spectra, a robust Gaussian relaxation in early time was observed. This shows that the static field comes from the majority of the nickel moments. We see no signs of oscillations in our ZF-μSR spectra down to 0.075 K, which indicates a broad local field distribution reflecting highly disordered local moments. Through the transition, the fluctuation rate was found decease from 16 MHz to 2 MHz then remains constant down to the lowest temperature, which implies the presence of persistent spin dynamics. Our LF-μSR study

confirmed such spin dynamics with a non-decoupled signal.

Our description for the μSR data was not fully understood: the absence of the minimum in the Kubo-Toyabe function implies a rather complicated field distribution than the single Gaussian in our model. However, the single Gaussian Kubo-Toyabe still parameterized the data reasonably well. Poor agreement of theoretical fitting functions to the data was especially pronounced in our LF data, where the dynamic Gaussian Kubo-Toyabe model could not describe the decoupling behaviour, indicating that the strong collision model may not be applicable in this system. Similar un-decoupled relaxation has also been observed in the Kagomé material $SrCr_xGa_{12-x}O_{19}$ (SCGO), the pyrochlores $Yb_2B_2O_7$ (B = Ti, Ge), and other frustrated systems [41–43]. More work is needed to solve this problem, although this phenomenon seems universal in frustrated magnetic systems.

Publication I: "*μSR study of spin freezing and persistent spin dynamics in $NaCaNi_2F_7$*", Y. Cai, M.N. Wilson, A.M. Hallas, L. Liu, B. A. Frandsen, S. R. Dunsiger, J. W. Krizan, R. J. Cava, Y. J. Uemura, O. Rubel, and G. M. Luke. J. Phys.: Condens. Matter **30** 385802. Reproduced from Ref. [1] with permission, copyrighted by the American Physical Society.

Author Contributions:

- *Experimental Concept*: **Y. Cai**, G.M. Luke
- *Sample Preparation*: J. W. Krizan, R. J. Cava
- *μSR Experiments*: **Y. Cai**, M.N. Wilson, A.M. Hallas, L. Liu, B. A. Frandsen, S. R. Dunsiger, Y. J. Uemura, G. M. Luke
- *DFT calculation* O. Rubel
- *Matlab simulation* **Y. Cai** G. M. Luke
- *Data Analysis*: **Y. Cai**, G. M. Luke
- *Manuscript*: **Y. Cai** M.N. Wilson, A.M. Hallas, S. R. Dunsiger, O. Rubel, Y. J. Uemura, G. M. Luke

setfancy

IOP Publishing Journal of Physics: Condensed Matter

J. Phys.: Condens. Matter **30** (2018) 385802 (8pp) https://doi.org/10.1088/1361-648X/aad91c

μSR study of spin freezing and persistent spin dynamics in $NaCaNi_2F_7$

Y Cai[1,8], M N Wilson[1], A M Hallas[1], L Liu[2], B A Frandsen[2], S R Dunsiger[3], J W Krizan[4], R J Cava[4], O Rubel[5], Y J Uemura[2] and G M Luke[1,6,7,8]

[1] Department of Physics and Astronomy, McMaster University, Hamilton, Ontario L8S 4M1, Canada
[2] Department of Physics, Columbia University, New York, NY, 10027, United States of America
[3] Center for Emergent Materials, The Ohio State University, Columbus, OH, 43210, United States of America
[4] Department of Chemistry, Princeton University, Princeton, NJ, 08544, United States of America
[5] Department of Materials Science and Engineering, McMaster University, Hamilton, Ontario L8S 4M1, Canada
[6] Canadian Institute for Advanced Research, Toronto, Ontario M5G 1M1, Canada
[7] TRIUMF, Vancouver, British Columbia V6T 2A3, Canada

E-mail: caiy42@mcmaster.ca and luke@mcmaster.ca

Received 27 June 2018, revised 3 August 2018
Accepted for publication 8 August 2018
Published 29 August 2018

Abstract

A new pyrochlore compound, $NaCaNi_2F_7$, was recently synthesized and has a single magnetic site with spin-1 Ni^{2+}. We present zero field and longitudinal field muon spin rotation (μSR) measurements on this pyrochlore. Density functional theory calculations show that the most likely muon site is located between two fluorine ions, but off-centre. A characteristic F-μ-F muon spin polarization function is observed at high temperatures where Ni spin fluctuations are sufficiently rapid. The Ni^{2+} spins undergo spin freezing into a disordered ground state below 4 K, with a characteristic internal field strength of 140 G. Persistent Ni spin dynamics are present to our lowest temperatures (75 mK), a feature characteristic of many geometrically frustrated magnetic systems.

Keywords: μSR, pyrochlore, $NaCaNi_2F_7$, frustrated magnetic, spin dynamics

(Some figures may appear in colour only in the online journal)

1. Introduction

A rich variety of magnetic ground states have been realized in the $A_2B_2X_7$ family of geometrically frustrated pyrochlores, including spin glasses, spin liquids, spin ices, as well as long-range-ordered states [1, 2]. Both the A and B sites form corner-sharing tetrahedral networks that can host many different ions which allows broad tuning of the physical interactions. For example, in titanium B-site pyrochlores, placing terbium on the A-site gives an enigmatic spin liquid state, holmium and dysprosium give a classical spin ice state, while gadolinium gives a unique partially ordered state [3–5]. The competing energy scales in these systems (spin anisotropy, exchange, and dipolar interactions) as well as sensitivity to dilute disorder have emerged as extremely important in selecting the ground states of these materials [1, 6].

One interesting state that occurs in some pyrochlores is the spin glass. Although classical spin glass materials have been well studied [8], open questions remain about how such a ground state might emerge in frustrated pyrochlores [1]. Classical spin glass states typically occur in dilute magnetic alloys, where the magnetic state arises from the long-range oscillatory RKKY interaction coupled with a distribution of spin–spin separations [9, 10]. A similar state could occur in pyrochlores arising from local disorder of the spin direction, yielding an effective dilute magnetic system. Other theoretical studies show the possibility that bond disorder in pyrochlores could result in a spin glass state [11–13], which was observed in nominally disorder free $Y_2Mo_2O_7$ [14–16, 53].

Recently, fluoride pyrochlores in the $A_2B_2F_7$ family have been synthesized, expanding the diversity of pyrochlore

[8] Authors to whom any correspondence should be addressed.

setfancy

systems [17–20]. In these materials, the *A* site is presumably randomly occupied by two different elements from Group 1 and 2 on the periodic table, and the *B* site is occupied by a magnetic transition metal. The chemical disorder on the *A* site leads to bond disorder around the magnetic site that is believed to substantially influence their low temperature properties. This new family of magnetic pyrochlores provides a platform for the study of frustrated magnetism where the strong electronic correlations of the transition metals, along with bond disorder caused by the random occupation of the *A* site, may show unique magnetic properties.

All six known members of this family show spin freezing transitions at temperatures below 4 K, with antiferromagnetic Curie–Weiss temperatures larger than 50 K, indicating substantial frustration. AC susceptibility measurements suggest that $NaCaFe_2F_7$, $NaSrFe_2F_7$, and $NaSrMn_2F_7$ each have a spin glass ground state below this spin freezing transition [19]. Neutron scattering shows short range XY-antiferromagnetism in $NaCaCo_2F_7$ and $NaSrCo_2F_7$, with substantial gapless fluctuations through different local XY states [21, 22], and nuclear magnetic resonance shows spin glass like freezing at 3.6 K with thermally activated spin fluctuation at low temperature in $NaCaCo_2F_7$ [23]. The lack of long range order in these Co pyrochlores is suggested to come from ice-like correlated disorder between the Na and Ca or Sr on the *A* site [21]. The spin-1 Ni^{2+} pyrochlore, $NaCaNi_2F_7$, has also been synthesized and shown to have spin freezing at 3.6 K with antiferromagnetic exchange interactions and a corresponding frustration index of $f \sim 36$ [20]. The magnetic entropy integrates to the value for a Ising system, $R\ln(2)$, which is less than expected for an $S = 1$ system, indicating the presence of significant residual entropy. Surprisingly, this Ni pyrochlore releases more entropy than in $NaCaCo_2F_7$ [20]. A bond-disorder induced spin glass state is a likely candidate for the ground state of this system, although no microscopic measurements of the magnetism have been reported [24, 25]. Local magnetic probes that are sensitive to the real space field distribution and to spin fluctuations would be useful to better understand this magnetic state.

In this paper, we present muon spin rotation and relaxation (μSR) measurements on high quality single crystals of $NaCaNi_2F_7$ [20]. μSR can probe both static magnetic order and dynamic spin fluctuations, which has been useful in studying conventional spin glass systems such as Cu_xMn and $AuFe_x$ [26, 27]. In $NaCaNi_2F_7$, we observe the slowing down of the Ni spins when cooling down to 4 K, with a spectra absent of coherent oscillation at base temperature, and dynamic spin fluctuations that persist even at 75 mK. Detailed analysis of the relaxation function shows that these fluctuations are consistent with the persistent spin dynamics commonly seen in other frustrated systems [7, 28–31]. We also performed density functional theory (DFT) [32] electronic structure calculations to determine the muon stopping sites of $NaCaNi_2F_7$, suggesting an off centered muon position between two adjacent fluorine ions, whose positions are distorted (drawn together) by the presence of the muon.

2. Experimental methods and results

2.1. High temperature zero field (ZF)-μSR

The $NaCaNi_2F_7$ sample was grown in an optical floating zone furnace based on a modified Bridgman–Stockbarger method as described previously [20]. We performed μSR measurements on the M15 and M20 beam-lines at the TRIUMF laboratory in Vancouver, Canada, with dilution refrigerator and He-4 gas flow cryostat setups. One large crystal of $NaCaNi_2F_7$ was mounted on the M20 beam-line with the (1 1 0) direction parallel to the incoming beam in the He-4 cryostat low background apparatus. This sample was subsequently sliced into ∼1 mm thick discs along the same (1 1 0) direction and then mounted onto an Ag plate and covered in thin Ag foil for the measurements in the dilution refrigerator. We performed measurements in both zero applied field and with a magnetic field applied along the incident muon spin direction. All the μSR data were fit using the open source μSRfit software package [39].

In μSR measurements, spin polarized muons are implanted into a sample one at a time where they thermalize rapidly in the material while maintaining their polarization. These thermalized muons find a minimum electrostatic potential site where they come to rest and their spins precess in the local magnetic field until they decay with a average lifetime $\tau_\mu = 2.2$ μs, emitting a positron preferentially in the direction of the muon spin. In materials containing fluorine, muons generally thermalize close to these highly electronegative fluorine ions [40]. At high temperature, well above any magnetic transition, where the electronic fluctuations are exchange narrowed and too rapid to contribute to the muon spin relaxation signal, the signal in such compounds typically shows oscillations attributed to the F-μ-F magnetic dipole interaction. This is caused by the dipole–dipole interactions between the muon and the surrounding fluorine nuclei (usually two fluorines). By modelling the simplest configuration of muons lying at the mid-point between two fluorine ions, the muon spin relaxation function $G_{F\mu F}(t)$ can be obtained by averaging over all different orientations of fluorine nuclear dipole moments [40–42]. In a cubic system, this relaxation function is given by,

$$P(t) = A_{\text{total}}(f e^{-(\lambda_1 t)^\beta} G_{F\mu F}(t) + (1-f)e^{-\lambda_2 t}) \quad (1)$$

with

$$\begin{aligned} G_{F\mu F} = {} & 1/6(3 + \cos(\sqrt{3}\omega_d t) \\ & + (1 - 1/\sqrt{3})\cos[((3-\sqrt{3})/2)\omega_d t] \\ & + (1 + 1/\sqrt{3})\cos[((3+\sqrt{3})/2)\omega_d t]). \end{aligned} \quad (2)$$

Here, ω_d is the muon-fluorine dipole frequency, β is a phenomenological stretching parameter, λ_1 is the relaxation rate of the F-μ-F signal that could reflect the combination effects from the slowing down of Ni spin fluctuation at lower temperatures and possible muon hopping between adjacent sites and from the effects of further near neighbours. λ_2 (background) is assumed to be a simple exponential. The fraction f represents the F-μ-F signal fraction and $1 - f$ represents the background

setfancy

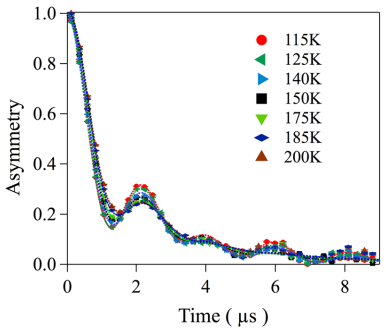

Figure 1. ZF-μSR time spectra measured in $NaCaNi_2F_7$ above 100 K. Oscillations due to the F-μ-F signal are well defined.

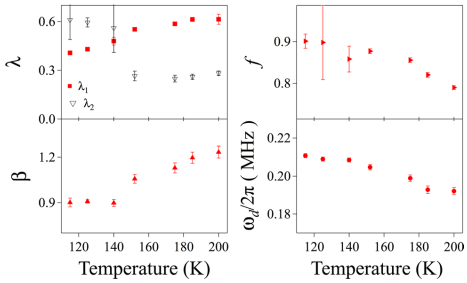

Figure 2. Temperature dependence of the fitting parameters of equation (1) used to fit the high temperature $NaCaNi_2F_7$ ZF μSR data.

fraction not associated with the F-μ-F signal. All the asymmetries are scaled by A_{total} in the following figures.

We show data for our $NaCaNi_2F_7$ sample between 100 and 200 K in figure 1, which is well above the spin freezing temperature of Ni moments. This data shows clear F-μ-F oscillations that we fit using equation (1) to extract the fitting parameters shown in figure 2. Since the frequency is mainly determined by the peak position and not that sensitive to the relaxation rate in the spectra, we allowed the other parameters to freely vary to obtain the best possible fit. The fit value of $\beta \approx 1$ corresponds to the typical exponential behaviour, and the fraction f is close to 90%. The fitted frequency is slightly dependent on temperature as shown in figure 2 and has an average value of $\omega_d/2\pi = 0.201(8)$ MHz over the 120 K–200 K temperature range. The frequency temperature dependence may be due to a subtle change in the muon site, or more likely a trading-off effect in the fitting parameters. This value corresponds to a F-μ-F bond length of $2r = 2.420(4)$ Å [40]. Based on the crystal structure ([20]), the flattened octahedra of NiF_6^{4-} could result in three different F–F equilibrium bonds lengths: 2.656 Å, 2.828 Å and 2.991 Å. Therefore, our data indicates that there is significant local distortion to the fluorine positions caused by the muon. This distortion effect is frequently seen, and is caused by the strength of the electrostatic attraction between the muons and fluorine ions [40, 48, 49].

2.2. DFT calculation on muon site

To better understand the likely muon position, we performed electronic structure calculations. These calculations used the Perdew–Burke–Ernzerhof generalized gradient approximation [33] (GGA) for the exchange-correlation functional with the Vienna *ab initio* simulation program [34–36] and projector augmented-wave potentials [37, 38]. The structure of $NaCaNi_2F_7$ was represented by a pseudo-cubic 88-atom supercell (figure 3(a)) that contains eight formula units. Na and Ca atoms were randomly mixed on the same sub-lattice sites with a ratio of 1:1. The experimental value of the lattice parameter ($a =$ 10.28 Å) was used [20]. The muon was modelled as a proton, i.e. a H atom with one electron subtracted from the model. This strategy was successfully applied in previous studies of muon implantation sites in fluorides [43, 44]. Atomic positions were optimized by minimizing the Hellmann–Feynman forces acting on atoms below 10 meV Å^{-1}. The Brillouin zone was sampled using $2 \times 2 \times 2$ Monkhorst–Pack grid [45]. The cutoff energy for a plane wave expansion was set at 500 eV, which is 25% higher than the value recommended in the pseudo-potential file. The higher cutoff energy was essential for obtaining accurate structural parameters.

Dudarev *et al* [46] GGA+U framework was used to account for strong electronic correlations due to the localized d-orbital for Ni. The effective on-site Coulomb interaction (Hubbard U) between localized d-electrons was set at $U = 6.4$ eV as suggested by Wang *et al* [47]. Nickel atoms were initialized with randomly oriented magnetic moments of magnitude 1 μ_B, which increased up to 1.85 μ_B when a converged electron density was obtained. Our calculation show that the moment is insensitive (± 0.01 μ_B) to the local environment of Ni atoms and to the presence of muons. The net magnetic moment of the supercell remained nearly zero.

Six alternative muon implantation sites were explored as shown in figures 3(e)–(j). The configurations are labeled according to the second nearest-neighbor environment of the muon. Each site was initialized with the muon positioned equidistantly on the line between the fluorine atoms. The DFT total energies of alternative configurations were compared upon completion of the structural optimization. The γ-Ni_2Na_4 configuration (figure 3(g)) is energetically most favorable (see table 1) and its energy separation from other muon sites is much greater than the temperature k_BT at which the experiment was performed. Unlike simple fluorine salts such as LiF where all fluorine atoms are equivalent, it is not the case for the pyrochlore fluorides. As a result, the muon shifts from the midway position between two fluorine atoms. In the case of the γ-Ni_2Na_4 configuration, the μ^+-F bond length disparity is 0.12 Å (table 1). The highest disparity is predicted to occur for the Ca-rich γ-$Ni_2(Na,Ca)_4$ configuration (figure 3), and the disparity vanishes for the β-$Ni_3Na_2Ca_2$ site (figure 3(f)) as a result of the symmetry of the fluorine environment.

2.3. Simulation on muon site

We also performed simulations of the F-μ-F spectra by a simple approach with two fluorines and one muon which

setfancy

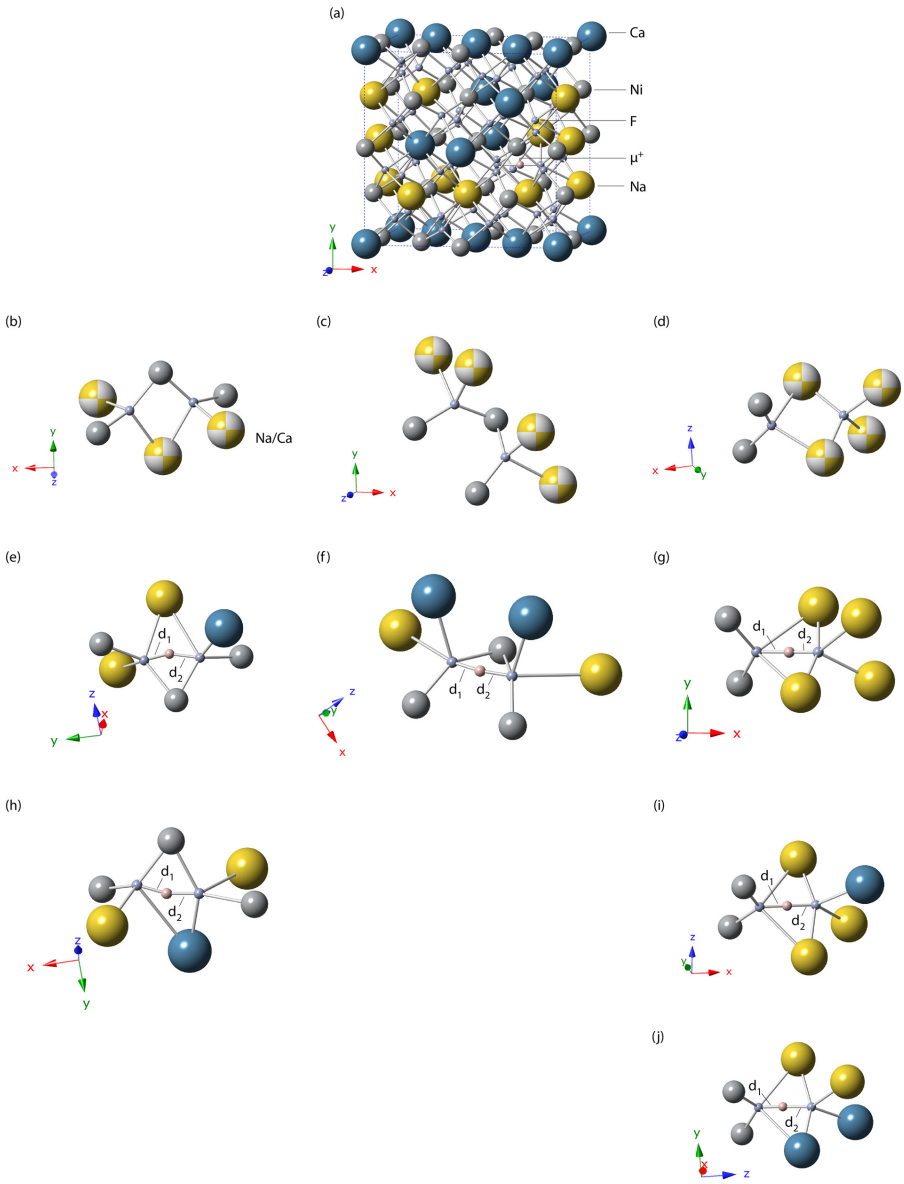

Figure 3. Possible μ^+ implantation sites in $NaCaNi_2F_7$. (a) The crystal structure of an 88-atom supercell. (b)–(d) Generic local environments of fluorine atoms that correspond to shortest (b), second shortest (c), and third shortest (d) F–F distances, which are referred as α-$Ni_3(Na,Ca)_3$, β-$Ni_3(Na,Ca)_4$, and γ-$Ni_2(Na,Ca)_4$ sites, respectively. (e)–(j) The local structure of possible muon sites with a specific nearest-neighbor environment: (e) α-Ni_3Na_2Ca, (f) β-$Ni_3Na_2Ca_2$, (g) γ-Ni_2Na_4, (h) α-Ni_3NaCa_2, (i) γ-Ni_2Na_3Ca, and (j) γ-$Ni_2Na_2Ca_2$. The muon is trapped nearly midway between the two fluorine atoms. The F-μ^+ bond lengths d_1 and d_2 are generally not identical and are sensitive to the nearest-neighbor environment.

setfancy

Table 1. Characteristics of the muon sites in $NaCaNi_2F_7$.

Environment (see figure 3)	Total energy difference (eV)	F-μ^+ bond length (Å)		
		d_1	d_2	$d_1 + d_2$
γ-Ni_2Na_4	0 (reference)	1.22	1.10	2.32
γ-Ni_2Na_3Ca	0.3	1.19	1.13	2.32
α-Ni_3Na_2Ca	0.8	1.09	1.26	2.35
γ-$Ni_2Na_2Ca_2$	1.0	1.07	1.27	2.34
β-$Ni_3Na_2Ca_2$	1.1	1.15	1.16	2.31
α-Ni_3NaCa_2	1.3	1.11	1.18	2.29

gives a three spin quantum mechanical system. The effects of further neighbors are incorporated by multiplying the simulation results by an exponential as also done in equation (1). We confirmed the simulation by comparing with the classical theory calculation of equation (2) assuming a muon site centred between two fluorine atoms, and find good agreement. Then, by offsetting the muon position, we found a possible asymmetric muon site simulation also captures most features of the spectra as shown in figure 4. For this simulation, two fluorine positions were set to $(\pm 0.5, 0, 0)r_{\text{simu}}$, and the off-centred simulation results in a muon site at $(0.1, 0.05, 0.05)r_{\text{simu}}$, with $2r_{\text{simu}} = 2.4$ Å, which gives two different muon-fluorine bond of lengths of $d_1 = 1.45 \pm 0.2$ Å and $d_2 = 0.97 \pm 0.2$ Å. Comparing both the centred and off-centred simulations with the fitting result from μSRfit and the actual data, either site would give essentially the same relaxation behavior and that we cannot distinguish them on this basis. Our conclusion that the muon occupies an off-centre F-μ-F site is based on our DFT calculations which find that the γ-Ni_2Na_4 site has the lowest energy. This site lacks inversion symmetry which then gives no symmetry requirement for a symmetric muon site.

Apart from the expected muon site and its ZF-μSR relaxation function, we also calculated the approximate field magnitude at possible muon sites in the magnetically ordered state. Given the magnetic Ni moments structures from the DFT modelling above, we extended the 16-Ni cell in three different directions into a larger 16∗3∗3∗3-Ni cell by assuming the periodic boundary conditions. The estimated dipolar field strengths are ∼2150 G and 3150 G for the lowest and next lowest energy muon position, corresponding to the γ-Ni_2Na_4 and γ-Ni_2Na_3Ca, respectively. In addition, for randomly oriented Ni moments, field strength at the lowest energy muon position was also calculated to be ∼1500 G. These estimated local fields are at least 15 times bigger than we observed experimentally, as will be shown later, which is evidence for strong dynamics in this compound.

2.4. Low temperature LF-μSR

Typical low temperature μSR spectra of $NaCaNi_2F_7$ are shown in figure 5 at 20 K and 1.75 K in ZF. As the temperature decreases, the spin relaxation increases due to the fluctuations of the magnetic Ni^{2+} moments slowing down and entering the μSR time window [40, 41]. At the lowest temperatures,

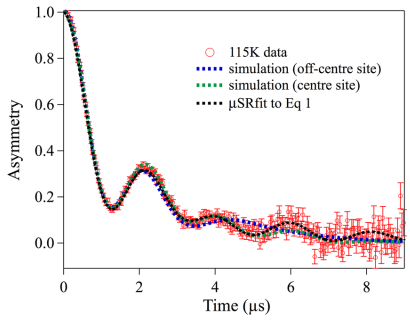

Figure 4. Different μ^+ sites simulation in $NaCaNi_2F_7$ compared with the fitting result. Red points are the 115 K data obtained in TRIUMF, the blue and green dashed lines are non-mid and mid muon site simulation results and the black dashed line is the fitting result from the μSRfit software which assumes a symmetric F-μ-F site.

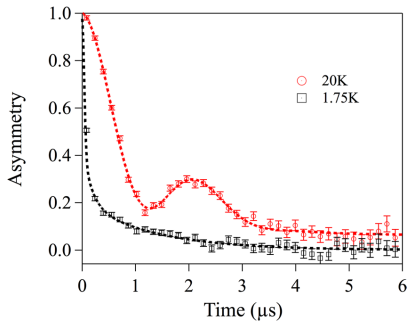

Figure 5. Asymmetry spectra of the μSR data of $NaCaNi_2F_7$ at 20 K and 1.75 K in zero field. The oscillation at 20 K is due to the F-μ-F signal, which is washed out at 1.75 K due to the frozen magnetic Ni moments. These spectra were measured on the M20 beamline.

the F-μ-F signal is washed out by the magnetic field caused by Ni^{2+} moments that relax the muon spin polarization. This is a similar process to the freezing of Ising-like Ho^{3+} in $LiHo_xY_{1-x}F_4$ [42].

Then we moved to dilution refrigerator to focus on the lower temperature range shown in figure 6, where the muons are dominated by fluctuating Ni moments rather than the F-μ-F signal. As the temperature decreases from 6 K to 0.075 K, the change from a single relaxing component to two components with a rapid Gaussian relaxing front end and a slowly relaxing tail indicates the onset of freezing of the Ni moments and a relatively small spin fluctuation rate compared to the relaxation rate from the random distribution of the static local field. In a cubic system, a zero fluctuation rate (static spins) gives a non relaxing 1/3 tail corresponding to the 1/3 probability of the local field being parallel to the initial spin polarization, while a slow, but non-zero, fluctuation rate will relax this 1/3 tail [50].

setfancy

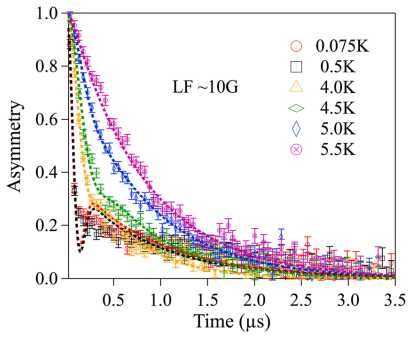

Figure 6. $NaCaNi_2F_7$ μSR data measured at $T = 0.075$, 0.5, 4.0, 4.5, 5.0, and 5.5 K with a longitudinal field of 10 G. Dashed lines show the fits to the dynamical Gaussian Kubo-Toyabe function [50].

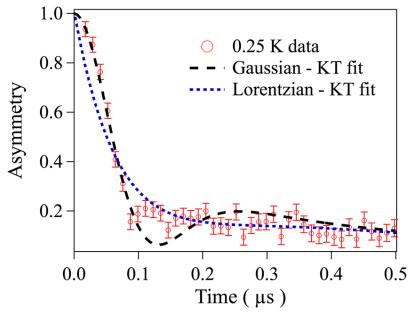

Figure 7. First 0.5 μs of the $NaCaNi_2F_7$ μSR data measured at $T = 0.25$ K, showing the robust Gaussian feature of the fast front end. Dashed lines are the fitting results using a dynamical Gaussian Kubo-Toyabe function (black) and a dynamical Lorentzian Kubo-Toyabe function (blue).

These low temperature measurements were performed in a longitudinal field of 10 G. This small field serves to decouple any contribution to the asymmetry spectra from those muons stopping outside of the sample, leaving only contributions from the electronic magnetism in the sample. This data in figure 6 shows a gradual increase of the static Gaussian relaxation rate with decreasing temperature. The fast relaxation is robustly Gaussian as shown in figure 7, which is typical of dense static moments rather than dilute spins [51]. This indicates that the static field likely comes from the majority of the nickel moments, rather than arising from an effective dilute-system possibly caused by disorder. The data exhibit no sign of oscillations down to 0.075 K, which indicates that the distribution of local fields is very broad and that the frozen moments are highly disordered.

We fit the low temperature data with a dynamical Gaussian Kubo-Toyabe function (DGKTLF) [50] and the results of this analysis are plotted in figure 8. The relaxation rate reflects the width of the static internal field distribution and corresponds to an order parameter for the frozen spin state. The Gaussian relaxation rate also gives us an estimate of local field at the lowest temperature as $\sigma/\gamma_\mu = 140$ G (γ_μ being the gyromagnetic ratio of the muon). Comparing such a relatively small field strength to our simulation result described above of 2150 G, it seems that only a small fraction of the Ni moment freezes, leaving much of the spectral weight still fluctuating on the μSR timescale. The fluctuation rate decreases from 16 MHz at 6 K (above the transition) to 2 MHz below about 4 K and then remains roughly constant down to the lowest temperature (75 mK), which implies the presence of slow dynamics down to our lowest measured temperature in this system. This presence of spin dynamics in $NaCaNi_2F_7$ is also consistent with the existence of residual entropy as the magnetic entropy integrates to roughly R ln(2), which is significantly reduced from R ln(3) [20]. Such persistent spin dynamics are frequently seen in a wide variety of geometrically frustrated systems although their physical origin is not understood.

The minimum of the Kubo-Toyabe function does not agree perfectly with our data, which might mean that the true distribution is somewhat more complicated than a single Gaussian. However, we find that this single Gaussian Kubo-Toyabe nonetheless parameterizes the data reasonably well, and expect that there is little to be gained from attempting a more complicated fit. An example shown in [52] for an increasing number of muon sites, each generating a standard static Gaussian distribution, demonstrates that the sum of the Kubo-Toyabe functions will smooth out the minimum. Here, since interactions between the muon and fluorines will distort the lattice, and Ca/Na site disorder will make muon sites inequivalent, we would expect a such distorted minimum.

To better understand the dynamic/static nature of the local field, we performed longitudinal field (LF) μSR measurements. In a LF-μSR setup, the external field is applied in the direction of the initial muon spin polarization. In this case, the overall field seen by the muons is the vector sum of the internal field and the applied field. If the observed relaxation of the muon polarization comes from static magnetism, applying a longitudinal field will add this external field component to the internal field. This results in a net field seen by the muons that is closer to the direction of the muon spin, reducing the relaxation rate and relaxing asymmetry (called decoupling). In the strong collision model, a static signal will be nearly fully decoupled by an applied field that is a few times larger than the internal field measured in ZF, and we can fit this using a longitudinal field Kubo-Toyabe function. However, if the relaxation of the ZF μSR signal comes from dynamics, the signal will not be decoupled by an applied field of this magnitude, as there is no well-defined weak internal field. In this case, the signal will only slowly decouple, and relaxation will continue to be apparent up to relatively large applied longitudinal fields [26].

Our LF results shown in figure 9 are not well described by the DGKTLF: we only see partial decoupling of the fast relaxation in contrast to expectations based on the ZF analysis. This indicates that a substantial portion of the relaxation comes from spin dynamics, which is inconsistent with the two-component form of the ZF relaxation which implies slow dynamics. The Gaussian nature of the initial relaxation requires quasi-static field, while the lack

setfancy

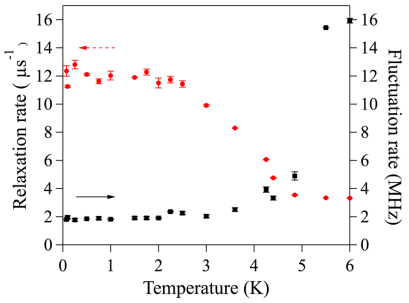

Figure 8. Fitting parameters of for the LF dynamic Gaussian Kubo-toyabe function used to fit the data in figure 6. The relaxation rate (red circles) increases with decreasing temperature up a plateau at 12 μs^{-1}, while the fluctuation rate (black squares) decreases with decreasing temperature to a plateau at 2 MHz.

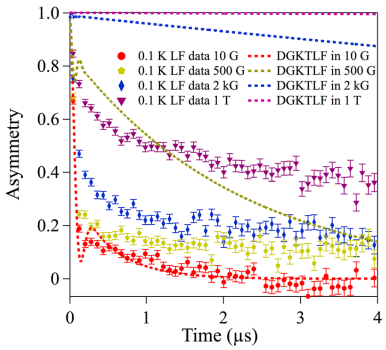

Figure 9. μSR data at 0.1 K in selected fields up to 1 T, and LF Kubo-Toyabe function in the same selected field up to 1 T. These data demonstrate that the static relaxation is not fully decoupled even by large fields. The partially decoupled asymmetry spectra shows the coexistence of static and dynamic local fields acting on the muons.

of decoupling in high fields requires fluctuating fields. A possible resolution of this apparent paradox could be that the strong collision model might not be applicable in this situation as it assumes a field independent fluctuation (collision) rate. Our observations imply that the application of a LF enhances the spin fluctuations, which would also end up with a non-decoupled signal. This behaviour is reminiscent of previous results in the Kagome material $SrCr_xGa_{12-x}O_{19}$, the pyrochlores $Yb_2B_2O_7$ (B = Ti,Ge), and other frustrated systems, where the observed gaussian relaxation was not decoupled by appropriate longitudinal fields [28, 54, 55].

3. Conclusion

In conclusion, we have presented a μSR study of spin dynamics in $NaCaNi_2F_7$. We found a partial spin freezing transition at 4 K to a spin-glass like state involving the majority of the Ni moments. We also observed a residual temperature independent spin fluctuation rate down to 0.075 K, which shows that there are persistent spin fluctuations at low temperature, as is common in highly frustrated systems. As this system combines intense geometric frustration with chemical disorder caused by randomly distributed Ca and Na ions on the *A*-site, the underlying cause of the dynamics is not yet fully understood. Our data, along with previous work showing existence of residual entropy and similar results in the titanium pyrochlores, suggest that bond disorder in frustrated systems results in a glassy ground state [20]. This similarity offers a great opportunity to explore the related properties of the new transition metal fluoride pyrochlores and the titanium oxide pyrochlore family. Finally, our DFT calculations and simulations suggest the muon position in $NaCaNi_2F_7$ is somewhat off centre between two inequivalent fluorine ions. The calculated field at the simulated muon site is 15 times larger than we observe experimentally, providing evidence that the full Ni moment is not frozen, and that much of the fluctuations remain above the μSR time window. Further neutron scattering studies on the magnetic excitations are needed to explore the magnetic anisotropy, which will also be helpful for understanding the universal persistent dynamics in frustrated magnets.

Acknowledgments

We greatly appreciate useful discussions with Wen Huang. We also greatly appreciate the support of personnel at TRIUMF during the μSR measurements. Work at Princeton was supported by the US Department of Energy, Division of Basic Energy Sciences, through the Institute for Quantum Matter, grant DE-FG02-08ER46544. Work of the Columbia group has been supported by NSF DMR-1436095 (DMREF) and NSF DMR-1610633, and Reimei Project of Japan Atomic Energy Agency. The DFT calculations were performed using computational resources of the Thunder Bay Regional Research Institute, Lakehead University, and Compute Canada (Calcul Quebec).

Work at McMaster (G M Luke, O Rubel) was supported by the Natural Sciences and Engineering Research Council of Canada.

ORCID iDs

Y Cai https://orcid.org/0000-0002-1374-5314

References

[1] Gardner J S, Gingras M J P and Greedan J E 2010 *Rev. Mod. Phys.* **82** 53
[2] Hallas A M, Gaudet J and Gaulin B D 2018 *Ann. Rev. Condens. Matter Phys.* **9** 105–24
[3] Gardner J S *et al* 1999 *Phys. Rev. Lett.* **82** 1012
[4] Harris M J, Bramwell S T, McMorrow D F, Zeiske T and Godfrey K W 1997 *Phys. Rev. Lett.* **79** 2554
[5] Ramirez A P, Hayashi A, Cava R J, Siddharthan R and Shastry B S 1999 *Nature* **399** 333

setfancy

[6] Stewart J R, Ehlers G, Wills A S, Bramwell S T and Gardner J S 2004 *J. Phys.: Condens. Matter* **16** 28
[7] Hallas A M, Gaudet J, Butch N P, Tachibana M, Freitas R S, Luke G M, Wiebe C R and Gaulin B D 2016 *Phys. Rev.* B **93** 100403
[8] Binder K and Young A P 1986 *Rev. Mod. Phys.* **58** 801
[9] Ruderman M A and Kittel C 1954 *Phys. Rev.* **96** 99
[10] Yosida K 1957 *Phys. Rev.* **106** 893
[11] Saunders T E and Chalker J T 2007 *Phys. Rev. Lett.* **98** 157201
[12] Andreanov A, Chalker J T, Saunders T E and Sherrington D 2010 *Phys. Rev.* B **81** 014406
[13] Shinaoka H, Tomita Y and Motome Y 2011 *Phys. Rev. Lett.* **107** 047204
[14] Greedan J E, Sato M, Yan X and Razavi F S 1986 *Solid State Commun.* **59** 895–7
[15] Silverstein H J *et al* 2014 *Phys. Rev.* B **89** 054433
[16] Thygesen P M M *et al* 2017 *Phys. Rev. Lett.* **118** 067201
[17] Krizan J W and Cava R J 2014 *Phys. Rev.* B **89** 214401
[18] Krizan J W and Cava R J 2015 *J. Phys.: Condes. Matter* **27** 296002
[19] Sanders M B, Krizan J W, Plumb K W, McQueen T M and Cava R J 2017 *J. Phys.: Condens. Matter* **29** 045801
[20] Krizan J W and Cava R J 2015 *Phys. Rev.* B **92** 014406
[21] Ross K A, Krizan J W, Rodriguez-Rivera J A, Cava R J and Broholm C L 2016 *Phys. Rev.* B **93** 014433
[22] Ross K A, Brown J M, Cava R J, Krizan J W, Nagler S E, Rodriguez-Rivera J A and Stone M B 2017 *Phys. Rev.* B **95** 144414
[23] Sarkar R, Krizan J W, Brückner F, Andrade E C, Rachel S, Vojta M, Cava R J and Klauss H-H 2017 *Phys. Rev.* B **96** 235117
[24] Andrade E C, Hoyos J A, Rachel S and Vojta M 2018 *Phys. Rev. Lett.* **120** 097204
[25] Li F-Y and Chen G 2018 *Phys. Rev.* B **98** 045109
[26] Uemura Y J, Yamazaki T, Hayano R S, Nakai R and Huang C Y 1980 *Phys. Rev. Lett.* **45** 583
[27] Uemura Y J, Yamazaki T, Harshman D R, Senba M and Ansaldo E J 1985 *Phys. Rev.* B **31** 546
[28] Uemura Y J *et al* 1994 *Phys. Rev. Lett.* **73** 3306
[29] Yaouanc A, Dalmas de Reotier P, Glazkov V, Marin C, Bonville P, Hodges J A, Gubbens P C M, Sakarya S and Baines C 2005 *Phys. Rev. Lett.* **95** 047203
[30] Lago J, Lancaster T, Blundell S J, Bramwell S T, Pratt F L, Shirai M and Baines C 2005 *J. Phys.: Condens. Matter* **17** 979
[31] Dunsiger S R, Kiefl R F, Chakhalian J A, Greedan J E, MacFarlane W A, Miller R I, Morris G D, Price A N, Raju N P and Sonier J E 2006 *Phys. Rev.* B **73** 172418
[32] Kohn W and Sham L J 1965 *Phys. Rev.* **140** A1133
[33] Perdew J P, Burke K and Ernzerhof M 1996 *Phys. Rev. Lett.* **77** 3865
[34] Kresse G and Hafner J 1993 *Phys. Rev.* B **47** 558
[35] Kresse G and Furthmüller J 1996 *Phys. Rev.* B **54** 11169
[36] Kresse G and Furthmüller J 1996 *Comput. Mater. Sci.* **6** 15–50
[37] Kresse G and Joubert D 1999 *Phys. Rev.* B **59** 1758
[38] Blöchl P E 1994 *Phys. Rev.* B **50** 17953
[39] Suter A and Wojek B M 2012 Musrfit: a free platform-independent framework for μSR data analysis *Phys. Procedia* **30** 69
[40] Brewer J H, Kreitzman S R, Noakes D R, Ansaldo E J, Harshman D R and Keitel R 1986 *Phys. Rev.* B **33** 7813
[41] Noakes D R, Ansaldo E J and Luke G M 1993 *J. Appl. Phys.* **73** 5666
[42] Rodriguez J, Aczel A A, Carlo J P, Dunsiger S R, MacDougall G J, Russo P L, Savici A T, Uemura Y J, Wiebe C R and Luke G M 2010 *Phys. Rev. Lett.* **105** 107203
[43] Bernardini F, Bonfà P, Massidda S and De Renzi R 2013 *Phys. Rev.* B **87** 115148
[44] Möller J S, Ceresoli D, Lancaster T, Marzari N and Blundell S J 2013 *Phys. Rev.* B **87** 121108
[45] Monkhorst H J and Pack J D 1976 *Phys. Rev.* B **13** 5188
[46] Dudarev S L, Botton G A, Savrasov S Y, Humphreys C J and Sutton A P 1998 *Phys. Rev.* B **57** 1505–9
[47] Wang L, Maxisch T and Ceder G 2006 *Phys. Rev.* B **73** 195107
[48] Noakes D R, Ansaldo E J, Kreitzman S R and Luke G M 1993 *J. Phys. Chem. Solids* **54** 785–92
[49] Luke G M, Kiefl R F, Kreitzman S R, Brewer J H, Noakes D R, Celio M, Keitel R, Uemura Y J, Harshman D R and Jaccarino V 1986 *Hyperfine Interact.* **1** 29–34
[50] Uemura Y J 1998 μSR relaxation functions in magnetic materials *Muon Science: Muons in Physics, Chemistry and Materials* ed S L Lee *et al* (New York: Taylor & Francis)
[51] Kubo R and Toyabe T 1967 *Magnetic Resonance and Relaxation* ed R Blinc (Amsterdam: North-Holland)
[52] Noakes D R, Ismail A, Ansaldo E J, Brewer J H, Luke G M, Mendels P and Poon S J 1995 *Phys. Lett.* A **199** 107–12
[53] Dunsiger S R *et al* 1996 *Phys. Rev.* B **54** 9019
[54] D'Ortenzio R M *et al* 2013 *Phys. Rev.* B **88** 134428
[55] Hallas A M *et al* 2016 *Phys. Rev.* B **93** 104405

4

$Er_3Ga_5O_{12}$

4.1 Summary of $Er_3Ga_5O_{12}$

In this paper, we present neutron scattering, magnetometry and μSR measurements of $Er_3Ga_5O_{12}$. Our $Er_3Ga_5O_{12}$ samples were grown by Floating Zone Optical Image Furnaces at McMaster University as described in Section. 2.1. $Er_3Ga_5O_{12}$ has a cubic structure with corner-sharing triangular motifs in three dimensions. A previous study found an antiferromagnetic transition at around 0.8 K [44]. We sought to further investigate this antiferromagnetic transition by measuring the crystal electric field excitations to uncover the magnetic ground state in order to infer the frustration effect in this three dimensional frustrated magnet. We used inelastic neutron scattering measurements at selected temperatures with 30 meV and 120 meV neutron beams, which allowed us to measure the crystal electric field excitations. We were able to determine the crystal field Hamiltonian of this material, including the crystal field levels, ground state wave function and the spin anisotropy. We also performed neutron powder diffraction measurements below its magnetic transition temperature to determine the ground state magnetic structure. Furthermore, we performed specific heat measurement and μSR measurements to characterize the low energy magnetic modes, and possible dynamical magnetic component in such magnetic ordered state.

All seven crystalline electric field excitations were identified from inelastic neutron scattering measurements, from which we have determined the CEF Hamiltonian, indicating an Ising-like anisotropy ground state. This Ising-like anisotropy ground state is in agreement with our specific heat measurements where the entropy is approaching $Rln(2)$. Rietveld refinements of neutron powder diffraction reveal that $Er_3Ga_5O_{12}$ orders into the Γ_3 magnetic structure, with ordered

moment $\mu_{ord} = 5.24(4)\ \mu_B$. This ordered moment matches the value of saturated moment along the local [100] Ising direction obtained from our deduced Hamiltonian with $\mu_{Ising} = 5.61\ \mu_B$.

Magnetic susceptibility shows a maximum around 0.8 K, where the long-range ordering transition was also identified by zero-field specific heat, however, this transition is strongly field dependent with an overestimated critical field of H_c (0 K) $\sim$ 7.08 kG. The magnetic susceptibility at high temperatures (150-300 K) is well described by a Curie-Weiss Law with a Weiss temperature θ_{CW} = -15 K and an effective Er moment of 9.57 μ_B; the latter corresponds well to the expected value of 9.59 μ_B for an isolated Er^{3+} ion. The Curie-Weiss fit to the magnetic susceptibility in the low temperature regime (2-5 K) results in a Weiss temperature θ'_{CW} = -0.94 K. The close agreement between θ'_{CW} and the ordering temperature indicates that $Er_3Ga_5O_{12}$ is not a strongly-frustrated system.

We also found that ZF-μSR is insensitive to the 0.8 K ordering transition in this material. We note that the ZF-μSR data exhibit no sign of oscillations down to 30 mK, which is unexpected in a magnetically-ordered state. There is either no change in the temperature-dependence of the relaxation rate at $\sim$ 0.8 K and it appears to be temperature-independent below $\sim$ 20 K. Similar low-temperature relaxation plateaus have been observed in a variety of frustrated magnets with ordered ground states [45–48], but their microscopic origin is still unclear [49]. This may be due to the different time-scales of the techniques, but this should be tested.

Our observation shows that the antiferromagnetic ground state is fragile that $Er_3Ga_5O_{12}$. Our results indicate that $Er_3Ga_5O_{12}$ is an excellent model system for studying the complex metamagnetism expected for a multi-axis antiferromagnet.

Preprint I: "*Crystal fields and magnetic structure of the Ising antiferromagnet* $Er_3Ga_5O_{12}$", Y. Cai, M.N. Wilson, J. Beare, C. Lygouras, G. Thomas, D.R. Yahne, K. Ross, K.M. Taddei, G. Sala, H.A. Dabkowska, A. A. Aczel, and G. M. Luke. *arXiv*:1905.03687 (2019).

Author Contributions:

- *Experimental Concept*: **Y. Cai**, G.M. Luke
- *Sample Preparation*: **Y. Cai**, C. Lygouras, G. Thomas, H. Dabkowska, G.M. Luke
- *μSR Experiments*: **Y. Cai**, M.N. Wilson, J. Beare, G.M. Luke
- *Neutron Experiments*: **Y. Cai**, K.M. Taddei, G. Sala, A. A. Aczel, G.M. Luke
- *Specfic heat Experiments*: D.R. Yahne, K. Ross
- *Data Analysis*: **Y. Cai**, A. A. Aczel, G.M. Luke

- *Manuscript*: **Y. Cai**, A. A. Aczel, G.M. Luke

Crystal fields and magnetic structure of the Ising antiferromagnet $Er_3Ga_5O_{12}$

Y. Cai,[1] M.N. Wilson,[1] J. Beare,[1] C. Lygouras,[1] G. Thomas,[1] D.R. Yahne,[2] K. Ross,[2,3] K.M. Taddei,[4] G. Sala,[4] H.A. Dabkowska,[5] A.A. Aczel,[4,6,*] and G.M. Luke[1,3,7,†]

[1] *Department of Physics and Astronomy, McMaster University, Hamilton, ON L8S 4M1, Canada*
[2] *Department of Physics, Colorado State University, Fort Collins, CO 80523, USA*
[3] *Canadian Institute for Advanced Research, Toronto, ON M5G 1M1, Canada*
[4] *Neutron Scattering Division, Oak Ridge National Laboratory, Oak Ridge, TN 37831, USA*
[5] *Brockhouse Institute for Materials Research, McMaster University, Hamilton, ON L8S 4M1, Canada*
[6] *Department of Physics and Astronomy, University of Tennessee, Knoxville, TN 37996, USA*
[7] *TRIUMF, Vancouver, BC V6T 2A3, Canada*

Rare earth garnets are an exciting playground for studying the exotic magnetic properties of the frustrated hyperkagome lattice. Here we present a comprehensive study of the single ion and collective magnetic properties of the garnet $Er_3Ga_5O_{12}$. Using inelastic neutron scattering, we find a crystal field ground state doublet for Er^{3+} with strong Ising anisotropy along local [100] axes. Magnetic susceptibility and heat capacity measurements provide evidence for long-range magnetic ordering with $T_N = 0.8$ K, and no evidence for residual entropy is found when cooling through the ordering transition. Neutron powder diffraction reveals that the ground state spin configuration corresponds to the six-sublattice, Ising antiferromagnetic state (Γ_3) common to many of the rare earth garnets. Our results indicate that $Er_3Ga_5O_{12}$ is an excellent model system for studying the complex metamagnetism expected for a multi-axis antiferromagnet.

INTRODUCTION

Frustrated magnets are materials in which the competing pairwise interactions between magnetic moments cannot be satisfied simultaneously. The pyrochlore lattice, which consists of corner-sharing tetrahedra, represents one of the canonical three-dimensional (3D) frustrated geometries[1–3]. Amongst this large family of materials, the rare earth pyrochlores of the form $R_2B_2O_7$ (R = rare earth, B = non-magnetic cation) have received the most attention due to their rich variety of magnetic ground states and excitations. This large variation between states, arising from the interplay of exchange couplings, dipolar interactions, and single ion anisotropy, leads to spin glasses[4, 5], spin liquids[6–8], spin ices[9], order-by-disorder[10, 11], magnetic moment fragmentation[12, 13], and conventional long-range magnetic ordering.

Another common 3D frustrated architecture, based on corner-sharing triangles, is the hyperkagome lattice. This geometry is realized by the rare earth sublattice in the garnets $R_3(Ga,Al)_5O_{12}$, and is illustrated in Fig. 1(a). The most commonly studied material in this family is the Heisenberg garnet $Gd_3Ga_5O_{12}$, as it hosts a spin liquid state above a freezing temperature of $T_g = 0.14$ K[14–22] that has recently been argued to arise from hidden multipolar order[23]. A Kagome spin ice state with extensive degeneracy has also been proposed for Ising garnets when the moments lie along the local [110] axes[24], but this exotic state has yet to be uncovered in the laboratory. Finally, complex metamagnetic behavior has been predicted and observed for garnets with strong Ising anisotropy along local [100] axes[25–28].

Establishing the hiearchy of interactions in $R_3(Ga,Al)_5O_{12}$ is an important step towards gaining a detailed understanding of the magnetic properties of these materials. As in the case of rare earth pyrochlores, exchange couplings, dipolar interactions, and single ion anisotropy arising from crystal fields are all expected to be important. While the single ion anisotropy is typically the easiest contribution to quantify, surprisingly little is known with certainty for this class of materials. Most previous crystal field studies were performed using optical spectroscopy since these materials were first investigated back in the 1960s-1970s[29–34], although it is not always straightforward to differentiate between phonons and low-lying crystal field levels with this technique. It is now understood that inelastic neutron scattering is the premier method for measuring crystal field excitations, as they can be unambiguously identified due to a momentum transfer (Q) dependence that is different from phonons. Despite this significant advantage, only the crystal field parameters of $Ho_3Ga_5O_{12}$[35] have been determined with inelastic neutron scattering to-date.

The collective magnetic properties of many rare earth aluminum and gallium garnets were also investigated several decades ago, typically with a combination of magnetic susceptibility, heat capacity, and neutron diffraction measurements. Many of these materials achieve six-sublattice antiferromagnetic long-range order corresponding to the Γ_3 irreducible representation in Kovalev's notation[36] at temperatures $T < 3$ K[37–39]. While this ordered state is consistent with expectations for dipolar interactions between local [100] Ising moments[40], the collective magnetic properties of several systems remain poorly understood. For instance, there is a sharp λ anomaly in the specific heat of $Yb_3Ga_5O_{12}$ at $T_N = 54$ mK[41] initially thought to be

indicative of long-range magnetic order, but muon spin relaxation[41] and Mossbauer spectroscopy[42] measurements show no evidence for the expected order. Neutron diffraction has also revealed that the magnetic ground state of $Nd_3Ga_5O_{12}$ corresponds to the Γ_4 irreducible representation[43], which is still consistent with local [100] Ising moments but not predicted by Capel's original theory[40]. Finally, revisiting the collective magnetic properties of these materials with modern neutron scattering instrumentation has led to some surprises. In particular, $Ho_3Ga_5O_{12}$ was initially reported to order in the Γ_3 magnetic structure[39], but recent neutron scattering measurements found the coexistence of diffuse magnetic scattering with the Γ_3 magnetic Bragg peaks in zero field, with a reasonably small field of 20 kG being enough to suppress the diffuse scattering[44]. This finding provides strong motivation to reexamine the collective magnetic properties of other Ising garnets, as they may also be more complex than first proposed in the earlier studies.

In this work, we address the magnetism in $Er_3Ga_5O_{12}$ using multiple techniques. Using inelastic neutron scattering, we find a doublet crystal field ground state for Er^{3+} with strong Ising anisotropy along local [100] axes. We also investigate the collective magnetic properties of this system with magnetic susceptibility, heat capacity, and neutron diffraction measurements, which reveal Γ_3 antiferromagnetic ordering with $T_N = 0.8$ K. No diffuse scattering is observed below T_N and no residual entropy is found when cooling through the ordering transition, which are both consistent with a conventional ordered state.

CRYSTAL GROWTH AND EXPERIMENTAL DETAILS

Single crystals of $Er_3Ga_5O_{12}$ were grown by the traveling-solvent floating-zone (TSFZ) technique at McMaster University. Stoichiometric mixtures of high-purity raw materials Er_2O_3 (99.99%) and Ga_2O_3 (99.999%) were ground, pressed hydrostatically into rods and heated in air at 1200°C for 8 hours. No sample mass loss was observed before or after heating. Crystal growth was performed at a growth rate of 5 mm/hr and 1 atm overpressure under Argon gas, resulting in a large, transparent, pink crystal with a length of 3 cm. The crystals were determined to be single phase $Er_3Ga_5O_{12}$ by performing powder x-ray diffraction measurements on a crushed portion of the crystals. We collected magnetic susceptibility measurements from 0.48 K to 300 K on a small cut single crystal with the magnetic field applied along the [110] direction using a Quantum Design Magnetic Property Measurement System XL-3 equipped with an iQuantum He^3 Insert for measurements below 2 K. We also measured the specific heat of a single crystal between 0.1 K and 4 K using a Quantum Design Physical Property Measurement System with a dilution fridge insert.

The inelastic neutron scattering (INS) experiment to measure the crystal field levels was performed using the SEQUOIA spectrometer[45] at the Spallation Neutron Source of Oak Ridge National Laboratory (ORNL) using 9.4 g of crushed single crystals loaded into an Al cylindrical can. All data were collected with incident energies $E_i = 30$ meV and 120 meV, with corresponding fine Fermi chopper frequencies of 240 Hz and 600 Hz, resulting in instrumental energy resolutions of 0.65 meV and 2.1 meV (full-width half-maximum) respectively at the elastic line. A closed cycle refrigerator was used to achieve a base temperature of 4 K. The neutron powder diffraction (NPD) experiment to investigate the magnetic structure was carried out on the HB-2A powder diffractometer[46] at the High Flux Isotope Reactor of ORNL using the same sample measured in the SEQUOIA experiment. A cryostat with a He^3 insert was used to achieve a base temperature of 0.3 K. A collimation of open-21′-12′ was used in this experiment, and the FULLPROF software suite[47] was used to perform all structural and magnetic refinements reported in this work.

Muon spin relaxation measurements were performed at TRIUMF, Canada on the the M20 and M15 beamlines with He^4 gas flow cryostat (base $T = 1.5$ K) and dilution fridge (base $T = 30$ mK) setups. A single crystal of $Er_3Ga_5O_{12}$ was mounted on the M20 beamline with a low background apparatus in the He^4 cryostat using aluminum backed mylar tape. Another single crystal sample was sliced into ∼1 mm thick discs and mounted onto an Ag plate and covered in thin Ag foil for the measurements on the M15 beamline. All measurements were performed with zero applied field (ZF) and all the μSR data were fit by the open source μSRfit software package[48].

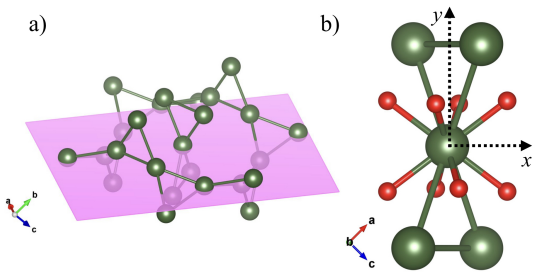

FIG. 1. (a) Corner-sharing triangular network of Er^{3+} ions in $Er_3Ga_5O_{12}$; the $0\bar{1}1$ crystallographic plane is shown in pink. (b) The local environment of an Er^{3+} ion in $Er_3Ga_5O_{12}$, this schematic is appropriate for the ion at site (0.25, 0.125, 0). Each Er^{3+} ion has D_2 orthorhombic point symmetry and is surrounded by eight O^{2-} ions.

RESULTS AND DISCUSSION

Inelastic neutron scattering

In $Er_3Ga_5O_{12}$, the Er^{3+} ions occupy two interpenetrating, corner-sharing triangular sublattices as shown in Fig. 1(a). Each Er^{3+} ion is surrounded by eight nearest-neighbor oxygen ions, leading to dodecahedral local geometry and D_2 orthorhombic point symmetry as shown in Fig. 1(b) for Er site (0.25, 0.125, 0). According to Hund's rules, the ground state multiplet of an Er^{3+} ion is $J = 15/2$. The $(2J + 1)$ levels associated with this multiplet are split into eight Kramers doublets due to the crystalline electric fields (CEFs) generated predominantly by the neighboring oxygen ions. To reduce the number of CEF parameters in the Hamiltonian to nine, the quantization axis z can be chosen to coincide with the anticipated Ising axis [010], while x and y are assigned to the other local twofold rotation axes [101] and [10$\bar{1}$]. Assuming no crystallographic distortion, the CEF Hamiltonian is written as:

$$\hat{\mathcal{H}}_{D_2}^{CEF} = \sum_{i=0,2} B_2^i \hat{O}_2^i + \sum_{i=0,2,4} B_4^i \hat{O}_4^i + \sum_{i=0,2,4,6} B_6^i \hat{O}_6^i, \quad (1)$$

where the B_n^i are the crystal field parameters to be determined experimentally and $\hat{O}_n^i$ are the Stevens operators[49]. For a given set of crystal field parameters, the Hamiltonian in Eq. (1) can be diagonalized to find the corresponding CEF energy levels and wavefunctions that can be probed directly with inelastic neutron scattering. The unpolarized double differential cross-section for magnetic neutron scattering can be written as follows[50]:

$$\frac{d^2\sigma}{d\Omega dE_f} = C\frac{k_f}{k_i} f^2(Q) S(Q, \hbar\omega), \quad (2)$$

where Ω is the scattered solid angle, E_f is the final neutron energy, $k_{f/i}$ is the scattered/incident momentum of the neutron, C is a constant, $f(Q)$ is the magnetic form factor, and $S(Q, \hbar\omega)$ is the scattering function. The scattering function provides the relative scattered transition intensities between different CEF levels and is given by[51]:

$$S(Q, \hbar\omega) = \sum_{i,i'} \frac{(\sum_\alpha |\langle i|J_\alpha|i'\rangle|^2) e^{-\beta E_i}}{\sum_j e^{-\beta E_j}} L(E_i - E_i' + \hbar\omega), \quad (3)$$

where $\alpha = x, y, z$, and $L(E_i - E_i' + \hbar\omega)$ is a Lorentzian function ensuring energy conservation as the neutron induces transitions between CEF levels with energies E_i and E_i'.

In Fig. 2, we present the INS data of $Er_3Ga_5O_{12}$ collected at $T = 4$ and 90 K with incident energy $E_i = 30$ or 120 meV. As CEF excitations arise from unpaired electrons and therefore have a magnetic origin, they should

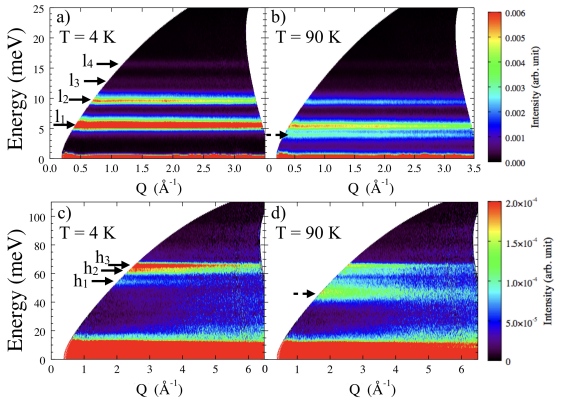

FIG. 2. Inelastic neutron scattering data for $Er_3Ga_5O_{12}$ presented as color contour plots, with (a) $E_i = 30$ meV and $T = 4$ K, (b) $E_i = 30$ meV and $T = 90$ K, (c) $E_i = 120$ meV and $T = 4$ K, and (d) $E_i = 120$ meV and $T = 90$ K. Two bands of crystal field excitations are observed in the 4 K data. The lower energy band consists of four modes while the higher energy band consists of three modes; all seven of these excitations are indicated by black arrows in panels (a) and (c). A temperature of 90 K is sufficient to thermally-populate the lowest two crystal field excitations, which generates virtual transitions in these higher-temperature datasets. The virtual transitions are indicated by dashed arrows in panels (b) and (d).

decrease in intensity with increasing momentum transfer (Q) following the square of the Er^{3+} magnetic form factor. We have identified seven possible CEF excitations in the $E_i = 30$ and 120 meV datasets, as indicated by the black arrows in Fig. 2(a) and (c). To prove they have a magnetic origin, we considered constant-E cuts of these datasets, as shown in Fig. 3(a) and (b) for the five most intense modes. The Q-dependence of the intensity for all seven excitations indeed matches expectations for magnetic scattering. Therefore, we attribute these modes to the seven excited doublets of the $J = 15/2$ ground state multiplet for Er^{3+}. These levels are divided into two distinct bands, with three modes located at much higher energies than the other four.

In order to determine the CEF parameters, we began with an initial guess calculated using a point charge model[49] and the known crystal structure. We then diagonalized the Hamiltonian with these parameters to find the corresponding CEF eigenfunctions and eigenvalues, which allowed us to calculate $S(Q, \hbar\omega)$. Finally, we used a least-squares minimization routine to find a set of crystal field parameters that produced the best agreement between the calculated and experimental $S(Q, \hbar\omega)$.

Fig. 3(c) and (d) show constant-Q cuts of the $E_i = 30$ and 120 meV data, indicated by open red circles, with integration ranges of $Q = [0.5, 3.5]$ Å^{-1} and $[0.5, 4.5]$ Å^{-1}

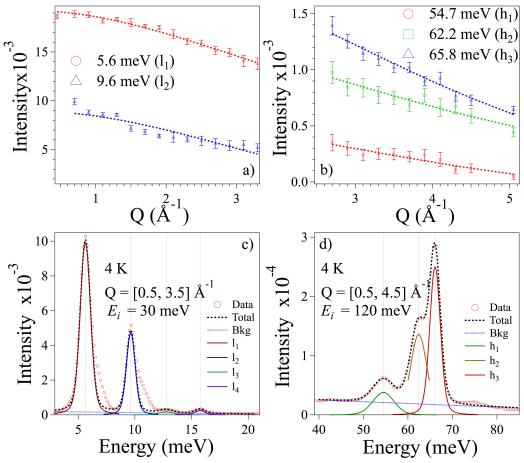

FIG. 3. (a) The Q-dependence of the two most intense CEF excitations from the lower energy band. (b) The Q-dependence of the three CEF excitations from the higher energy band. The intensity of all five of these excitations decreases with increasing Q, which is consistent with a magnetic origin. (c) The neutron scattering intensity as a function of energy transfer with $E_i = 30$ meV, revealing the presence of four CEF excitations. (d) The neutron scattering intensity as a function of energy transfer with $E_i = 120$ meV, revealing the presence of three additional CEF excitations. The best fit to these combined datasets, yielding the crystal field parameters presented in Table II, is indicated by the solid curves in these two panels.

TABLE I. The CEF energy levels for $Er_3Ga_5O_{12}$ from the point charge calculation ($point_{cal}$), the INS experiment (exp), and the refined CEF Hamiltonian ($Fitted$). The CEF wavefunctions for the ground state doublet, the g tensor components, and the saturated moment μ_{Ising} along the local [100] Ising direction obtained from the refined CEF Hamiltonian.

$point_{cal}$(meV)	0	9.89	18.10	22.40	27.79	29.10	43.36	45.13
exp (meV)	0	5.72	9.79	13.09	16.03	53.75	61.42	65.13
$Fitted$ (meV)	0	5.78	9.78	12.92	16.07	56.08	59.43	64.07

$$\phi_0^{\pm} = -0.0068 \mid \mp\frac{13}{2}\rangle - 0.0490 \mid \mp\frac{9}{2}\rangle - 0.0335 \mid \mp\frac{5}{2}\rangle + 0.0691 \mid \mp\frac{1}{2}\rangle - 0.1418 \mid \pm\frac{3}{2}\rangle - 0.6085 \mid \pm\frac{7}{2}\rangle - 0.7580 \mid \pm\frac{11}{2}\rangle + 0.1635 \mid \pm\frac{15}{2}\rangle$$

$[g_x, g_y, g_z] = [1.42, 0.03, 11.21]$, $\mu_{Ising} = \frac{g_z}{2}\mu_B = 5.61\mu_B$

respectively. The best fit curves are superimposed on the data and account for the experimental features quite well, with the exception of the asymmetric peak shapes of the lowest two CEF excitations that are likely a consequence of the instrumental resolution function. Table I presents the CEF energy levels corresponding to our point charge calculation, the CEF energy levels measured directly by INS, and the CEF energy levels, ground state doublet wavefunctions, g-tensor components ($g_z = 2g_J|\langle\phi_0^{\pm}|J_z|\phi_0^{\pm}\rangle|$; $g_x, g_y = 2g_J|\langle\phi_0^{\pm}|J_x, -i * J_y|\phi_0^{\mp}\rangle|$), and the saturated magnetic moment along the Ising direction obtained from our best fit to the INS data. These g-tensor values determined by our INS data are in broad agreement with those obtained from magnetic susceptibility[52, 53]. The crystal field parameters corresponding to both the point charge calculation and our best fit are also shown in Table II. The ground state doublet wavefunctions and g-tensor components for Er^{3+} are indicative of a strong Ising anisotropy along local [100] directions.

TABLE II. The crystal field parameters for $Er_3Ga_5O_{12}$ obtained from the point charge calculation and by fitting the INS data at $T = 4$ K.

$B_n^i(meV)$	$point_{cal}$	$Fitted$
B_2^0	0.0779	0.1271
B_2^2	-0.2781	-0.4371
B_4^0	2.1371e-5	6.6574e-4
B_4^2	-0.0034	-0.0017
B_4^4	-0.0029	0.0033
B_6^0	-3.0242e-6	1.0300e-5
B_6^2	-1.4031e-5	9.0100e-5
B_6^4	1.9502e-5	5.0300e-5
B_6^6	-2.1051e-5	-8.5100e-6

Specific heat and magnetic susceptibility

We next turn to the low-temperature collective magnetic properties of $Er_3Ga_5O_{12}$. We performed a specific heat measurement in zero field to look for signs of magnetic order, low-lying magnetic excitations, and residual entropy. In Fig. 4, we display our specific heat data for $Er_3Ga_5O_{12}$ in the low-temperature regime which is in agreement with previous work[54]. The upturn at the lowest temperatures likely arises from a ^{167}Er nuclear Schottky contribution. With increasing temperature, a second order phase transition is clearly seen around 0.75 K where a λ anomaly appears. We also plot the entropy recovery when warming through the ordering transition in Fig 4, which saturates at $Rln(2)$ by 4 K. This finding is consistent with the well-isolated CEF doublet ground state revealed by INS and indicates that there is essentially no residual entropy remaining in the ordered state.

As shown in Fig. 5, the magnetic susceptibility at high temperatures (150-300 K) is well described by a Curie-Weiss Law with a Weiss temperature θ_{CW} = -15 K and an effective Er moment of 9.57 μ_B; the latter corresponds well to the expected value of 9.59 μ_B for an isolated Er^{3+} ion. The Curie-Weiss fit to the magnetic susceptibility in the low temperature regime (2-5 K) results in a Weiss

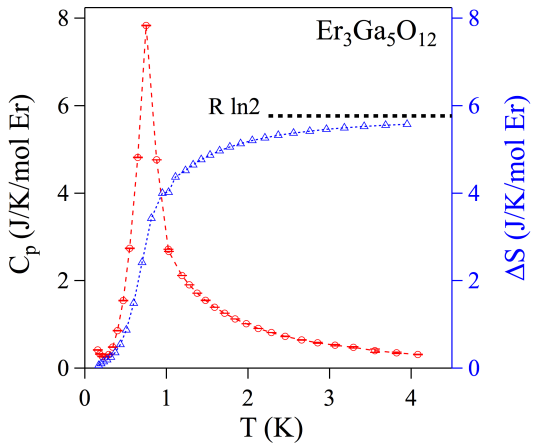

FIG. 4. Specific heat (red circles, left y-axis) vs temperature for $Er_3Ga_5O_{12}$ and the entropy recovered (blue triangles, right y-axis) when warming through the ordering transition. Dashed lines are a guide to the eye. The black line shows the expected saturation entropy of $Rln(2)$

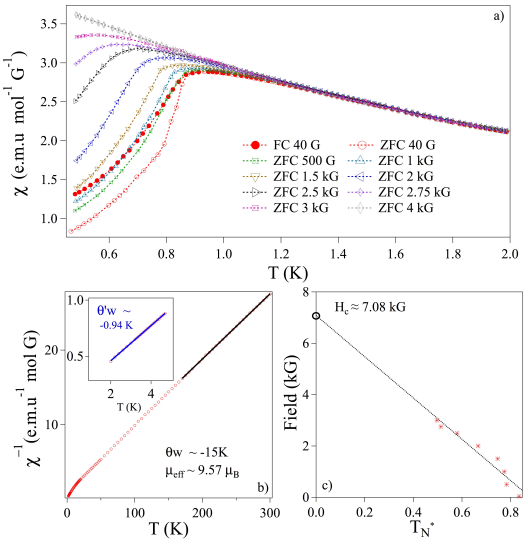

FIG. 5. (a) Temperature-dependent DC susceptibility below 2 K in selected [110] magnetic fields up to 4 kG. Zero-field-cooled/field-cooled irreversibility was found in the 40 G data only. (b) The inverse susceptibility data (red dots) obtained in a 100 G applied field at temperatures between 2 to 5 K and 150 to 300 K with the Curie-Weiss fits superimposed on the data as solid lines. (c) External field vs T_{N^*} determined by DC susceptibility measurements. A linear extrapolation of T_{N^*}, shown by the dashed line, yields a critical field of 7.08 kG at 0 K.

temperature θ'_{CW} = -0.94 K. Upon cooling, low-field (i.e. 40 G) susceptibility data shows a maximum around 0.8 K where the long-range ordering transition was first identified by zero-field specific heat. The close agreement between θ'_{CW} and the ordering temperature indicates that $Er_3Ga_5O_{12}$ is not a strongly-frustrated system. We also found zero-field-cooled/field-cooled irreversibility in the 40 G data only and a strongly field-dependent ordering transition that is suppressed below the temperature range we can measure by 4 kG. A linear extrapolation of the field-dependent ordering temperatures (T_{N^*}) gives $H_c(0\text{ K}) \sim 7.08$ kG, as shown in Fig. 5(c).

Neutron powder diffraction

Figure 6 shows $\lambda = 2.41$ Å NPD data for $Er_3Ga_5O_{12}$ at $T = 3$ K and 0.3 K. The crystal structure of the 3 K dataset refines well in the garnet room temperature space group $Ia\bar{3}d$ with lattice constant $a = 12.2652(1)$ Å, which indicates that cubic symmetry is preserved over a wide temperature range. The 0.3 K NPD data shows evidence for long-range magnetic order, as several new Bragg peaks emerge and some nuclear peaks gain additional intensity. On the other hand, no diffuse magnetic scattering is observed in this data. The five strongest magnetic Bragg peaks are marked by black arrows in Fig. 6(b) and can be indexed as (110), (211), (222), (321) and (330); the latter is indicative of a $\vec{k} = 0$ magnetic propagation vector. The representational analysis software SARAh[55] was used to establish candidate magnetic models allowed by symmetry. There are eight possible irreducible representations that describe the spin configurations of this six-sublattice magnet. For clarity, the fractional coordinates for one of the four Er^{3+} ions in the chemical unit cell making up each of the six sublattices are presented in Table III. Γ_3 and Γ_4 are the simplest magnetic models with only one basis vector each and they are appropriate for Ising garnets with equal moments on all Er^{3+} sites with strong Ising anisotropy along local [100] directions. Γ_5 and Γ_6 consist of two basis vectors each and they are also appropriate for Ising garnets with strong Ising anisotropy along local [100] directions, but the moment size on all magnetic sites is not equivalent. The other four models are much more complicated and consist of several basis vectors.

We tried to refine the NPD data using all eight possible models and including both the j_0 and j_2 spherical Bessel contributions to the Er^{3+} magnetic form factor. We found that the best fit comes from the Γ_3 magnetic structure, in good agreement with previous work[56]. The final result is superimposed as a dashed red curve on the 0.3 K data presented in Fig. 6(b). A schematic of the Γ_3 magnetic structure viewed along the a-axis is also illustrated in Fig. 6(c), while the local arrangement of the Er^{3+} ions on two corner-sharing triangles is shown

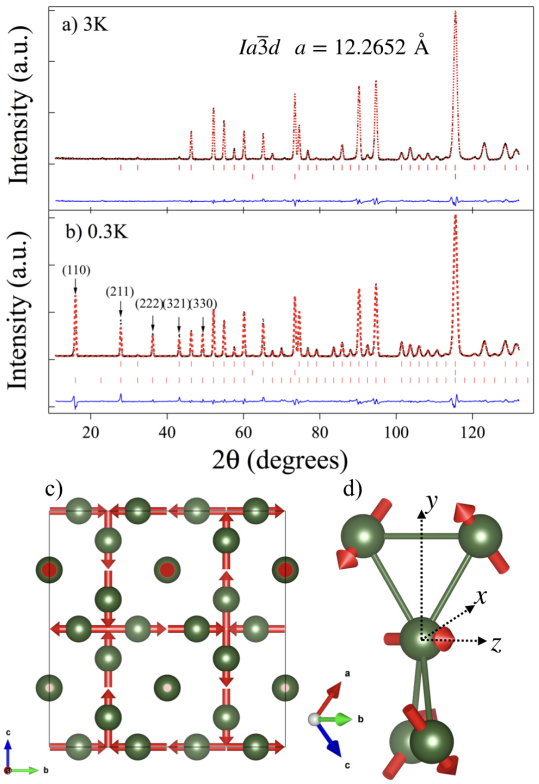

FIG. 6. Neutron powder diffraction data, indicated by the solid symbols and collected with a neutron wavelength 2.41 Å, at temperatures of (a) 3 K and (b) 0.3 K. The best structural refinement, including contributions from both the sample and the Al sample can, is superimposed on the 3 K data as a dashed red curve. The magnetic contribution is also included in the 0.3 K refinement. The expected Bragg peak positions for the crystal structure of $Er_3Ga_5O_{12}$, the crystal structure of the Al can, and the magnetic structure of $Er_3Ga_5O_{12}$ are indicated by ticks. (c) A schematic of the magnetic structure for $Er_3Ga_5O_{12}$ as viewed along the a-axis. (d) The spin configuration for the Er^{3+} ions on two corner-sharing triangles.

TABLE III. Fractional coordinates of the Er^{3+} ions corresponding to the six different magnetic sublattices in the $Ia\bar{3}d$ crystallographic unit cell.

Sublattice	Fractional Coordinates	Moment Direction
1	(0, 0.25, 0.125)	$-\hat{c}$
2	(0.125, 0, 0.25)	$-\hat{a}$
3	(0.25, 0.125, 0)	$-\hat{b}$
4	(0, 0.25, 0.625)	$\hat{c}$
5	(0.625, 0, 0.25)	$\hat{a}$
6	(0.25, 0.625, 0)	$\hat{b}$

in Fig. 6(d). All the moments in this magnetic structure point along local [100] directions, with the exact configuration specified in Table III, and the refined ordered moment is 5.24(4) μ_B. Both the moment direction and magnitude agree well with our crystal field analysis described above, as we find a slightly larger saturated moment along the local [100] Ising direction of 5.61 μ_B. It is also interesting to note that the Γ_3 state is the expected magnetic structure for an Ising garnet with moments constrained along the [100] directions and coupled through dipolar interactions only[40]. Furthermore, this is the same spin configuration found for other Ising garnets including $Dy_3Al_5O_{12}$[37], $Tb_3Al_5O_{12}$[38], $Ho_3Al_5O_{12}$[38], and $Ho_3Ga_5O_{12}$[39].

Muon spin relaxation

In μSR measurements, spin polarized muons are implanted into a sample one at a time where they thermalize rapidly in the material while maintaining their polarization. These thermalized muons find a minimum electrostatic potential site where they come to rest and their spins precess in the local magnetic field until they decay (with an average lifetime $\tau_\mu = 2.2\ \mu s$), emitting a positron preferentially in the direction of the muon spin at the time of decay. Detectors on either side of the sample register the decay of the positron and record the time interval between muon injection and decay.

We show ZF$-\mu$SR data for $Er_3Ga_5O_{12}$ between 30 mK and 300 K in Fig. 7. This temperature range ensures that the sample passes through the 0.8 K transition temperature inferred from the bulk characterization measurements. We note that the data exhibit no sign of oscillations down to 30 mK, which is unexpected in a magnetically-ordered state. In most cases, no spontaneous muon precession indicates an absence of coherent long-range magnetic order. One alternative scenario for the absence of oscillations is that the initial muon beam polarization and the local field are parallel, but this cannot be the case here due to the non-collinear nature of the magnetic structure as determined by NPD above. Another scenario is that the ordered moment size is too large to resolve in our ZF-μSR measurements, but we would then expect missing initial asymmetry and we find no evidence for that here.

We fit the ZF$-\mu$SR spectra at all temperatures to a stretched exponential function of the form: $P(t) = A_t e^{-(\lambda t)^\alpha}$, with a temperature-independent initial asymmetry A_t. The temperature-dependence of the relaxation rate λ and the power α are shown in Fig. 8. Surprisingly, there is no change in either of these parameters at $T_N = 0.8$ K and they appear to be temperature-independent below ~ 20 K. Similar low-temperature relaxation plateaus have been observed in a variety of frustrated magnets with ordered ground states[57–60], but

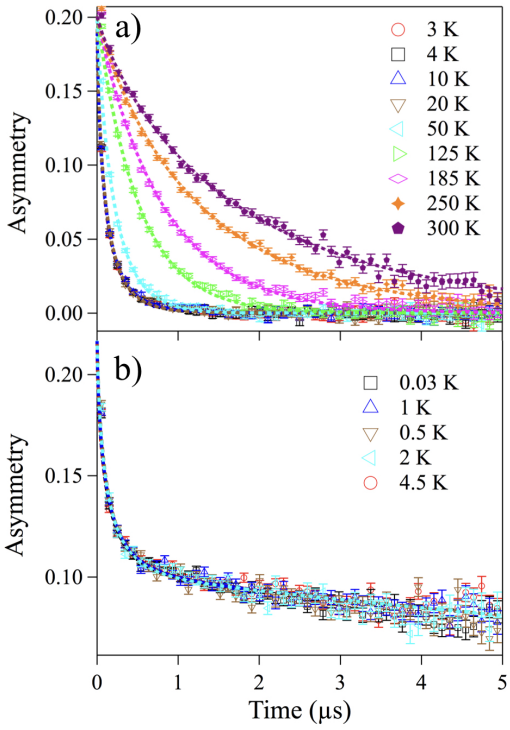

FIG. 7. Zero field μSR spectra of $Er_3Ga_5O_{12}$ measured over a temperature range of (a) 2 to 300 K and (b) 30 mK to 4.5 K. Colored symbols are the experimental data and the dashed lines are the fitting results as described in the text.

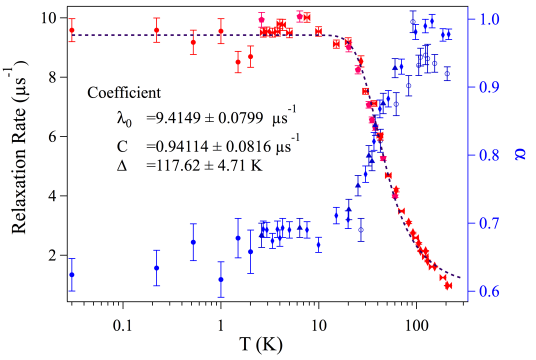

FIG. 8. Temperature dependence of the zero field μSR relaxation rate (red symbols) and power α (blue symbols) for $Er_3Ga_5O_{12}$. The dashed black curve represents the best fit result of the temperature-dependent relaxation rate using the fitting function described in the main text.

their microscopic origin is still unclear[61].

We note that ZF-μSR could be completely insensitive to the ordering transition in this material if the muon occupies a crystallographic site where the local field is zero by symmetry. However, an increase in the relaxation rate below T_N in the isostructural material $Yb_3Ga_5O_{12}$[41] indicates that this possibility is unlikely. To strengthen this conjecture, we calculated the expected field distribution on 1 Å spherical shells centered on the O^{2-} ions, corresponding to probable stopping sites for the muons[62], for the magnetic structure of $Er_3Ga_5O_{12}$ shown in Fig. 6(c). Assuming an ordered moment of 5.24 μ_B as determined by our NPD measurements above, we found that the internal fields range from 0.5 kG to 37.0 kG. We also calculated the local field distribution at these same locations assuming that the Er moments are frozen in a completely random spin configuration, which yields local fields varying from 1.3 kG to 40.3 kG. These calculated fields are all much bigger than the average local field ($\lambda_0/\gamma_\mu \sim 110$ G) we inter from our ZF-μSR spectra, which indicates that the insensitivity of this technique to the ordering transition is not simply due to an accidental cancellation of the local field at the muon stopping sites.

Above $\sim$ 20 K when the sample is in the paramagnetic state, the relaxation rate decreases with temperature up to 300 K. This behaviour is likely due to an Orbach process[63], which involves both phonon modes and a thermally-excited crystal field level with an energy Δ, and has been shown to play an important role in the μSR spectra of other rare-earth based magnets[41, 64]. In this case, the temperature-dependence of the relaxation rate can best be modeled by $\lambda^{-1} = \lambda_0^{-1} + C^{-1}e^{-\beta\Delta}$ where $\beta = 1/k_BT$. The fitted result for $Er_3Ga_5O_{12}$ is presented in Fig. 8 and provides a good description of the relaxation rate over a wide temperature range when $\lambda_0 = 9.41(8)\ \mu s^{-1}$, $C = 0.94(8)\ \mu s^{-1}$, and $\Delta = 10.1(4)$ meV. The value for Δ is in reasonable agreement with the second excited CEF level at 9.79 meV measured with INS. A two phonon process has been used to show why the second excited CEF level is participated[65, 66].

CONCLUSION

We have carried out a series of comprehensive measurements investigating the single ion and collective magnetic properties of the garnet $Er_3Ga_5O_{12}$. Our inelastic neutron scattering measurements reveal a CEF Hamiltonian for Er^{3+} that is consistent with a large Ising anisotropy along local [100] directions. Our bulk characterization measurements, including specific heat and magnetic susceptibility, show evidence for the onset of long-range antiferromagnetic order at 0.8 K. Neutron powder diffraction

reveals that this order corresponds to a six-sublattice, Ising antiferromagnetic spin configuration. This magnetic state is consistent with predictions for [100] Ising moments coupled through dipolar interactions[40] and ensures that $Er_3Ga_5O_{12}$ is an excellent model system for investigating the complex metamagnetic behavior expected for a multi-axis magnet.

ACKNOWLEDGMENTS

We acknowledge useful discussions with Connor Buhariwalla, Alannah Hallas and Jonathan Gaudet. We also appreciate the support of TRIUMF personnel during the μSR measurements. Work at McMaster was supported by the Natural Sciences and Engineering Research of Council of Canada. A portion of this research used resources at the Spallation Neutron Source and High Flux Isotope Reactor, which are DOE Office of Science User Facilities operated by Oak Ridge National Laboratory.

* aczelaa@ornl.gov
† luke@mcmaster.ca

[1] J.E. Greedan, Journal of Alloys and Compouonds **408-412**, 444 (2006).
[2] J.S. Gardner, M.J.P. Gingras, and J.E. Greedan, Rev. Mod. Phys. **82**, 53 (2010).
[3] C.R. Wiebe and A.M. Hallas, APL Materials **3**, 041519 (2015).
[4] J.N. Reimers, J.E. Greedan, R.K. Kremer, E. Gmelin, and M.A. Subramanian, Phys. Rev. B **43**, 3387 (1991).
[5] H.J. Silverstein, K. Fritsch, F. Flicker, A.M. Hallas, J.S. Gardner, Y. Qiu, G. Ehlers, A.T. Savici, Z. Yamani, K.A. Ross, B.D. Gaulin, M.J.P. Gingras, J.A.M. Paddison, K. Foyevtsova, R. Valenti, F. Hawthorne, C.R. Wiebe, and H.D. Zhou, Phys. Rev. B **89**, 054433 (2014).
[6] J.-J. Wen, S.M. Koohpayeh, K.A. Ross, B.A. Trump, T.M. McQueen, K. Kimura, S. Nakatsuji, Y. Qiu, D.M. Pajerowski, J.R.D. Copley, and C.L. Broholm, Phys. Rev. Lett. **118**, 107206 (2017).
[7] B. Gao, T. Chen, D.W. Tam, C.-L. Huang, K. Sasmal, D.T. Adroja, F. Ye, H. Cao, G. Sala, M.B. Stone, C. Baines, J.A.T. Barker, H. Hu, J.-H. Chung, X. Xu, S.-W. Cheong, M. Nallaiyan, S. Spanga, M.B. Maple, A.H. Nevidomskyy, E. Morosan, G. Chen, and P. Dai, arXiv: 1901.10092
[8] J. Gaudet, E.M. Smith, J. Dudemaine, J. Beare, C.R.C. Buhariwalla, N.P. Butch, M.B. Stone, A.I. Kolesnikov, G. Xu, D.R. Yahne, K.A. Ross, C.A. Marjerrison, J.D. Garrett, G.M. Luke, A.D. Bianchi, and B.D. Gaulin, arXiv: 1903.09207
[9] J. Snyder, J.S. Slusky, R.J. Cava, and P. Schiffer, Nature **413**, 48 (2001).
[10] J.D.M. Champion, M.J. Harris, P.C.W. Holdsworth, A.S. Wills, G. Balakrishnan, S.T. Bramwell, E. Cizmar, T. Fennell, J.S. Gardner, J. Lago, D.F. McMorrow, M. Orendac, A. Orendacova, D. McKPaul, R.I. Smith, M.T.F. Telling, and A. Wildes, Phys. Rev. B **68**, 020401(R) (2003).
[11] K.A. Ross, Y. Qiu, J.R.D. Copley, H.A. Dabkowska, and B.D. Gaulin, Phys. Rev. Lett. **112**, 057201 (2014).
[12] O. Benton, Phys. Rev. B **94**, 104430 (2016).
[13] S. Petit, E. Lhotel, B. Canals, M. Ciomaga Hatnean, J. Ollivier, H. Mutka, E. Ressouche, A.R. Wildes, M.R. Lees, and G. Balakrishnan, Nature Physics **12**, 746 (2016).
[14] W. I. Kinney and W. P. Wolf, J. Appl. Phys., **50**, 2115 (1979).
[15] O.A. Petrenko, C. Ritter, M. Yethiraj, and D. McKPaul, Phys. Rev. Lett. **80**, 4570 (1998).
[16] S.R. Dunsiger, J.S. Gardner, J.A. Chakhalian, A.L. Cornelius, M. Jaime, R.F. Kiefl, R. Movshovich, W.A. MacFarlane, R.I. Miller, J.E. Sonier, and B.D. Gaulin, Phys. Rev. Lett. **85**, 3504 (2000).
[17] I.M. Marshall, S.J. Blundell, F.L. Pratt, A. Husmann, C.A. Steer, A.I. Coldea, W. Hayes, and R.C.C. Ward, J. Phys.: Condens. Matter **14**, L157 (2002).
[18] T. Yavors'kii, M. Enjalran, and M.J.P. Gingras, Phys. Rev. Lett. **97**, 267203 (2006).
[19] P.P. Deen, O.A. Petrenko, G. Balakrishnan, B.D. Rainford, C. Ritter, L. Capogna, H. Mutka, and T. Fennell, Phys. Rev. B **82**, 174408 (2010).
[20] J.A. Quilliam, S. Meng, H.A. Craig, L.R. Corruccini, G. Balakrishnan, O.A. Petrenko, A. Gomez, S.W. Kycia, M.J.P. Gingras, and J.B. Kycia, Phys. Rev. B **87**, 174421 (2013).
[21] N. d'Ambrumenil, O.A. Petrenko, H. Mutka, and P.P. Deen, Phys. Rev. Lett. **114**, 227203 (2015).
[22] P.P. Deen, O. Florea, E. Lhotel, and H. Jacobsen, Phys. Rev. B **91**, 014419 (2015).
[23] J.A.M. Paddison, H. Jacobsen, O.A. Petrenko, M.T. Fernandez-Diaz, P.P. Deen, and A.L. Goodwin, Science **350**, 179 (2015).
[24] T. Yoshioka, A. Koga, and N. Kawakami, J. Phys. Soc. Jpn. **73**, 1805 (2004).
[25] B.E. Keen, D.P. Landau, and W.P. Wolf, Physics Letters **23**, 202 (1966).
[26] B.E. Keen, D. Landau, B. Schneider, and W.P. Wolf, Journal of Applied Physics **37**, 1120 (1966).
[27] J. Felsteiner and S.K. Misra, Phys. Rev. B **24**, 2627 (1981).
[28] M. Steiner and N. Giordano, Phys. Rev. B **25**, 6886 (1982).
[29] E.Y. Wong, O.M. Stafsudd, and D.R. Johnston, The Journal of Chemical Physics **39**, 786 (1983).
[30] B. Dreyfus, J. Verdone, and M. Veyssie, J. Phys. Chem. Solids **26**, 107 (1965).
[31] F.N. Hooge, The Journal of Chemical Physics **45**, 4504 (1966).
[32] J.A. Koningstein, The Journal of Chemical Physics **44**, 3957 (1966).
[33] R.A. Buchanan, K.A. Wickersheim, J.J. Pearson, and G.F. Herrmann, Phys. Rev. **159**, 245 (1967).
[34] L.F. Johnson, J.F. Dillon Jr., and J.P. Remeika, Phys. Rev. B **1**, 1935 (1970).
[35] B.L. Reid, D.F. McMorrow, P.W. Mitchell, O. Prakash, and A.P. Murani, Physica B **174**, 51 (1991).
[36] O.V. Kovalev, *Representations of the Crystallographic Space Groups Edition 2*, (Gordon and Breach Publishers, Yverdon, Switzerland, 1993).

[37] J.M. Hastings, L.M. Corliss, and C.G. Windsor, Phys. Rev. **138**, A176 (1965).
[38] J. Hammann, Acta. Cryst. B **25**, 1853 (1969).
[39] J. Hammann and M. Ocio, Le Journal de Physique **38**, 463 (1977).
[40] H.W. Capel, Physica **31**, 1152 (1965).
[41] P. Dalmas de Reotier, A. Yaouanc, P.C.M. Gubbens, C.T. Kaiser, C. Baines, and P.J.C. King, Phys. Rev. Lett. **91**, 167201 (2003).
[42] J.A. Hodges, P. Bonville, M. Rams, and K. Krolas, J. Phys.: Condens. Matter **15**, 4631 (2003).
[43] J. Hammann, Physics Letters **26A**, 263 (1968).
[44] H. D. Zhou, C. R. Wiebe, L. Balicas, Y. J. Yo, Y. Qiu, J. R. D. Copley, and J. S. Gardner, Phys. Rev. B **78**, 140406(R) (2008).
[45] G.E. Granroth, A.I. Kolesnikov, T.E. Sherline, J.P. Clancy, K.A. Ross, J.P.C. Ruff, B.D. Gaulin, and S.E. Nagler, J. Physics: Conference Series **251**, 012058 (2010).
[46] S. Calder, K. An, R. Boehler, C.R. dela Cruz, M.D. Frontzek, M. Guthrie, B. Haberl, A. Huq, S.A.J. Kimber, J. Liu, J.J. Molaison, J. Neuefeind, K. Page, A.M. dos Santos, K.M. Taddei, C. Tulk, and M.G. Tucker, Rev. Sci. Inst. **89**, 092701 (2018).
[47] J. Rodriguez-Carvajal, Physica B **192**, 55 (1993).
[48] A. Suter, B. M. Wojek, Physics Procedia **30**, 69 (2012).
[49] M. T. Hutchings *Solid State Physics*, (Academic Press, New York, USA, 1964).
[50] G. Squires, *Introduction to the Theory of Thermal Neutron Scattering*, (Cambridge University Press, Cambridge, UK, 1978).
[51] J. Gaudet, D.D. Maharaj, G. Sala, E. Kermarrec, K.A. Ross, H.A. Dabkowska, A.I. Kolesnikov, G.E. Granroth, and B.D. Gaulin, Phys. Rev. B **92**, 134420 (2015).
[52] Cooke et al, *Proc. Phys. Soc.* **92**, 400 (1967).
[53] Redoules et al, *Le Journal de Physique* **33**, 281 (1972).
[54] D.G. Onn, H. Meyer, and J.P. Remeika, Phys. Rev. **156**, 663 (1967).
[55] A.S. Wills, Physica B **276**, 680 (2000).
[56] J. Hammann, Le Journal de Physique **29**, 495 (1968).
[57] J. Lago, T. Lancaster, S.J. Blundell, S.T. Bramwell, F.L. Pratt, M. Shirai, and C. Baines, J. Phys.: Condens. Matter **17**, 979 (2005).
[58] P. Dalmas de Reotier, A. Yaouanc, L. Keller, A. Cervellino, B. Roessli, C. Baines, A. Forget, C. Vaju, P.C.M. Gubbens, A. Amato, and P.J.C. King, Phys. Rev. Lett. **96**, 127202 (2006).
[59] S.R. Dunsiger, R.F. Kiefl, J.A. Chakhalian, J.E. Greedan, W.A. MacFarlane, R.I. Miller, G.D. Morris, A.N. Price, N.P. Raju, and J.E. Sonier, Phys. Rev. B **73**, 172418 (2006).
[60] G.M. Kalvius, A. Krimmel, O. Hartmann, F.J. Litterst, R. Wappling, F.E. Wagner, V. Tsurkan, and A. Loidl, Eur. Phys. J. B **77**, 87 (2010).
[61] P.A. McClarty, J.N. Cosman, A.G. Del Maestro, and M.J.P. Gingras, J. Phys.: Condens. Matter **23**, 164216 (2011).
[62] E. Holzschuh, A. B. Denison, W. Kundig, P. F. Meier, and B. D. Patterson, *Phys. Rev. B* **27**, 5294 (1983).
[63] R. Orbach, Proc. Phys. Soc. A **264**, 458 (1961).
[64] R. Khasanov, H. Luetkens, A. Amato, H.-H. Klauss, Z.A. Ren, J. Yang, W. Lu, and Z.-X. Zhao, Phys. Rev. B **78**, 092506 (2008).
[65] J. Xu, C. Balz, C. Baines, H. Luetkens, and B. Lake, *Phys. Rev. B* **94**, 064425 (2016)
[66] A. Yaouanc and P. Dalmas de Reotier, *Muon Spin Rotation, Relaxation, and Resonance: Applications to Condensed Matter* (Oxford University Press, 2011).

5

$ErMgGaO_4$

5.1 Summary of $ErMgGaO_4$

The quasi-two dimensional $YbFe_2O_4$-type structured compound $YbMgGaO_4$ has been attracting lots interest as a potential quantum spin liquid candidate, in which anisotropic exchange interactions between rare earth ions play a crucial role in stabilizing a spin liquid ground state in this triangular antiferromagnet [17–19, 21, 22, 50]. Such exchange interactions associated with spin orbit coupling strongly depends on different rare earth ions. In this work, we sought to study a related material $ErMgGaO_4$, where Er^{3+} is expected to show different exchange interaction strength compared to Yb^{3+}.

We grew our $ErMgGaO_4$ samples by Floating Zone Optical Image Furnaces at McMaster University as described in Section. 2.1. $ErMgGaO_4$, similar to $YbMgGaO_4$, has a space group as $R\bar{3}m$, with quasi-two dimensional Er^{3+} stacked triangular lattice. The magnetic susceptibility at high temperature (150-300 K) was well described by a Curie Weiss Law with the resulting Weiss temperature θ_{CW} = -33 K and an effective Er moment of 10.3 μ_B; the latter corresponds fairly well to the expected value of 9.59 μ_B for an isolated Er^{3+} ion. The Curie-Weiss fit to the magnetic susceptibility in the low temperature regime (2-5 K) results in a Weiss temperature θ'_{CW} = -3.9 K. Further measurements below 2 K indicates the presence of magnetic anisotropy and no evidence of any magnetic transitions down to 0.5 K, indicating substantial frustration in this system.

We performed a point charge calculation of the crystal electric field in studying the spin anisotropy. This calculation yielded a well separated Kramers doublet ground state, which is comprised primarily of $m_J = \pm 15/2$ and the corresponding anisotropic g-tensor components are

given by $g_{\parallel} = 2g_J|\langle\phi_0^{\pm}|J_z|\phi_0^{\pm}\rangle| = 17.91$ and $g_{\perp} = g_J|\langle\phi_0^{\pm}|J_{\pm}|\phi_0^{\mp}\rangle| = 0$. This implies an Ising-like behaviour of the Er^{3+} in $ErMgGaO_4$.

Furthermore, we perform specific heat measurement and μSR measurements to characterize the low energy magnetic modes, and spin dynamics.

The specific heat measurements exhibit a broad hump with the maximum at around 1.5 K. We computed the entropy change $\Delta S(T)$: we find that the entropy saturates at $Rln(2)$ around 4 K, which is the expected value for an Ising-like, isolated doublet state as expected on the basis of our CEF anisotropy calculation. This agreement indicates that any residual entropy for temperatures approaching zero is extremely small or zero, which means there won't be any magnetic transitions down to zero temperature and indicates, similar to $YbMgGaO_4$, $ErMgGaO_4$ is another quantum spin liquid candidate.

We carried out μSR measurement in wide temperature range between 25 mK to 300 K. In ZF$-\mu$SR measurement, the data exhibit no sign of oscillations down to 25 mK, indicating there is no transition to long-range magnetic order. The ZF asymmetry appears to relax to the zero baseline without a recovery of 1/3 tail which rules out the possibility of a spin glass state. In LF$-\mu$SR measurements, the relaxation rate at 25 mK is barely decoupled as the applied field increasing up to 1 T. This means the spins associated with the Er^{3+} ions remain in a dynamically fluctuating state down to our lowest temperature 25 mK, which is also evidence for a quantum liquid state.

Our observation provide evidences of a quantum spin liquid state in this Ising-like triangular antiferromagnet $ErMgGaO_4$.

Preprint II: "*μSR study of triangular Ising antiferromagnet $ErMgGaO_4$*", Y. Cai, C. Lygouras, G. Thomas, M. N. Wilson, J. Beare, D.R. Yahne, K. Ross, Z. Gong, Y. J. Uemura, H.A. Dabkowska, and G.M. Luke. *arXiv*:1905.12798 (2019).

Author Contributions:

- *Experimental Concept*: **Y. Cai**, G.M. Luke
- *Sample Preparation*: **Y. Cai**, C. Lygouras, G. Thomas, H.A. Dabkowska, G.M. Luke
- *μSR Experiments*: **Y. Cai**, M.N. Wilson, J. Beare, Z. Gong, Y. J. Uemura, G.M. Luke
- *Specfic heat Experiments*: D.R. Yahne, K. Ross
- *Data Analysis*: **Y. Cai**, G.M. Luke
- *Manuscript*: **Y. Cai**, G.M. Luke

μSR study of triangular Ising antiferromagnet $ErMgGaO_4$

Y. Cai,[1] C. Lygouras,[1] G. Thomas,[1] M. N. Wilson,[1] J. Beare,[1] D.R. Yahne,[2]
K. Ross,[3,4] Z. Gong,[5] Y. J. Uemura,[5] H.A. Dabkowska,[6] and G.M. Luke[1,4,7]

[1]*Department of Physics and Astronomy, McMaster University, Hamilton, Ontario L8S 4M1, Canada*
[2]*Department of Physics, Colorado State University, Fort Collins, CO 80523, USA*
[3]*Department of Physics, Colorado State University, Fort Collins, Colorado 80523, USA*
[4]*Canadian Institute for Advanced Research, Toronto, Ontario M5G 1M1, Canada*
[5]*Department of Physics, Columbia University, New York, New York 10027, USA*
[6]*Brockhouse Institute for Materials Research, McMaster University, Hamilton, Ontario, Canada L8S 4M1*
[7]*TRIUMF, Vancouver, British Columbia. V6T 2A3, Canada*

We present a detailed magnetic study of the triangular antiferromagnet $ErMgGaO_4$. A point charge calculation under the single ion approximation reveals a crystal field ground state doublet with a strong Ising-like behavior of the Er^{3+} moment along the c axis. Magnetic susceptibility and specific heat measurements indicate no presence of magnetic transitions above 0.5 K and no evidence of residual entropy as temperature approaching zero. Zero field (ZF) μSR measurements shows no sign of static uniform or random field and longitudinal field (LF) μSR measurements exhibit persistent spin fluctuations down to our lowest temperature of 25 mK. Our results provide evidence of a quantum spin liquid state in the triangular antiferromagnet $ErMgGaO_4$.

A quantum spin liquid (QSL) is a state of matter in which spins are highly entangled and do not show magnetic order down to zero temperature [1]. QSL's are of great current interest both from a fundamental physics point of view and for possible applications in quantum computation [2]. Geometrically frustrated magnets (where competing magnetic interactions cannot be simultaneously satisfied) are excellent candidate materials for QSL behavior since magnetic order is suppressed in them by the frustration [3–5]. Such frustration frequently arises from antiferromagnetically coupled spins located on triangle-based lattices (stacked triangular, kagome, pyrochlore), and can lead to a highly degenerate ground state without magnetic order. The previously studied quasi-two dimensional triangular layered material $YbMgGaO_4$ (with $YbFe_2O_4$-type structure) has been attracting considerable interest as a potential quantum spin liquid candidate [6–12].

$YbMgGaO_4$ has a Curie-Weiss temperature of $\sim$ -4 K but shows no sign of long-range order down to 30 mK [6, 7, 9, 10]. Its magnetic specific heat in zero field shows a broad hump at 2.4 K instead of sharp λ-type peak which would be expected for a well-defined second order phase transition. The magnetic excitation spectra appears as a broad continuum in inelastic neutron scattering measurements, which has been taken as an evidence for a QSL state [7, 10]. Particularly, the anisotropic exchange interactions between rare earth ions are found to be playing a crucial role in stabilizing such spin liquid ground state [6–10], although an alternative explanantion in terms of the random Ga/Mg site mixing has also been proposed [11]. Such exchange interactions associated with spin orbit coupling strongly depends on rare earth ions. It has also been found, particularly, in rare earth pyrochlores ($R_2B_2O_7$ with R = rare earth, B = non-magnetic cation), that the interplay of exchange couplings, dipolar interactions, and single ion anisotropy leads to spin glasses [5, 13], spin liquids [14–16], spin ices [17], order-by-disorder [18, 19], magnetic moment fragmentation [20, 21], and conventional long-range magnetic ordering [22]. These observations indicating different rare earth ions can result in much different ground states, motivating the search for $RMgGaO_4$ with different magnetic rare earth elements.

In this paper, we report our study of the stacked triangular compound $ErMgGaO_4$. We have successfully synthesized single crystals of $ErMgGaO_4$ using the floating zone technique. On the basis of point charge calculations, we find a crystal field ground state doublet for Er^{3+} with strong Ising anisotropy along local [001] axes. We have investigated the collective magnetic properties of this system with magnetic susceptibility, heat capacity and muon spin rotation and relaxation. We find no magnetic transition down to our lowest temperature of 25 mK using ZF-μSR and no residual entropy which suggests there will not be any further magnetic transitions down to zero temperature. LF-μSR measurements indicate the presence of persistent spin fluctuations down to our lowest temperature 25 mK, a feature in common with some other high frustrated magnetic systems including $SrCr_{9p}Ga_{12-9p}O_{19}$ [23] and $Tb_2Ti_2O_7$ [24]. Collectively, our observations indicates that $ErMgGaO_4$ is an Ising-like quantum spin liquid candidate.

Crystals of $ErMgGaO_4$ were prepared in an optical floating zone image furnace at McMaster University [25]. Stoichiometric mixture powders of pre-annealed Er_2O_3, Ga_2O_3 and MgO were pre-reacted at 1200°C in air for 12 hours. The powder was later made into rods (6 cm in length and 8 mm in diameter) through hydrostatic pressure at 60 MPa for 15 minutes and these rods were then sintered at 1450°C in oxygen for 56 hours with an intermediate grinding and reformation. Both pre-reacted

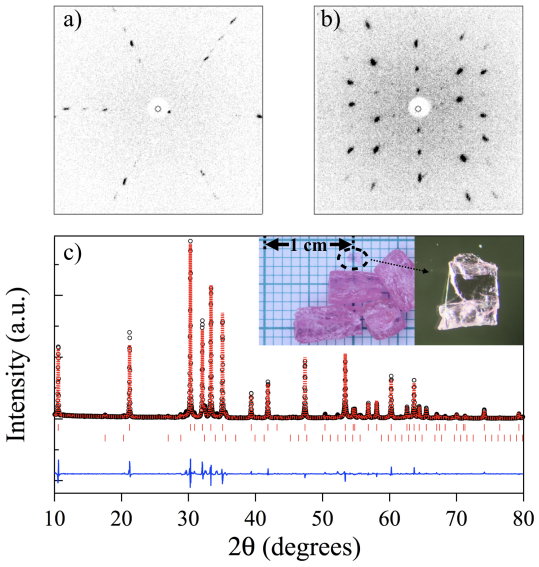

FIG. 1. Structural chracterization of $ErMgGaO_4$ by Laue diffraction and powder X-ray diffraction: a) & b) the Laue pattern in orientation of (001) and (100), c) Rietveld refinement of powder X-ray diffraction data. (Insert shows a picture of crystals and an extracted transparent small crystal)

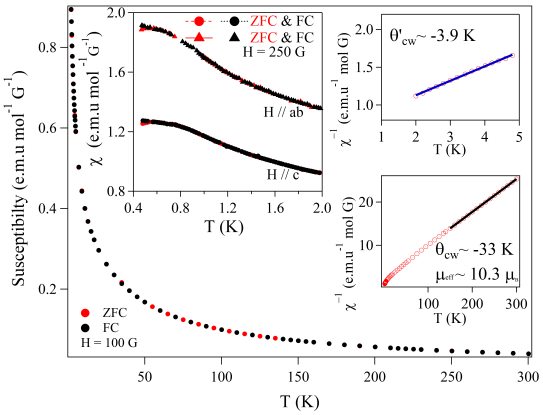

FIG. 2. Main panel: temperature dependent DC susceptibility from 2 K to 300 K at 100 G. Left insert: temperature dependent DC susceptibility below 2 K with applied external field along selected orientation. Right insert: the inverse susceptibility data (red dot) at temperatures between 2 to 5 K and 150 to 300 K with the Cure-Weiss fit superimposed on the data as solid lines.

powder and sintered rods were examined by powder X-ray diffraction. No pure phase of $ErMgGaO_4$ was found in either diffraction pattern and both contained magnetic $Er_3Ga_5O_{12}$ and non-magnetic MgO, indicating the desired phase was not formed during the sintering process. Crystal growth was carried out in a two-mirror optical floating zone image furnace (NEC systems). The optimal growing conditions were found from multiple attempts to have oxygen gas at 2 atmosphere overpressure and at a growth rate of 0.5 mm/hr. No clear large single crystal was found even after 8 cm growth, instead, transparent, relatively large multi-grain crystals (approximately 1cm in length) were obtained. Those grains were found to be misaligned in the ab-plane, but aligned with their c axis (which was usually perpendicular to the growth direction); this pattern of crystal formation of the crystal likely reflects the huge lattice parameter difference $c \gg a$. These multi-grain crystals are shown in Fig. 1: we also extracted single crystals from them. In Fig. 1, we present the characterization of a separated small crystal utilizing Laue X-ray diffraction. We also ground up a small crystal for powder X-ray diffraction. Structural Rietveld refinements were carried out using Fullprof software package. As shown in Fig. 1c, refinements to our X-ray diffraction data yield a good fit within two phases: $ErMgGaO_4$ ($R\bar{3}m$) and $Er_3Ga_5O_{12}$ ($Ia\bar{3}d$) with $\chi^2 = 3.96$ and weight fractions as 95.11% and 4.89%, respectively. Our Laue diffraction measurements confirm the $R\bar{3}m$ structure as seen in Fig. 1 a&b with the crystal oriented in the a-c plane.

We performed magnetic susceptibility measurements on a small crystal from 0.48 K to 300 K with a Quantum Design MPMS XL-3 equipped with an iQuantum He^3 Insert for measurements below 2 K. We also measured the specific heat between 0.1 K and 4 K using a Quantum Design PPMS with a dilution refrigerator insert.

As shown in Fig. 2, the magnetic susceptibility at high temperature (150-300 K) was well described by a Curie Weiss Law with the resulting Weiss temperature θ_{CW} = -33 K and an effective Er moment of 10.3(1) μ_B; the latter corresponds fairly well to the expected value of 9.59 μ_B for an isolated Er^{3+} ion. The Curie-Weiss fit to the magnetic susceptibility in the low temperature regime (2-5 K) results in a Weiss temperature θ'_{CW} = -3.9 K. Further measurements below 2 K indicates the presence of magnetic anisotropy and no evidence of any magnetic transitions down to 0.5 K in this compound. The high temperature results as well as magnetic anisotropy properties (above 2 K) are consistent with previous measurements [12]. Furthermore, there is no splitting of the zero-field-cooled and field-cooled susceptibilities other than a very small signature from $Er_3Ga_5O_{12}$ [26], which rules out the presence of a glassy spin freezing transition. The dominant antiferromagnetic exchange interaction in $ErMgGaO_4$ with no sign of magnetic transitions reveals that magnetic frustration is significant, which is similar to $YbMgGaO_4$ [6] and $TmMgGaO_4$ [27].

One important feature of the ground state properties of $ErMgGaO_4$ is its crystal electric field (CEF) induced magnetic spin anisotropy, where Er^{3+} has trigonal local symmetry with the point group D_{3d}. Spin anisotropy studies in $YbMgGaO_4$ have shown that a point charge calculation under a single ion approximation well captures its major properties, which were later found to be in agreement with their inelastic neutron scattering measurements [8]. We performed a similar point charge calculation under the single ion approximation to examine the ground state magnetism of $ErMgGaO_4$. According to Hund's rules, the total angular momentum of the Er^{3+} ion is $J = 15/2$ and the $(2J+1)$-fold degeneracy is lifted by CEFs due largely to the presence of the neighbouring O^{2-}ions into 8 Kramers doublets. Neglecting the potential effect of crystallographic distortion from the Ga/Mg site mixing, the CEF Hamiltonian is written as

$$\hat{\mathcal{H}}^{CEF}_{D_{3d}} = B^0_2\hat{O}^0_2 + \sum_{i=0,3} B^i_4\hat{O}^i_4 + \sum_{i=0,3,6} B^i_6\hat{O}^i_6, \qquad (1)$$

where the B^i_n are rare-earth dependent coefficients and $\hat{O}^i_n$ are Stevens operators which are combinations of total angular momentum operators [28].

In Table. I, we present our results obtained from this point charge calculation. This calculation yielded a well separated ground state and the ground state doublet is comprised primarily of $m_J = \pm 15/2$. The corresponding anisotropic g-tensor components are given by $g_\parallel = 2g_J|\langle\phi^\pm_0|J_z|\phi^\pm_0\rangle| = 17.91$ and $g_\perp = g_J|\langle\phi^\pm_0|J_\pm|\phi^\mp_0\rangle| = 0$, where z corresponds to the local c axis which implies a strong, effectively, Ising-like behaviour of the Er^{3+} moment along the c axis. We caution that the point charge calculation ignores the effect beyond nearest six oxygen neighbours and does not account the effects of the distorted electrostatic potential due to the Ga/Mg site mixing. This distortion in $YbMgGaO_4$ was found to only slightly broaden the CEF excitations and present a distribution of g-tensors but without dramatically changing its magnetic properties [8]. Our finding of Ising-like moments is quite different from $YbMgGaO_4$, where a Heisenberg-like spin anisotropy was established [7, 8].

We next turn to the low-temperature collective magnetic properties of $ErMgGaO_4$. We performed a specific heat measurement in zero field to look for signs of magnetic order, low-lying magnetic excitations, and residual entropy. In Fig. 3, we display our specific heat data for $ErMgGaO_4$ in the low-temperature regime. The upturn at the lowest temperatures likely arises from a ^{167}Er nuclear Schottky contribution. With increasing temperature, only a broad hump is seen with its maximum at around 1.5 K. No clearly λ anomaly was observed which would be expected for any magnetic order. We also plot the entropy recovery when warming through the hump in Fig 3, which saturates near $Rln(2)$ by 4 K. This finding is consistent with the well-isolated CEF doublet ground

TABLE I. The CEF parameters and eigenvalues for $ErMgGaO_4$ from point charge calculation. The ground state eigenvector are given in terms of the m_J basis with $J = 15/2$ for Er.

$B^0_2(meV)$	B^0_4	B^3_4	B^0_6	B^3_6	B^6_6
-0.3440	-5.3176e-4	-0.0122	2.4242e-6	1.3236e-5	7.043e-20

$Calcu$(meV)	0	19.06	36.99	48.63	52.91	61.71	62.69	64.37

$$\phi^\pm_0 = \mp 0.9937 \mid \mp\frac{15}{2}\rangle + 0.1111 \mid \mp\frac{9}{2}\rangle \mp 0.0128 \mid \mp\frac{3}{2}\rangle;$$

$$[g_\parallel, g_\perp] = [17.91, 0]$$

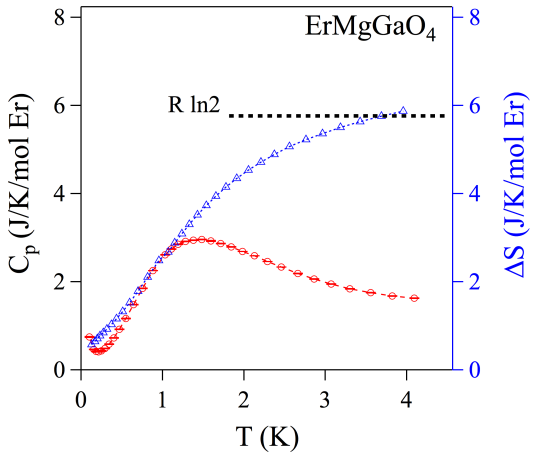

FIG. 3. Red circle points shows the specific heat versus temperature for $ErMgGaO_4$. The blue triangular shows the temperature dependent integral of C_p/T.

state as we expect on the basis of our previous CEF anisotropy calculation and indicates that there is essentially no residual entropy remaining as temperature approaching zero. This result also implies there will not be any further magnetic transitions down to zero temperature and that similar to $YbMgGaO_4$, $ErMgGaO_4$ is a quantum spin liquid candidate.

To directly rule out any possible magnetic ordering, we turned to muon spin rotation and relaxation (μSR), the most sensitive technique in detecting such weak ordering. In addition, μSR is also capable to characterize the low energy spin dynamics, which is also crucial in examining a quantum spin liquid state. We performed μSR measurements on the M15 and M20 beam-lines at the TRIUMF laboratory in Vancouver, Canada. Crystals of $ErMgGaO_4$ (aligned within 5 degrees along c-axis) were mounted on the M20 beam-line in a low background apparatus utilizing a He^4 cryostat, and later mounted onto an Ag plate and covered in thin Ag foil for the measure-

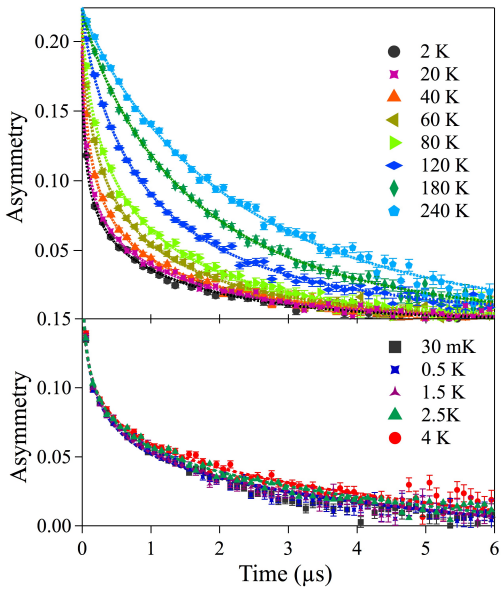

FIG. 4. Zero field μSR spectra of $ErMgGaO_4$ measured at temperature range 25 mK to 300 K. Coloured dots are experiment data, and corresponding dashed lines are the fitting results as described in text

ments in a dilution refrigerator on the M15 beamline. We performed measurements in both zero applied field (ZF) and with a magnetic field applied along the incident muon spin direction (LF). All the μSR data were fit by the open source μSRfit software package [29].

In Fig. 4, we show ZF$-\mu$SR data for $ErMgGaO_4$ between 25 mK and 300 K. The relaxation rate keeps increasing as the temperature deceases and the data exhibit no sign of oscillations down to 25 mK. The absence of spontaneous muon precession indicates there is no transition to long-range magnetic order in $ErMgGaO_4$, which is consistent with the magnetic susceptibility and specific heat results discussed above. The ZF$-\mu$SR asymmetry spectra relax to the same zero baseline without a recovery of 1/3 tail which rules out the possibility of a spin glass state, which would have 1/3 of muon polarization parallel to the random local field [30]. At all temperature, the ZF$-\mu$SR spectra were well fit to a stretched exponential:

$$P(t) = A_{total} e^{-(\lambda t)^{\beta}}$$

where the asymmetry A_{total} was independent of temperature.

The temperature dependence of the relaxation rate λ as well as the exponent β are shown in Fig. 5. Above $\sim$ 2 K, a sharply decreasing relaxation rate was observed with temperature increasing up to 300K. This behaviour

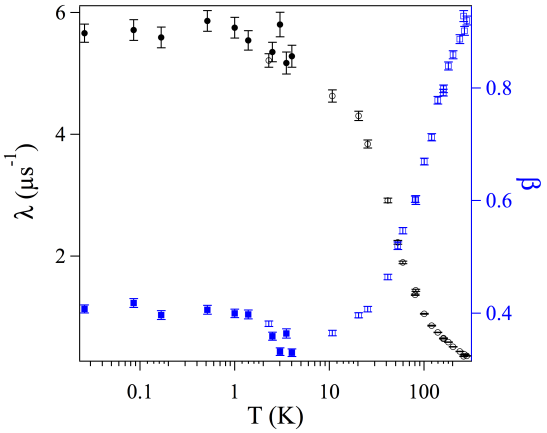

FIG. 5. Temperature dependence of zero field μSR relaxation rate in $ErMgGaO_4$. Open symbols are measurements obtained from He^4 cryostat ($>$ 2 K), and closed symbols are measurements obtained from dilution refrigerator ($<$ 5 K)

is likely due to the Orbach process [31]: the thermal excitation of the crystal field levels. The relaxation rate appears to saturate and becomes temperature independent from about 2 K down to 25 mK with no sign of magnetic ordering in $ErMgGaO_4$. The value of relaxation rate below 2 K, $\lambda \sim 6\ \mu s^{-1}$, is considerably larger than the corresponding value found in $YbMgGaO_4$ ($0.3\ \mu s^{-1}$) [34], this difference is likely due to the larger moment from Er^{3+} compared to Yb^{3+}.

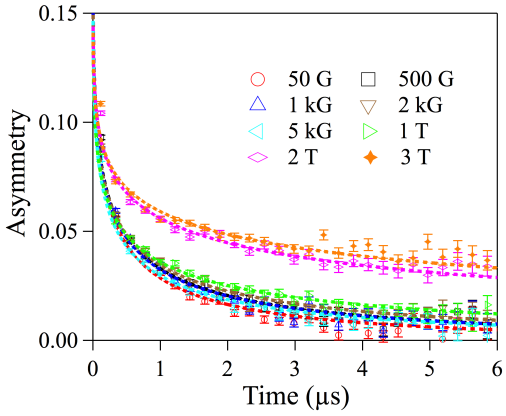

FIG. 6. μSR measurements on $ErMgGaO_4$ at 25 mK in selected longitudinal field up to 3 T.

We also performed longitudinal field (LF) μSR measurements to test for the presence of spin fluctuations. In a LF-μSR setup, the external field is applied in the direction of the initial muon spin polarization. In the case

of a quasi-static internal field distribution, a static relaxation signal will be nearly fully decoupled by an applied field that is a few times larger than the field corresponding to the ZF relaxation rate. However, if the relaxation of the ZF-μSR signal comes from fluctuating fields, the signal will not be decoupled by an applied field of this magnitude. In this case, the signal will only slowly decouple, and relaxation will continue to be apparent up to relatively large applied longitudinal fields [32]. If the fluctuation rate is independent of the applied field, then the relaxation rate will decrease with applied field according to the Redfield form [33], where a field corresponding roughly to the fluctuation rate will be needed to greatly decrease the relaxation. In Fig. 6, we present our LF scans at 25 mK, the relaxation rate at this temperature is barely decoupled even up to 1 T (much bigger than the local field $\lambda_0/\gamma_\mu \sim 66$ G, we would infer from our ZF spectra if the origin of the ZF relaxation were quasi-static internal fields). This means the spins associated with the Er^{3+} ions remain in a dynamically fluctuating state down to our lowest temperature 25 mK, consistent with a quantum spin liquid state. Similar spin dynamics were found in $YbMgGaO_4$ with estimated local fields $\sim$ 0.09 mT, where only small decoupling was observed with applied LF field up to 0.18 T [34].

In conclusion, we have grown single crystals and have performed a detailed study of magnetism and spin dynamics in $ErMgGaO_4$. Our ZF-μSR, specific heat and magnetic susceptibility measurements reveals no presence of static internal magnetic fields or magnetic transition. LF-μSR measurements detect the existence of persistent spin fluctuations down to our lowest temperature $\sim$ 25 mK. Our observations provide evidence of a quantum spin liquid state in the triangular antiferromagnet $ErMgGaO_4$. Point charge calculations suggest that the Er moments are predominately Ising-like, in contrast to the Heisenberg spins found in $YbMgGaO_4$; however inelastic neutron scattering measurements to experimentally determine the CEF parameters would be needed to confirm this.

We greatly appreciate the support of personnel at TRIUMF during the μSR measurements. Work at McMaster was supported by the Natural Sciences and Engineering Research of Council of Canada.

[1] L. Balents. *Nature* **464**, 199-208, 2010.
[2] N. Chetan, et al. Reviews of Modern Physics 80.3 (2008): 1083.
[3] J.E. Greedan, Journal of Alloys and Compouonds **408-412**, 444 (2006).
[4] J.S. Gardner, M.J.P. Gingras, and J.E. Greedan, Rev. Mod. Phys. **82**, 53 (2010).
[5] J.N. Reimers, J.E. Greedan, R.K. Kremer, E. Gmelin, and M.A. Subramanian, Phys. Rev. B **43**, 3387 (1991).
[6] Y. Li, G. Chen, W. Tong, L. Pi, J. Liu, Z. Yang, X. Wang, and Q. Zhang, *Phys. Rev. Lett.* **115**, 167203 (2015).
[7] J.A.M. Paddison, M. Daum, Z.L. Dun, G. Ehlers, Y. Liu, M.B. Stone, H.D. Zhou, M. Mourigal *Nat. Phys.*, **13** 177 122 (2017)
[8] Y. Li, D. Adroja, R. I. Bewley, D. Voneshen, A. A. Tsirlin, P. Gegenwart, and Q. Zhang *Phys. Rev. Lett.* **118**, 107202 (2017)
[9] Y. Li, H. Liao, Z. Zhang, S. Li, F. Jin, L. Ling, L. Zhang, Y. Zou, L. Pi, Z. Yang, J. Wang, Z. Wu, Q. Zhang *Sci. Rep.*, **5** 16419 (2015).
[10] Y. Shen, Y.-D. Li, H. Wo, Y. Li, S. Shen, B. Pan, Q. Wang, H.C. Walker, P. Steffens, M. Boehm, Y. Hao, D.L. Quintero-Castro, L.W. Harriger, M.D. Frontzek, L. Hao, S. Meng, Q. Chang, G. Chen, J. Zhao *Nature*, **540** 559-562 (2016)
[11] Z. Zhu, P.A. Maksimov, S.R. White, A.L. Chernyshev *Phys. Rev. Lett.*, *119* 157201 (2017)
[12] F. Alex Cevallos, Karoline Stolze, Robert J. Cava, *Solid State Communications*, **276**, 5-8, (2018).
[13] H.J. Silverstein, K. Fritsch, F. Flicker, A.M. Hallas, J.S. Gardner, Y. Qiu, G. Ehlers, A.T. Savici, Z. Yamani, K.A. Ross, B.D. Gaulin, M.J.P. Gingras, J.A.M. Paddison, K. Foyevtsova, R. Valenti, F. Hawthorne, C.R. Wiebe, and H.D. Zhou, Phys. Rev. B **89**, 054433 (2014).
[14] J.-J. Wen, S.M. Koohpayeh, K.A. Ross, B.A. Trump, T.M. McQueen, K. Kimura, S. Nakatsuji, Y. Qiu, D.M. Pajerowski, J.R.D. Copley, and C.L. Broholm, Phys. Rev. Lett. **118**, 107206 (2017).
[15] B. Gao, T. Chen, D.W. Tam, C.-L. Huang, K. Sasmal, D.T. Adroja, F. Ye, H. Cao, G. Sala, M.B. Stone, C. Baines, J.A.T. Barker, H. Hu, J.-H. Chung, X. Xu, S.-W. Cheong, M. Nallaiyan, S. Spanga, M.B. Maple, A.H. Nevidomskyy, E. Morosan, G. Chen, and P. Dai, arXiv: 1901.10092
[16] J. Gaudet, E.M. Smith, J. Dudemaine, J. Beare, C.R.C. Buhariwalla, N.P. Butch, M.B. Stone, A.I. Kolesnikov, G. Xu, D.R. Yahne, K.A. Ross, C.A. Marjerrison, J.D. Garrett, G.M. Luke, A.D. Bianchi, and B.D. Gaulin, arXiv: 1903.09207
[17] J. Snyder, J.S. Slusky, R.J. Cava, and P. Schiffer, Nature **413**, 48 (2001).
[18] J.D.M. Champion, M.J. Harris, P.C.W. Holdsworth, A.S. Wills, G. Balakrishnan, S.T. Bramwell, E. Cizmar, T. Fennell, J.S. Gardner, J. Lago, D.F. McMorrow, M. Orendac, A. Orendacova, D. McK. Paul, R.I. Smith, M.T.F. Telling, and A. Wildes, Phys. Rev. B **68**, 020401(R) (2003).
[19] K.A. Ross, Y. Qiu, J.R.D. Copley, H.A. Dabkowska, and B.D. Gaulin, Phys. Rev. Lett. **112**, 057201 (2014).
[20] O. Benton, Phys. Rev. B **94**, 104430 (2016).
[21] S. Petit, E. Lhotel, B. Canals, M. Ciomaga Hatnean, J. Ollivier, H. Mutka, E. Ressouche, A. R. Wildes, M. R. Lees, and G. Balakrishnan, Nature Physics **12**, 746 (2016).
[22] J. R. Stewart, G. Ehlers, A. S. Wills, S. T. Bramwell, and J. S. Gardner, *J. Phys.: Condens. Matter* **16**, L321 (2004).
[23] A. Keren, Y. J. Uemura, G. Luke, P. Mendels, M. Mekata, and T. Asano, *Phys. Rev. Lett.* **84**, 3450 (2000).
[24] J. S. Gardner, S. R. Dunsiger, B. D. Gaulin, M. J. P. Gingras, J. E. Greedan, R. F. Kiefl, M. D. Lumsden, W. A. MacFarlane, N. P. Raju, J. E. Sonier, I. Swainson, and Z. Tun, *Phys. Rev. Lett.* **82**, 1012 (1999).

[25] Y. Cai, C. Lygouras, G. Thomas, M. N. Wilson, H. A. Dabkowska, G. M. Luke. *APS Meeting Abstracts* (2018)
[26] Y. Cai, M.N. Wilson, J. Beare, C. Lygouras, G. Thomas, D.R. Yahne, K. Ross, K.M. Taddei, G. Sala, H.A. Dabkowska, A. A. Aczel, G. M. Luke, arXiv:1905.03687
[27] Cevallos, F. A., Stolze, K., Kong, T., Cava, R. J. *Materials Research Bulletin*. **105** 154-158 (2018).
[28] M. T. Hutchings *Solid State Physics* vol16, ed F. Seitz and D Turnbull (New York: Academic) p 227
[29] A. Suter, B. M. Wojek, "Musrfit: A Free Platform-Independent Framework for μSR Data Analysis", *Physics Procedia* **30**, 69 (2012).
[30] A. Yaouanc and P. Dalmas de Reotier, *Muon Spin Rotation, Relaxation, and Resonance: Applications to Condensed Matter* (Oxford University Press, 2011).
[31] R. Orbach, *Proc. Phys. Soc.* London Sect. A 264, 458 (1961).
[32] Y. J. Uemura, T. Yamazaki, R. S. Hayano, R. Nakai, and C. Y. Huang, *Phys. Rev. Lett.* **45**, 583 (1980).
[33] C.P. Slichter, *Principles of Magnetic Resonance*, Springer Verlag (1978)
[34] Yuesheng Li, Devashibhai Adroja, Pabitra K. Biswas, Peter J. Baker, Qian Zhang, Juanjuan Liu, Alexander A. Tsirlin, Philipp Gegenwart, and Qingming Zhang, *Phys. Rev. Lett.* **117**, 097201 (2016).

6

Conclusions and Future Directions

This thesis has examined three different frustrated magnet families including 3D tetrahedra network in pryochlores, 3D twisted triangular network in gallium garnet and quasi 2D triangular network in $ErMgGaO_4$.

In our study of $NaCaNi_2F_7$, we have revealed the weak effect of the disorder on its magnetic ground state, where the disorder comes from chemical disorder from the stochastic mixture of elements on the A site. This results in the Ni^{2+} spins undergo spin freezing into a disordered ground state below 4K, with remaining persistent spin dynamics.

In our study of $Er_3Ga_5O_{12}$, we present a comprehensive study of the single ion and collective magnetic properties. We found a crystal field ground state doublet for Er^{3+} with Ising anisotropy along local [100] axes. Magnetic susceptibility and heat capacity measurements provide evidence for long-range magnetic ordering with $T_N = 0.8$ K, and no evidence for residual entropy is found when cooling through the ordering transition. Neutron powder diffraction reveals that the ground state spin configuration corresponds to the six-sublattice, Ising antiferromagnetic state (Γ_3) common to many of the rare earth garnets. Our results indicate that $Er_3Ga_5O_{12}$ is an excellent model system for studying the complex metamagnetism expected for a multi-axis antiferromagnet.

In our study of $ErMgGaO_4$, we have successfully synthesized crystal of $ErMgGaO_4$, a closely related material to $YbMgGaO_4$ which was found to be a quantum spin liquid candidate. Our susceptibility, specific heat, and ZF-μSR measurements indicate no presence of a magnetic transition in $ErMgGaO_4$. LF-μSR measurements show evidence of persistent spin fluctuations down to our lowest temperature 25 mK. Our observation provide evidences of a quantum spin liquid state in this triangular antiferromagnet $ErMgGaO_4$.

During these studies, one exotic property of these frustrated compounds that has become apparent lies in their dynamics. The origin of the observed persistent spin dynamics in frustrated magnets, which features with a temperature independent spin lattice relaxation rate irrespective of the presence of magnetic order or not, remains elusive. The lack of spontaneous muon spin precession in $Er_2Ti_2O_7$ [45, 51] and $Yb_2Sn_2O_7$ [52] in their ordered states is also not understood. A physical understanding for such phenomenon is still missing. Future study on the spin lattice relaxation rate on $Er_3Ga_5O_{12}$ would be essential in understanding such extraordinary spin dynamics found in the magnetic ordered state.

Furthermore, It would be important to synthesis larger single crystal of $ErMgGaO_4$, which is essential for experimental techniques like neutron scattering. Finally, It would be interesting to do a more thorough characterization of the liquid behaviour of $ErMgGaO_4$. In particular, It was found that the disorder effect in $YbMgGaO_4$ seems to be stabilizing its liquid state, it would be useful to have neutron scattering measurements that could probe the excitations to better understand the ground state, the spin anisotropy and such disorder effect as well.

7

Appendix

The theory of point charge calculation was well established in Ref. [7]. However, there is no open access to an detail example of such calculation. This code would save much time for other colleagues who are interested in CEF analysis.

Listing 7.1: Matlab code for CEF parameters under point charge approximation, example of $Er_3Ga_5O_{12}$

```
function BCoeff=Point_charge_cal()
clear all;
%point charge calculation

J=15/2; % For Er
a= 12.352e-10;  %  a is lattice parameter
q=-1.602176e-19; % charge e
oneover4piepsilon0=9e9; % (1/(4*pi*epsilon) unit is N*m^2*C^-2)
epsilon0=8.854187817e-12; % with unit C^2 * N-1 * m^-2
%from N*m to eV is 1N*m= 6.24150913e18eV
unittrans=6.24150913e18;
% bohr magneton
bohr_magneton=5.7883818012e-5;   % with unit eV/T
g_J=6/5;
bohr_radius=5.29177e-11; %   this is the unit for the meanr^2 and meanr^4!!!!!!
t=pi;
Ry = [cos(t) 0 sin(t); 0 1 0; -sin(t) 0 cos(t)];

%one way to generate the Zvector, use three Er atom in the triangluar lattice.
Atom_Er_position = a*[0.25, 0.125, 0;0.125,0,0.25;0,0.25,0.125]; % first one is the Er
    used, the other two is to generate the symmetry Zunit

%
Atom_O_position = a*[0.3492,-0.02636,-0.05657; 0.22364,0.0992,-0.19343;
```

```
    0.44343,0.15080,0.02636; 0.30657,0.27636,-0.0992;
    0.15080,-0.02636,0.05657; 0.27636,0.09920,0.19343;
    0.05657,0.15080,-0.02636; 0.19343,0.27636,0.09920;  % 8 Nearest and then 8 NN
    0.47340,-0.05670,0.15110; 0.40110,0.30670,0.22340;
    0.09890,0.19330,0.27660; -0.02660,0.05670,0.15110;
    0.52660,0.05670,-0.15110; 0.40110,0.19330,-0.27660;
    0.09890,0.30670,-0.22340; 0.02660,-0.05670,-0.15110; % 4 Nearest Er ions with
        positive charge
    0.125,0.0, 0.25; 0, 0.25, 0.125; 0.375, 0.0 -0.25; 0.5,0.25,-0.125];



Xunit =[0,1,1]/sqrt(2);
Yunit=[0,-1,1]/sqrt(2);
Zunit=[1,0,0]/sqrt(1);   %Ising direction

%could considering 16 O around Er atom (with extra 8 Next nearest neighbour)

n=8; % only consider the Nearest 8 O ions


%calculate the theta and phi

for i =1:n
    Atom_ErObond(i,:) = Atom_O_position(i,:)-Atom_Er_position(1,:);
    Atom_ErObond_ProjPlane(i,:) = Atom_ErObond(i,:)-dot(Atom_ErObond(i,:),Zunit)*Zunit;
    Atom_ErO_R(i) = sqrt(sum(Atom_ErObond(i,:).^2));
    theta(i) = acos(dot(Atom_ErObond(i,:)/norm(Atom_ErObond(i,:)),Zunit));
        if(Atom_ErObond_ProjPlane(i,2) < 0)
            phi(i) = 2*pi-acos(dot(Atom_ErObond_ProjPlane(i,:)/norm(
                Atom_ErObond_ProjPlane(i,:)),Xunit));
        else
            phi(i) = acos(dot(Atom_ErObond_ProjPlane(i,:)/norm(Atom_ErObond_ProjPlane(i
                ,:)),Xunit));
        end
end


% calculate CEF parameters
for j=1 %B20
    for i = 1:n
        if i<=16
            temp(i)= q*(4*pi/(2*2+1)) *2*q/(Atom_ErO_R(i)^(2*2-1))  *ylm(2,-2*(j-1),theta
                (i),phi(i));
        else
            temp(i)= -q*(4*pi/(2*2+1)) * 3*q/(Atom_ErO_R(i)^(2*2-1))  *ylm(2,-2*(j-1),
                theta(i),phi(i));
```

```
66          end
67      end
68      A_CF_para(j)=sum(temp);
69  end
70
71  for j=2 %B22
72      for i = 1:n
73          if i <=16
74              temp(i)= q*(4*pi/(2*2+1)) *2*q/(Atom_ErO_R(i)^(3)) *1/sqrt(2)*(ylm(2,-2*(j-1)
                    ,theta(i),phi(i))+ylm(2,2*(j-1),theta(i),phi(i)));
75          else
76              temp(i)= -q*(4*pi/(2*2+1)) *3*q/(Atom_ErO_R(i)^(3)) *1/sqrt(2)*(ylm(2,-2*(j
                    -1),theta(i),phi(i))+ylm(2,2*(j-1),theta(i),phi(i)));
77          end
78      end
79      A_CF_para(j)=sum(temp);
80  end
81
82  for j=3  %B40
83      for i = 1:n
84          if i<=16
85              temp(i)=q*(4*pi/(2*4+1)) *2*q/((Atom_ErO_R(i))^(5)) * ylm(4,-2*(j-3),theta(i)
                    ,phi(i));
86          else
87              temp(i)=-q*(4*pi/(2*4+1)) *3*q/((Atom_ErO_R(i))^(5)) * ylm(4,-2*(j-3),theta(i
                    ),phi(i));
88          end
89      end
90      A_CF_para(j)=sum(temp);
91  end
92
93  for j=4:5 %B42 B44
94      for i = 1:n
95          if i<=16
96              temp(i)=q*(4*pi/(2*4+1)) *2*q/((Atom_ErO_R(i))^(5)) *1/sqrt(2) * (ylm(4,-2*(j
                    -3),theta(i),phi(i)) + (-1)^(2*(j-3)) * ylm(4,2*(j-3),theta(i),phi(i)));
97          else
98              temp(i)=-q*(4*pi/(2*4+1)) *3*q/((Atom_ErO_R(i))^(5)) *1/sqrt(2) * (ylm(4,-2*(
                    j-3),theta(i),phi(i)) + (-1)^(2*(j-3)) * ylm(4,2*(j-3),theta(i),phi(i)));
99          end
100     end
101     A_CF_para(j)=sum(temp);
102 end
103
104
105 for j=6 %B60
106     for i =1:n
```

```
107         if i<=16
108             temp2(i)=q*(4*pi/(2*6+1)) *2*q/((Atom_ErO_R(i))^(7))  * ylm(6,-2*(j-6),theta(
                    i),phi(i));
109         else
110             temp2(i)=-q*(4*pi/(2*6+1)) *3*q/((Atom_ErO_R(i))^(7))  * ylm(6,-2*(j-6),theta
                    (i),phi(i));
111         end
112     end
113     A_CF_para(j)=sum(temp2);
114 end
115
116 for j=7:9 %B62 64 66
117     for i =1:n
118         if i<=16
119             temp2(i)=q*(4*pi/(2*6+1)) *2*q/((Atom_ErO_R(i))^(7)) *1/sqrt(2) * (ylm(6,-2*(
                    j-6),theta(i),phi(i))+ (-1)^(2*(j-6))*ylm(6,2*(j-6),theta(i),phi(i)));
120         else
121             temp2(i)=-q*(4*pi/(2*6+1)) *3*q/((Atom_ErO_R(i))^(7)) *1/sqrt(2) * (ylm
                    (6,-2*(j-6),theta(i),phi(i))+ (-1)^(2*(j-6))*ylm(6,2*(j-6),theta(i),phi(i
                    )));
122         end
123     end
124     A_CF_para(j)=sum(temp2);
125 end
126
127 % other coefficient in CEF parameter B_n^i
128 alphaEr=4/(9*25*7);
129 betaEr = 2/(9*5*7*11*13);
130 gammaEr = 8/(27*7*11^2*13^2);
131 sigma=[0.460,0.0190,-0.0283];
132 meanr = [0.750,1.49,6.52];
133 %meanr=[0.666,1.126,3.978]; % from https://onlinelibrary.wiley.com/doi/pdf/10.1002/qua
        .560080816
134
135 for i=1:2;
136     %B(i)=alphaEr*(1-sigma(1))*A_CF_para(i)*meanr(1);
137     B(i)=alphaEr*A_CF_para(i)*meanr(1)*bohr_radius^2;
138
139 end
140 for i=3:5
141     % B(i)=betaEr*(1-sigma(2))*A_CF_para(i)*meanr(2);
142     B(i)=betaEr*A_CF_para(i)*meanr(2)*bohr_radius^4;
143
144 end
145 for i=6:9
146     % B(i)=gammaEr*(1-sigma(3))*A_CF_para(i)*meanr(3);
147     B(i)=gammaEr*A_CF_para(i)*meanr(3)*bohr_radius^6;
```

```
148
149 end
150
151 Coeff_Zna=[0.25*sqrt(5/pi),0.25*sqrt(15/pi),3/(sqrt(pi)*16),sqrt(5/pi)*3/8,sqrt(35/pi)
        *3/16,...
152     sqrt(13/pi)/32,sqrt(2730/pi)/64,sqrt(13/(7*pi))*21/32,sqrt(26/(231*pi))*231/64];
153
154
155
156
157 BCoeff=1000*B.*Coeff_Zna*oneover4piepsilon0*unittrans; % 1000 is for unit meV instead of
        eV
158
159 [O20,O22,O40,O42,O43,O44,O60,O62,O63,O64,O66,Jx,Jy,Jz,Jplus,Jminus,Jsquare,Unit] =
        OperatorTotalmomentum(J);
160 Hcef_pointcharge_cal=BCoeff(1)*O20+BCoeff(2)*O22+BCoeff(3)*O40+BCoeff(4)*O42+BCoeff(5)*
        O44+BCoeff(6)*O60+BCoeff(7)*O62+BCoeff(8)*O64+BCoeff(9)*O66; % - 1000*g_J*
        boho_magneton*(0.1e-3)*Jz; % could add a Zeeman term if needed
161 %Hcef_pointcharge_cal = round(Hcef_pointcharge_cal,6); % may need to round
162
163 % solve the Hamiltonian for eigenvalue and eigenvector
164 [V_pointcharge_cal,E_pointcharge_cal] = eig(Hcef_pointcharge_cal,'Vector');
165 [Energy_pointcharge_cal,index]=sort(E_pointcharge_cal);
166 V_pointcharge_cal=V_pointcharge_cal(index,:);
167 Energy_pointcharge_cal = (Energy_pointcharge_cal + abs(min(E_pointcharge_cal(:,1))))
168
169 % calculate g-tensors
170 gz=abs(g_J*2*V_pointcharge_cal(:,1)'*Jz*V_pointcharge_cal(:,1));
171 gx=abs(g_J*2*V_pointcharge_cal(:,1)'*Jx*V_pointcharge_cal(:,2));
172 gy=abs(g_J*2*V_pointcharge_cal(:,1)'*Jy*V_pointcharge_cal(:,2));
173 if gz<0
174    g_xy=V_pointcharge_cal(:,2)'*Jplus*V_pointcharge_cal(:,1);
175 else
176     g_xy=V_pointcharge_cal(:,1)'*Jplus*V_pointcharge_cal(:,2);
177 end
178
179 G_tensor_abc=[gx,gy,gz]
180
181 %ground state doublet wave function
182 [V_pointcharge_cal(:,1),V_pointcharge_cal(:,2)]
183
184 end
```

Listing 7.2: Steven Operators based on theory Ref. [7]

```
1 function [O20,O22,O40,O42,O43,O44,O60,O62,O63,O64,O66,Jx,Jy,Jz,Jplus,Jminus,Jsquare,Unit]
      = OperatorTotalmomentum(J)
2
```

```
Jplus  = zeros((2.*J+1),(2.*J+1));
Jminus = zeros((2.*J+1),(2.*J+1));
Jz     = zeros((2.*J+1),(2.*J+1));
Unit = eye(2.*J+1);

Jz = zeros((2.*J)+1,(2.*J)+1);
for i = 1:((2.*J)+1)
    Jz(i,i) = ((-J) + (i-1));
end

for i = 1:(2.*J)
    Jplus(i+1,i) = sqrt( ((J) - (-(J  )+(i-1))).*((J)+((-J)+(i-1))+1) );
    Jminus(i,i+1)  = sqrt( ((J) + (-(J-1)+(i-1))).*((J)-((-(J-1))+(i-1))+1) );
end

imag = sqrt(-1);
Jx = (0.5).*(Jplus + Jminus);
Jy = (0.5)*imag.*(Jminus - Jplus);

Jsquare = (Jx*ctranspose(Jx)) + (Jy*ctranspose(Jy)) + (Jz*ctranspose(Jz));
Jplussquare = Jplus*Jplus;
Jminussquare = Jminus*Jminus;

% Steven operators definition, detail could be find in the ref.(hunching)
O20 = 3.*(Jz^2) - Jsquare;
O22 = 0.5.*(Jplus^2+Jminus^2);
O40 = 35.*(Jz^4) - 30.*(Jsquare*(Jz^2)) + 25.*(Jz^2) -6.*(Jsquare) + 3.*(Jsquare^2);
O42 = 0.25.*((7*(Jz^2)-Jsquare-5*Unit)*(Jplus^2+Jminus^2)+(Jplus^2+Jminus^2)*(7*(Jz^2) -
    Jsquare - 5*Unit));
O44 = 0.5.*(Jplus^4+Jminus^4);
O60 = 231.*(Jz^6) - 315.*(Jsquare*(Jz^4)) + 735.*(Jz^4) + 105.*((Jsquare^2)*(Jz^2)) -
    525.*(Jsquare*(Jz^2)) + 294.*(Jz^2) - 5.*(Jsquare^3) + 40.*(Jsquare^2) - 60.*(Jsquare
    );
O43 = 0.25.*(Jz*(Jplus^3+Jminus^3) + (Jplus^3+Jminus^3)*Jz);
O62 = 0.25.*((33.*(Jz^4) - (18.*Jsquare + 123*Unit)*Jz^2 + Jsquare^2 + 10.*Jsquare + 102*
    Unit) * (Jplus^2 + Jminus^2) + (Jplus^2 + Jminus^2) * (33.*(Jz^4) - (18.*Jsquare +
    123*Unit)*Jz^2 + Jsquare^2 + 10.*Jsquare + 102.*Unit));
O63 = 0.25.*( ((11.*Jz^3 -3.*(Jsquare*Jz) - 59.*Jz)*(Jplus^3+Jminus^3)) +  ((Jplus^3+
    Jminus^3))*(11.*Jz^3 -3.*(Jsquare*Jz) - 59.*Jz));
O64 = 0.25.*((11.*Jz^2 - Jsquare - 38*Unit)*(Jplus^4+Jminus^4) + (Jplus^4+Jminus^4)*(11.*
    Jz^2 - Jsquare - 38*Unit));
O66 = 0.5.*(Jplus^6 + Jminus^6);

end
```

Bibliography

[1] Y. Cai, M.N. Wilson, A.M. Hallas, L. Liu, B. A. Frandsen, S. R. Dunsiger, J. W. Krizan, R. J. Cava, Y. J. Uemura, O. Rubel, and G. M. Luke. J. Phys.: Condens. Matter **30** 385802.

[2] Kronmüller, Helmut. (2007). Handbook of Magnetism and Advanced Magnetic Materials, 5 Volume Set. John Wiley & Sons.

[3] G. Toulouse *Commun. Phys.*, 1977, **2**, 115.

[4] P. W. Anderson. *phys. Rev.*, 1956, **102**, 1008.

[5] John. E. Greedan. *J. Mater. Chem.*, 2001,**11**, 37-53.

[6] HA Kramers. Théorie générale de la rotation paramagnétique dans les cristaux. Proc. Acad. Amst, 33:959?972, 1930.

[7] KWH Stevens. Matrix elements and operator equivalents connected with the magnetic properties of rare earth ions. Proceedings of the Physical Society. Section A, 65(3):209, 1952.

[8] J. S. Gardner, S. R. Dunsiger, B. D. Gaulin, M. J. P. Gingras, J. E. Greedan, R. F. Kiefl, M. D. Lumsden, W. A. MacFarlane, N. P. Raju, J. E. Sonier, I. Swainson, and Z. Tun, *Phys. Rev. Lett.* **82**, 1012 (1999).

[9] M. J. Harris, S. T. Bramwell, D. F. McMorrow, T. Zeiske, and K. W. Godfrey, *Phys. Rev. Lett.* **79**, 2554 (1997).

[10] Ramirez A. P., Hayashi A., Cava R. J., Siddharthan R., and Shastry B. S., *Nature* 399 (6734), 333 (1999).

[11] J. Villain, Z. *Phys. B*, 1979, **33**, 31.

[12] Leon Balents. *Nature* **464**, 199-208, 2010.

[13] Savary L and Balents L 2017 Reports on Progress in Physics 80 016502.

[14] Imai T and Lee Y S 2016 Physics Today 69 30.

[15] P. W. Anderson, *Mater. Res. Bull.*, 1973, **8**, 153

[16] Bednorz J G and Müller K A 1986 Z. *Phys. B* **64** 189

[17] Li Y, Liao H, Zhang Z, Li S, Jin F, Ling L, Zhang L, Zou Y, Pi L, Yang Z, Wang J, Wu Z and Zhang Q 2015 Sci. Rep. 5 16419

[18] Li Y, Chen G, Tong W, Pi L, Liu J, Yang Z, Wang X and Zhang Q 2015 Phys. Rev. Lett. 115 167203

[19] J.A.M. Paddison, M. Daum, Z.L. Dun, G. Ehlers, Y. Liu, M.B. Stone, H.D. Zhou, M. Mourigal *Nat. Phys.*, **13** 177 122 (2017)

[20]] Li Y, Adroja D, Biswas P K, Baker P J, Zhang Q, Liu J, Tsirlin A A, Gegenwart P and Zhang Q 2016 Phys. Rev. Lett. 117 097201

[21] Y. Shen, Y.-D. Li, H. Wo, Y. Li, S. Shen, B. Pan, Q. Wang, H.C. Walker, P. Steffens, M. Boehm, Y. Hao, D.L. Quintero-Castro, L.W. Harriger, M.D. Frontzek, L. Hao, S. Meng, Q. Chang, G. Chen, J. Zhao *Nature*, **540** 559-562 (2016)

[22] Z. Zhu, P.A. Maksimov, S.R. White, A.L. Chernyshev *Phys. Rev. Lett.*, *119* 157201 (2017)

[23] G. ZHang, M. M. Chou and C. Lin, *Crystals* 2017, **7**, 167

[24] H. A. Dabkowska, A. B. Dabkowski. *Crystal growth of oxides by optical floating zone technique* Springer-Verlag Berlin Heidelberg, 2010, p. 367

[25] B. Josephson. *Physics Letters*, 2 (7): 251 (1962).

[26] M. Tinkham. *Introduction to Superconductivity.* Dover Publications, New York, second edition (1996).

[27] A. Yaouanc and P. Dalmas de Reotier, *Muon Spin Rotation, Relaxation, and Resonance: Applications to Condensed Matter* (Oxford University Press, 2011).

[28] S.L. Lee, S.H. Kilcoyne, and R. Cywinski, editors. *μSR relaxationfunctions in magnetic materials* (Institute of Physics Publishing, 1999)

[29] A. Schenck. *Muon spin rotation spectroscopy: principles and applications in solid state physics* Bristol; Boston: A. Hilger, 1985.

[30] Hayano R S, Uemura Y J, Imazato J, Nishida N, Yamazaki T and Kubo R 1979 *Phys. Rev. B 20* 850

[31] Uemura Y J, Yamazaki T, Harshman D R, Senba M and Ansaldo E J 1985 *Phys. Rev. B 31* 546

[32] J. H. Brewer, S. R. Kreitzman, D. R. Noakes, E. J. Ansaldo, D. R. Harshman, and R. Keitel, *Phys. Rev. B* **33**, 7813(R) (1986).

[33] D. R. Noakes, E. J. Ansaldo, and G. M. Luke *J. Appl. Phys* **73**, 5666 (1993).

[34] J. H. Brewer, D. R. Harshman, R. Keitel, S. R. Kreitzman, G. M. Luke, D. R. Noakes, and R. E. Turner. *Hyperfine Interact.*, 32:677 (1986).

[35] K. Nishiyama, S. W. Nishiyama, and W. Higemoto. *Physica* **B**, 326:41 (2003)

[36] J. Rodriguez, A. A. Aczel, J. P. Carlo, S. R. Dunsiger, G. J. MacDougall, P. L. Russo, A. T. Savici, Y. J. Uemura, C. R. Wiebe, and G. M. Luke *Phys. Rev. Lett.* **105**, 107203 (2010).

[37] G. Shirane, S. M. Shapiro, and J. M. Tanquada. Neutron Scattering with a Triple-Axis Spectrometer. Cambridge University Press, Cambridge (2004).

[38] W. L. Bragg. Cambridge Philosophical Society, 17: 43 (1913).

[39] G. Squires, Introduction to the Theory of Thermal Neutron Scattering (Cambridge University Press, Cambridge, UK, 1978).

[40] Krizan J W and Cava R J 2015 *Phys. Rev. B* **92** 014406

[41] Y. J. Uemura, A. Keren, K. Kojima, L. P. Le, G. M. Luke, W. D. Wu, Y. Ajiro, T. Asano, Y. Kuriyama, M. Mekata, H. Kikuchi, and K. Kakurai, *Phys. Rev. Lett.* **73**, 3306 (1994).

[42] R. M. D'Ortenzio, H. A. Dabkowska, S. R. Dunsiger, B. D. Gaulin, M. J. P. Gingras, T. Goko, J. B. Kycia, L. Liu, T. Medina, T. J. Munsie, D. Pomaranski, K. A. Ross, Y. J. Uemura, T. J. Williams, and G. M. Luke, *Phys. Rev. B* **88**, 134428 (2013).

[43] A. M. Hallas, J. Gaudet, M. N. Wilson, T. J. Munsie, A. A. Aczel, M. B. Stone, R. S. Freitas, A. M. Arevalo-Lopez, J. P. Attfield, M. Tachibana, C. R. Wiebe, G. M. Luke, and B. D. Gaulin, *Phys. Rev. B* **93**, 104405 (2016).

[44] H. Capel, Physica 31, 1152 (1965).

[45] J. Lago, T. Lancaster, S.J. Blundell, S.T. Bramwell, F.L. Pratt, M. Shirai, and C. Baines, J. Phys.: Condens. Matter **17**, 979 (2005).

[46] P. Dalmas de Reotier, A. Yaouanc, L. Keller, A. Cervellino, B. Roessli, C. Baines, A. Forget, C. Vaju, P.C.M. Gubbens, A. Amato, and P.J.C. King, Phys. Rev. Lett. **96**, 127202 (2006).

[47] S.R. Dunsiger, R.F. Kiefl, J.A. Chakhalian, J.E. Greedan, W.A. MacFarlane, R.I. Miller, G.D. Morris, A.N. Price, N.P. Raju, and J.E. Sonier, Phys. Rev. B **73**, 172418 (2006).

[48] G.M. Kalvius, A. Krimmel, O. Hartmann, F.J. Litterst, R. Wappling, F.E. Wagner, V. Tsurkan, and A. Loidl, Eur. Phys. J. B **77**, 87 (2010).

[49] P.A. McClarty, J.N. Cosman, A.G. Del Maestro, and M.J.P. Gingras, J. Phys.: Condens. Matter **23**, 164216 (2011).

[50] Yuesheng Li, Devashibhai Adroja, Robert I. Bewley, David Voneshen, Alexander A. Tsirlin, Philipp Gegenwart, and Qingming Zhang *Phys. Rev. Lett.* **118**, 107202 (2017)

[51] P. Dalmas de Reotierr, et al, Phys. Rev. B 86, 104424 (2012).

[52] A. Yaouanc, et al, Phys. Rev. Lett. 110, 127207 (2013).